

Improving Utilization of Ir-Based Catalyst Layers in Proton Exchange Membrane Water Electrolyzers

by

Eric Beaulieu

A thesis submitted in partial fulfillment of the requirements for the degree of

Master of Science

Department of Mechanical Engineering

University of Alberta

© Eric Beaulieu, 2024

Abstract

In order to store large quantities of intermittent renewable energy, proton exchange membrane water electrolyzers (PEMWE) can be used to produce hydrogen which can then be used in a fuel cells to retrieve the energy. One limitation of PEMWE is that the catalysts used, commonly platinum and iridium, are scarce and expensive. In this work, two methods are studied to reduce the loading of iridium. The first method is to reduce catalyst loading of a state-of-the-art IrO_x catalyst. Modelling predicted that, for a catalyst with poor electronic and protonic conductivity and high catalyst activity, reducing the loading should result in increased performance. The effects of the reduced loading will be studied to determine catalyst utilization and, if it is poor, study why that is the case. The second method is to combine nickel with iridium to increase the efficacy of the catalyst which, for similar loadings, should provide increased performance.

To test both methods catalyst coated membranes (CCMs) were made using inkjet printing. Ir_8NiO_x was synthesized in-house using an alkaline aqueous reaction while commercial IrO_x , by Tanaka Kikinzoku Kogyo (TKK), was used for comparison and the loading study. To print the anode, Ir_8NiO_x inks were made by combining propylene glycol (PG), water, and Nafion while IrO_x inks contained PG, isopropanol (IPA) and Nafion. To print the cathode, platinum supported on carbon inks were made similarly to the IrO_x . The density, viscosity and particle size of each ink were measured to ensure that the fluid properties were compatible with the inkjet printer. These properties are im-

portant because they affect the ability of stable droplets to form as well as if clogging of print nozzles will occur. Four CCMs of Ir_8NiO_x at about 1 mg/cm^2 and 4 CCM batches of IrO_x at about 0.25, 0.5, 0.75 and 1 mg/cm^2 were successfully printed; each IrO_x batch includes one of each loading. Testing in a membrane electrode assembly (MEA) was conducted on three of the four Ir_8NiO_x and 12 of the 16 IrO_x CCMs. The remaining CCMs were used only for characterization of the catalyst layer through scanning electron microscopy and energy dispersive X-ray spectroscopy.

As the loading of the IrO_x catalyst layers decreased, the i-V curve performance was similar for the first two of the three tested batches. However, the third tested batch showed the 0.5 and 0.75 mg/cm^2 cells were similar but the high (1 mg/cm^2) and low (0.25 mg/cm^2) loadings had better and worse performance, respectively. These results partially validate the previously mentioned model. The benefits of reduced loading were not as drastic as predicted since the increase in kinetic losses was made up for by decreased ohmic losses. Since the effect of decreased loading was not as drastic as the model suggested, electrical conductivity testing was done under compression from 0-95 psig in an attempt to mimic the in-cell compression. It was found that the higher the compression, the higher the electrical conductivity but it did not match measurements of the electrical conductivity of IrO_x TTK in literature. This could simply be due to the different method of measurement so, further investigation into the electrical conductivity of the IrO_x catalyst is required to determine the cause of this discrepancy.

Ir_8NiO_x cells were found to have worse performance on an i-V curve as well as low electrochemical active surface area (ECSA) when compared to the IrO_x cells. The lower performance was primarily due to the instability of the Ir_8NiO_x catalyst layer as through SEM imaging it was found that a significant portion of the catalyst left the layer likely due to delamination caused by

trapped oxygen bubbles. Additionally, low ECSA could be due to the Ir_8NiO_x catalyst having a lower surface area, the catalyst layer having a higher packing density, or the catalyst not having as rough of a surface when compared to IrO_x . Although overall performance was low, when normalized by the ECSA it was found that the Ir_8NiO_x performed better on a site to site basis. In addition, the kinetic activity was found to be similar to the IrO_x however the ohmic and mass transport losses were larger resulting in the performance loss described above.

To my family

Acknowledgements

Thank you to my supervisor Professor Marc Secanell and co-supervisor Professor Steven Bergens for providing me the opportunity to gain valuable knowledge in the field of water electrolysis and lab experience. I would also like to thank them for the support and guidance that went in to the experimental work and writing of this thesis.

I would also like to acknowledge my fellow lab members Manas Mandal, Jasper Eitzen, Luis Padilla, Jiafei Liu, Fei Wei, Michael Moore and the rest of the Energy Systems Design Laboratory for supporting my work and always being willing to lend a helping hand. Thank you Luis and Manas for training me when I first started. Thank you Michael for fixing the code for the electrolyzer test stand as this work would not have continued smoothly without your help.

I acknowledge the funding from Future Energy Systems (FES) through the Canada First Research Excellence Fund (<https://futureenergysystems.ca>; Grant No. T06-P04) as well as the Natural Sciences and Engineering Research Council of Canada through the Alexander Graham Bell Canada Graduate Scholarship.

Finally, I would like to thank my family for their love and support throughout the degree. When experiments weren't going my way you were always there to keep me going.

Contents

1	Introduction	1
1.1	Motivation	1
1.2	Function and Characterization of PEMWE	3
1.2.1	Chemistry	3
1.2.2	The Membrane Electrode Assembly	5
1.2.3	Catalyst Layer Fabrication Method	7
1.2.4	Performance and Characterization	8
1.3	Literature Review	16
1.3.1	Variations in Loading	16
1.3.2	Iridium Bi-Metallic Catalysts	19
1.4	Thesis Objectives	23
2	Methodology	24
2.1	Catalyst Synthesis	24
2.1.1	Catalyst Preparation	24
2.1.2	Ex Situ Characterization	26
2.2	Electrode Fabrication	27
2.2.1	Catalyst Ink Development	27
2.2.2	Ink Characterization	30
2.2.3	Inkjet Printing	37
2.3	Ex Situ Characterization	39
2.3.1	Imaging	39
2.3.2	Through-plane Conductivity	41
2.3.3	Profilometry	44
2.4	Electrochemical Testing	44
2.4.1	Cell Assembly	44
2.4.2	Experimental Setup	46
2.4.3	Conditioning	48
2.4.4	Cyclic Voltammetry	50
2.4.5	Polarization Curves	51
2.4.6	Kinetic parameters	52
2.4.7	EIS	52
3	Study of Reducing IrO_x Anode Catalyst Layer Loading for Improved Cell Performance	55
3.1	Ink Characterization and Printing	55
3.2	Initial Ex Situ Characterization	58
3.2.1	Optical Microscopy	58
3.2.2	Catalyst Layer Thickness and Porosity	60
3.2.3	Uniformity and Adhesion	64
3.3	Electrochemical Characterization	66
3.3.1	Cyclic Voltammetry	66
3.3.2	Polarization Curves	71

3.3.3	Linear Scan Voltammetry	76
3.3.4	Electrochemical Impedance Spectroscopy	79
3.3.5	In-Situ Compression Effects	85
3.4	Ex-Situ Compression Effects	87
4	Ir-Ni Catalyst Upscaling and Assessment in a PEMWE	90
4.1	Catalyst Characterization	90
4.2	Ink Characterization	97
4.3	Initial Ex Situ Characterization	98
4.4	Electrochemical Characterization	104
4.4.1	Conditioning	104
4.4.2	Cyclic Voltammetry	105
4.4.3	Polarization Curves	109
4.4.4	Kinetic Parameters	114
4.4.5	Electrochemical Impedance Spectroscopy (EIS)	116
4.5	Final Ex Situ Characterization	124
4.6	Repeatability	128
5	Conclusions and Future Work	132
5.1	Conclusions	132
5.2	Future Work	136
	References	139
	Appendix A Additional Methodology	153
A.1	Triply Distilled Water	153
A.2	Viscometer Calibration	154
A.3	Setting Images	155
A.3.1	Inkjet printing ink jetting settings	155
A.3.2	CV	157
A.3.3	LSV	158
A.3.4	EIS	159
A.4	Pinch Value	162
	Appendix B IrNi EDX Spectra	163
	Appendix C Additional IrO_x TKK Loading Results	165
C.0.1	SEM Images	165
C.0.2	Different Loading Pol. Curves	167

List of Tables

2.1	Dimatix print nozzle ideal ink properties	27
2.2	Ideal ink recipes for each nozzle and catalyst type	29
2.3	Cell components and corresponding thickness	45
2.4	Applied current and time for conditioning IrO _x cells and first Ir ₈ NiO _x cell (E1)	49
2.5	Applied current and time for conditioning subsequent Ir ₈ NiO _x cells (E5, E6)	50
3.1	CCMs printed for electrochemical and ex-situ testing using the Samba cartridges.	57
3.2	CCMs printed for electrochemical testing with changes to compression using the 10 pL cartridges. *Made by Manas Mandal.	58
3.3	T-tests between samples for layer thickness	62
3.4	Fitting parameter values for EIS performed at 0.1, 1 and 10 A along with the pseudo capacitance related to each respective CPE and the double layer capacitance from the previous CVs.	83
3.5	Cell HFR and ECSA with pinch changed to test the effect of no compression. These cells were printed with 10 pL cartridges.	86
4.1	Elementary composition of Ir ₈ NiO _x catalyst found by EDX for batches 1 and 2.	94
4.2	Ir ₈ NiO _x CCMs printed for electrochemical and ex situ testing using the Samba cartridges.	98
4.3	EDX elemental composition of Ir ₈ NiO _x before testing (CCM E2).	102
4.4	Calculated ECSA before and after pol. curves for the tested Ir ₈ NiO _x and IrO _x cells to compare ECSA and double layer capacitance with thickness and porosity. *For E5-E6 the values were assumed to be similar to that of E1.	108
4.5	Kinetic parameters obtained from Tafel plots for E1, E5, E6, ML15 and ML23.	115
4.6	Fitting parameter values for EIS performed at 0.1 A along with the pseudo capacitance related to each respective CPE and the double layer capacitance from the previous CVs.	121
4.7	HFR of Ir ₈ NiO _x and the IrO _x cells.	121

List of Figures

1.1	Schematic of the PEMWE MEA with components and reactions.	7
1.2	Example of the electrolysis polarization curve and the different regions of losses.	11
1.3	Example CV for a catalyst containing IrO _x .	12
1.4	Example of a Nyquist plot. Tests go from high to low frequency as the curve goes from low to high resistance.	14
1.5	a) Overall performance at 2 A/cm ² , and b) kinetic performance at 1.5 V for various studies. Cell architecture and catalyst vary. Testing was performed at 80°C except for Babic's which was at 60°C. References and catalysts used are Lewinski (Ir-NSTF) [46], Rozain (IrO ₂ Surepure Chemicals) [47], Bernt (IrO ₂ on TiO ₂ from Umicore) [13], Alia (IrO ₂ Alfa Aesar) [48], Hegge (IrO ₂ Alfa Aesar + IrO _x nanofibers) [49], Taie (IrO _x TKK) [12], Babic (IrO ₂ on TiO ₂ from Umicore) [50], Jang (IrO ₂ Alfa Aesar) [51], Buhler (IrO ₂ Alfa Aesar) [52].	18
1.6	Cost [42, 43] and amount mined/produced [75, 76] for each metal that can be combined with Ir along with Ir itself. Logarithmic axis are base 100.	20
1.7	Mass activity of IrNi catalysts compared to Ir or IrO _x catalysts from the corresponding article. References are Nong [81], Wang [62], Moghaddam [67], Pi [77], Feng [82], Lv [78], Chen [87].	22
2.1	Setup for measuring the kinematic viscosity of an ink.	31
2.2	Area where the ink is inserted and left to heat to 32 °C.	32
2.3	Measurement area of the viscometer showing the lines where the timer was started and stopped.	34
2.4	Inkjet printer with CCMs on vacuum plate.	38
2.5	Example of the catalyst layers coated on the gold plate along with the gold plated block used to transfer the force and electrical signal to the catalyst layer.	42
2.6	Setup for catalyst layer through-plane electrical conductivity tests under compression using 2-probe method.	43
2.7	a) Electrolyzer setup, b) Schematic of Electrolyzer setup.	47
2.8	Electrolyzer cell connected to the fuel cell test station for when doing CV tests. a) Actual setup, b) Schematic.	48
2.9	Example of a Nyquist plot with data fitted using an equivalent circuit. Tests go from high to low frequency as the curve goes from low to high resistance.	53
2.10	Equivalent circuit used to fit EIS data for PEMWE.	54
3.1	DLS light sensitivity distribution of the 1:1 PG:IPA IrO _x TKK ink made for the Samba cartridges.	56
3.2	DLS light sensitivity distribution of the 46.7% Pt/C TKK ink.	56

3.3	Optical microscope images at 20x magnification of the anode side of each CCM. a-p corresponds to ML11-ML26. Each column is a batch and each row is a different loading with 1 mg/cm ² at the top and 0.25 mg/cm ² at the bottom. Exposure and brightness was adjusted in each image to see cracks formed during printing.	59
3.4	SEM images of 5000x magnification IrO _x Layers. a) ML19 0.993 mg/cm ² , b) ML20 0.808 mg/cm ² , c) ML21 0.567 mg/cm ² , d) ML22 0.241 mg/cm ² . The faint grey lines above the catalyst layer were the guidelines used to indicate where measurements were taken.	61
3.5	Catalyst layer thickness depending on the the IrO _x TKK loading using both SEM images and stylus profilometry. Error bars are the standard deviation.	62
3.6	Calculated porosity of SEM imaged and tested catalyst layers. Measured thickness was used for ML19-ML22 and calculated theoretical thickness was used for the remaining cells.	63
3.7	SEM images of ML19-ML22 (a-d) at 20000x magnification showing the internal structure of the IrO _x catalyst layer.	64
3.8	SEM images of ML19, 0.993 mg/cm ² IrO _x TKK at a) 1000x, b) 500x, c) 200x, d) 100x.	65
3.9	CV curves for each cell showing the stable 11 th cycle from 0-1.5 V. a) ML12-ML14, b) ML15-ML17, c) ML23-ML26	68
3.10	ECSA comparison between all cells separated by batch before and after polarization curves.	69
3.11	CV curves for each cell showing the stable 11 th cycle from 0-0.4 V to show the electric double layer region. a) ML12-ML14, b) ML15-ML17, c) ML23-ML26	70
3.12	Double layer capacitance comparison between all cells separated by batch before and after polarization curves.	71
3.13	Polarization and iR-free curves of batch ML12-ML14.	73
3.14	Polarization and iR-free curves of batch ML15-ML17.	73
3.15	Polarization and iR-free curves of batch ML23-ML26.	74
3.16	Polarization and iR-free curves of the ≈0.75 mg/cm ² cells ML13, ML17 and ML25.	74
3.17	iR-free overpotentials at 2 A/cm ² [12, 57].	75
3.18	Butler-Volmer plots for a) ML12-ML14, b) ML15-ML17, c) ML23-ML26	77
3.19	Tafel slope comparison between all cells in this work and Taie et. al. loading study [12].	78
3.20	Comparison of exchange current density normalized by the mass of catalyst. Taie et. al. [12], Mandal et. al. [28].	78
3.21	Nyquist plots for each batch of cells at 0.1 A from 100 kHz to 20 mHz. a) ML12-ML14, b) ML15-ML17, c) ML23-ML26	81
3.22	Frequency vs real and imaginary components of the impedance for each batch of cells at 0.1 A from 100 kHz to 20 mHz. - Im(Z) vs log(freq) a) ML12-ML14, c) ML15-ML17, e) ML23-ML26. Re(Z) vs log(freq) b) ML12-ML14, d) ML15-ML17, f) ML23-ML26	82
3.23	Pseudo capacitance for the first (C ₂) and second (C ₃) semicircles from the Nyquist plots at 0.1 A compared to the double layer capacitance from the CVs.	83

3.24	Nyquist plots from EIS simulations to show the effect of changing Q_3 . Q_3 is in units of $F \cdot s^{a-1}$. Parameters kept constant are $L=8E-9$ H, $R_1=0.011 \Omega$, $Q_2=0.33 F \cdot s^{a-1}$, $a_2=0.9$, $R_2=0.014 \Omega$, $a_3=0.9$, $R_3=0.14 \Omega$	84
3.25	R_{ct3} for each cell when the EIS applied current is 0.1, 1 and 10 A.	84
3.26	HFR comparison between all cells separated by batch.	85
3.27	SEM image of cell ML15 after testing showing the indentations created by the PTL pushing into the CCM.	86
3.28	Cell polarization curves for pinch values of 67 and -8 μm	87
3.29	Sheet resistance as a function of the catalyst layer thickness.	88
3.30	IrO_x TKK catalyst layer through-plane conductivity as a function of pressure.	89
4.1	TEM/EDX results for Ir_8NiO_x batch 1 at a 200 nm scale. a) TEM image, b) Ir, c) Ni, d) Cl, e) K, f) O	93
4.2	TEM/EDX results for Ir_8NiO_x batch 2 at a 1 μm scale. a) TEM image, b) Ir, c) Ni, d) Cl, e) K, f) O	94
4.3	DLS light intensity distribution for Ir_8NiO_x from batch 1 in water.	96
4.4	DLS light intensity distribution for Ir_8NiO_x from batch 2 in water.	96
4.5	DLS light sensitivity distribution for Ir_8NiO_x ink with 2.33 PG:water mass ratio.	98
4.6	Optical microscope images at 20x magnification of a) E1, 0.99 mg/cm^2 Ir_8NiO_x and b) ML23, 1.007 mg/cm^2 IrO_x TKK	99
4.7	Optical microscope images at 80x magnification of a) E1, 0.99 mg/cm^2 Ir_8NiO_x and b) ML23, 1.007 mg/cm^2 IrO_x TKK	99
4.8	SEM images at 5000x magnification before testing of a) E2, Ir_8NiO_x 0.99 mg/cm^2 , b) ML19, IrO_x TKK 0.993 mg/cm^2 where the vertical direction displays the 3 cross sections used to estimate the thickness of each catalyst layer.	101
4.9	EDX of Ir_8NiO_x CCM E2 at 2000x magnification. a) SEM image, b) C, c) Cl, d) F, e) Ir, f) K, g) Ni, h) O, i) S.	103
4.10	Conditioning curves over time for each of the three tested Ir_8NiO_x cells and the two tested IrO_x cells. All cells have the same current steps up until the 4th current step at 0.2 A which changes to 1 A for E1, ML15 and ML23 and 0.8 A for E5 and E6.	105
4.11	CVs of the three Ir_8NiO_x cells (E1, E5, E6) and two IrO_x cells (ML15, ML23) before and after doing the polarization curves. a) Entire graph, b) Zoomed in on the Ir_8NiO_x curves for a better view.	108
4.12	Methods of increasing the surface area of the catalyst particles/agglomerates and the catalyst layer.	109
4.13	E1 0.99 mg/cm^2 polarization curves compared to IrO_x cells ML15 and ML23.	111
4.14	E5 and E6 1.005 mg/cm^2 polarization curves compared to IrO_x cells ML15 and ML23.	111
4.15	a) Pol. curves of the Ir_8NiO_x and IrO_x cells where the current is normalized by the ECSA. b) Zoomed in area for clarity at low specific current densities. Legend is the same for both a) and b).	113
4.16	Butler-Volmer plots for E1, E5, E6, ML15 and ML23.	115
4.17	Plots from EIS tests for Ir_8NiO_x (E1, E5, E6) and IrO_x TKK (ML15, ML23) at 0.1 A. a) Nyquist Plot, b) $-Im(Z)$ vs $\log(freq)$, c) $Re(Z)$ vs $\log(freq)$. b) and c) are used to show relation to frequency so all data is present.	120

4.18	EIS curves for Ir ₈ NiO _x (E1, E5, E6) at 0.1, 1 and 10 A. a) Nyquist Plot, b) -Im(Z) vs log(freq), c) Re(Z) vs log(freq). b) and c) are used to show relation to frequency so all data is present.	122
4.19	Pol. curves showing the breakdown of losses a) E1 vs ML15 and ML23, b) E5 and E6 vs ML15 and ML23. c) Overpotential of each cause of voltage loss compared across E1, E5, E6, ML15 and ML23 which stack to form the total overpotential experienced at 2 A/cm ² .	123
4.20	SEM at 200x magnification of the surface of tested Ir ₈ NiO _x and IrO _x (ML15) CCMs, a) E1, b) E5, c) E6, d) ML15.	126
4.21	SEM at 1000x magnification of the interface of tested Ir ₈ NiO _x and IrO _x CCMs, a) E1, b) ML15.	126
4.22	SEM (left) and EDX (right) showing the catalyst layer surface and Iridium signal of the remaining tested Ir ₈ NiO _x catalyst layer, a) E1, b) E5, c) E6.	127
4.23	The average hydrodynamic diameter after each test given in the list above.	131
A.1	Triple distillation of water apparatus.	153
A.2	Zeitfuchs Cross-arm Viscometer Certificate of Calibration.	154
A.3	Cartridge settings for inkjet printing. a) waveform choice and piezoelectric voltage, b) cartridge temperature and nozzle settings, c) cleaning settings.	155
A.4	Multi-pulse waveform.	156
A.5	The setting parameters filled out to obtain a CV.	157
A.6	The setting parameters filled out to obtain a LSV.	158
A.7	The setting parameters filled out to obtain the first EIS curve at 0.1 A.	159
A.8	The setting parameters filled out to obtain the second EIS curve at 1 A.	160
A.9	The setting parameters filled out to obtain the third EIS curve at 10 A.	161
A.10	Schematic of MEA components pressing on the polymer membrane and catalyst layers at different distances to create the pinch.	162
B.1	EDX spectra for the surface of E2, Ir ₈ NiO _x 0.99 mg/cm ² .	164
C.1	SEM images of ML20, 0.808 mg/cm ² IrO _x TKK at a) 1000x, b) 500x, c) 200x, d) 100x.	165
C.2	SEM images of ML21, 0.567 mg/cm ² IrO _x TKK at a) 1000x, b) 500x, c) 200x, d) 100x.	166
C.3	SEM images of ML22, 0.241 mg/cm ² IrO _x TKK at a) 1000x, b) 500x, c) 200x, d) 100x.	166
C.4	Pol. curves and iR-free pol. curves for 0.25 mg/cm ² cells.	167
C.5	Pol. curves and iR-free pol. curves for 0.5 mg/cm ² cells.	167
C.6	Pol. curves and iR-free pol. curves for 1 mg/cm ² cells.	168

Chapter 1

Introduction

1.1 Motivation

Climate change continues to be one of the most pressing challenges that the world is facing. To help combat the effects of CO₂ and other greenhouse gas emissions, many countries have put in place climate action plans to try and reduce emissions. Twenty-six countries have proposed to have net-zero emissions by 2050 [1]. In March of 2022, Canada released their vision to reduce emissions to 40-45% below 2005 levels by 2030 [2]. To achieve this requirement there will need to be substantially more investment in, and improvement of, renewable energy technologies and energy storage. Renewable sources, such as wind and solar, have the downside of being intermittent since it is not always windy, nor is it always sunny. This intermittency occurs on both small, as the weather changes day to day, but also on a large scale through seasonal patterns. To make up for the times where there is less renewable energy available, the wind and solar energy that is generated needs to be stored for later use.

There are many methods that can be used to store renewable energy which include pumped hydro, batteries, hydrogen, and flywheels [3]. The Fraunhofer Institute for Solar Energy Systems [4] detailed how much potential energy each method could store along with how long it could discharge. Hydrogen storage has a large capacity, i.e. about 10 MWh to 100 GWh, and a variable discharge rates from days to months, making it an ideal candidate for seasonal energy storage.

In addition to energy storage, hydrogen can also be used in other processes

including transportation, metal production, ammonia, fertilizer, synthetic fuels and chemical processes which means that when produced from a renewable source can have the potential to decarbonize multiple sectors [5].

Hydrogen produced with renewable energy is known as green hydrogen. It is produced by water electrolysis which simply takes water and uses electricity to split the water into hydrogen and oxygen through a chemical reaction, as will be explained further in section 1.2. Currently there are four main types of water electrolysis cells categorized into high and low temperature operation. High temperature systems consist of solid oxide electrolyzers [6]. At low to moderate temperatures, technologies include alkaline (fluid electrolyte) [7], proton exchange membrane (PEM) [8] and anion exchange membrane (AEM) [9] electrolyzers which have the advantage of quick ramp up times. Being able to operate quickly and flexibly is important due to the intermittency of renewable sources.

PEM water electrolyzers (PEMWE) have the advantages of a compact design due to the solid polymer membrane, they can operate with hydrogen back pressure and at higher current densities [5]. Additionally, operating at low temperatures allows for a faster ramp up time than high temperature methods. PEMWE's also create the high purity hydrogen that is required for low temperature fuel cells and other processes [10]. The primary downside to the PEMWE is the use of precious metals such as iridium and platinum as catalysts for the chemical reactions which are scarce and costly. While increased production can benefit from the component cost cuts associated with "economies of scale", catalyst costs remain constant due to the small supply of iridium and platinum [11]. The only way to reduce the cost of the catalyst is to reduce the amount of precious metals used (i.e. the loading). It has been reported that only about 7.25 tons of Ir is produced each year and that even using half of this amount per year for PEMWEs would not be sufficient to meet energy demands at current catalyst loadings [12]. It has been proposed that to have a meaningful impact on energy storage and, for example use green hydrogen to displace fossil fuels in the transportation sector, it would require an Ir loading of just $0.01 \text{ mg}_{Ir}/\text{W}$ which corresponds to a geometric

loading of $0.05 \text{ mg}_{Ir}/\text{cm}^2$ at 1.79 V [13, 14]. Other perspectives put forward include conservative and optimistic estimates of 0.1 and $0.04 \text{ mg}_{Ir}/\text{W}$ at 1.58 V by 2050 which correspond to $0.23 \text{ mg}_{Ir}/\text{cm}^2$ and $0.1 \text{ mg}_{Ir}/\text{cm}^2$, respectively [15]. These required loadings are far lower than presently available commercial electrolyzers, which have loadings of about $2 \text{ mg}_{Ir}/\text{cm}^2$. Thus, the study of the reduction in Ir catalyst loading within PEMWEs must be explored further.

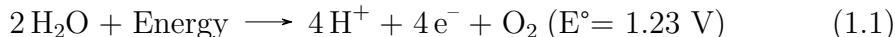
The focus of this thesis will be on PEMWEs and how to reduce Ir catalyst loading.

1.2 Function and Characterization of PEMWE

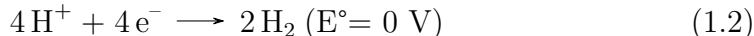
This section will explore what an electrolyzer is, what it does, and how it can be tested and characterized.

1.2.1 Chemistry

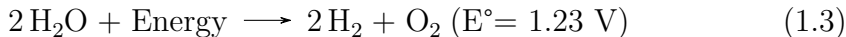
An electrolyzer operates by utilizing electricity from an external source to "split" water into its components, hydrogen and oxygen gas. Oxygen, protons (H^+) and electrons are produced through the oxygen evolution reaction (OER) (Equation 1.1),



at the anode. The protons migrate through a proton exchange membrane (typically Nafion) and are reduced by the electrons at the cathode through the hydrogen evolution reaction (HER) (Equation 1.2),



which is considered the reversible hydrogen electrode (RHE) with a reaction potential of 0 V . The overall reaction is then (Equation 1.3),



which occurs at 1.23 V vs RHE under standard conditions. This reaction potential changes with temperature and pressure as described by the Nernst

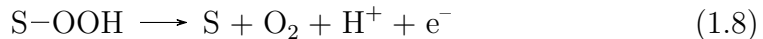
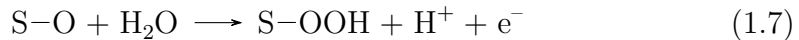
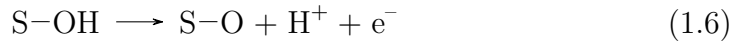
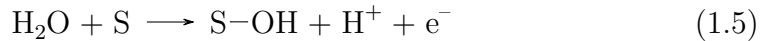
equation,

$$E(T, P) \approx E^\circ + \frac{\Delta S^\circ_{rxn}(T - T^\circ)}{nF} - \frac{RT}{nF} \ln \left(\frac{\prod_i^P (a_i)^{\nu_i}}{\prod_j^R (a_j)^{\nu_j}} \right) \quad (1.4)$$

where E° is the standard cell potential, ΔS° is the change in standard entropy for the reaction, T is the temperature, T° is the standard temperature (25°C), n is the number of electrons transferred in the reaction, F is Faraday's constant, R is the universal gas constant, a is the activity of a reactant or product, and ν is the stoichiometric coefficient for a given species. The activity of water as a pure liquid is 1 and the activities of the hydrogen and oxygen gas are governed by their partial pressures compared to the standard pressure at 1 atm.

The OER is slow, and requires an electrocatalyst to decrease the activation energy [8]. Typically Ir based catalysts are used for the OER under acidic conditions and platinum based catalysts for the HER. As such, the anode will be the focus of this work.

The OER occurs at the interface between the catalyst, ionomer Nafion, and the reactant water. The catalyst acts as a place for intermediate reactions to occur as the water is split into protons, electrons and oxygen. The catalyst can then transfer the electrons while the ionomer transfers the protons. There are many proposed mechanisms for the OER [16, 17]. One proposed mechanism is given in Eqns 1.5 - 1.8 where S is an active site on the catalyst layer [18].



For the catalyst to be the most effective, the effect on the adsorption of species cannot be too strong or too weak as outlined by Sabatier's principle

[18]. If the adsorption is too weak then the intermediates do not form on the catalyst and the reaction does not proceed. If the adsorption is too strong then once the intermediate forms on the catalyst layer it will not leave the catalyst blocking any further reaction from occurring. This can also be seen in a volcano plot by Fan et. al. [19] which shows IrO_2 , RuO_2 , and $\text{Ti}(\text{Ir})\text{O}_2$ as catalysts with a good balance of intermediate binding. Although the activity of Ir and Ru based catalysts are similar, Ir based catalysts are used over Ru due to IrO_2 's durability in the acidic environment created by the OER [20, 21].

1.2.2 The Membrane Electrode Assembly

To perform water electrolysis with a proton exchange membrane, a PEMWE cell is required which is known as a membrane electrode assembly (MEA). These MEAs are made up of the following components: the solid polymer electrolyte membrane; anode and cathode catalyst layers; porous transport layer (PTL); gas diffusion layer (GDL); microporous layer (MPL); and a bipolar plate for both anode and cathode. Figure 1.1 shows the layout of the PEMWE and the reactions at both anode and cathode.

The bipolar plates are made out of titanium for the anode side and graphite for the cathode side. These plates work as the current collectors which transfer electrons to and from their respective sides of the cell; they also contain flow channels for the initial transport of water to the cell as well as excess water and oxygen out of the anode side, and excess water and hydrogen out of the cathode side of the cell.

The material used for a PTL is typically titanium or platinized titanium. The PTL transports water to the anode catalyst layer as well as allows oxygen to move back through it to leave the cell. This movement of oxygen is important as the build up of gas in the layer can reduce the amount of water able to reach the catalyst, therefore reducing the efficiency of the cell. The PTL also transports electrons from the bipolar plate to the anode catalyst layer. Having good contact between the PTL and catalyst layer allows for lower charge transport losses and more of the layer to be utilized.

The cathode GDL is made of carbon paper. On one side it contains an extra layer which is the MPL. The GDL/MPL are attached in one layer and is placed on the cathode side to transport the hydrogen gas out of the cell as well as conduct electrons for the HER. The MPL is facing the catalyst layer as its purpose is to decrease contact resistance between the GDL and the catalyst layer [22].

The polymer electrolyte membrane is made of an ionomer known as Nafion. Nafion is a sulfonated tetrafluoroethylene-based polymer which contains sulfonic acid groups that are able to transport hydrogen ions (protons) across it while being insulative to electrons. Since it is a solid structure, yet still quite thin, it separates the two sides of the cell while allowing the cell to be compact. These membranes come in many different thicknesses where the general trade-off is that thicker membranes have less hydrogen crossover but have more ohmic resistance. Hydrogen crossover is when the hydrogen from the cathode side comes back through the membrane to the anode side which can decrease the efficiency of the cell and create an explosive mixture with oxygen creating a safety hazard [23]. Thinner membranes have the opposite effects, less ohmic resistance but can be prone to a higher chance of crossover.

Lastly there are the two catalyst layers comprised of Ir-based catalyst at the anode side and platinum supported on carbon (Pt/C) at the cathode side. Both layers contain an ionomer, typically Nafion, to bind the layer together and provide proton transport to and from the membrane. The catalyst layers are where the reactions occur with the OER at the anode on the Ir-based catalyst and HER at the cathode on the platinum. On the anode side electrons are transferred from the PTL to the anode catalyst layer and protons are transferred to the membrane by the Nafion. On the cathode side protons are received from the membrane through the Nafion and electrons from the MPL/GDL. The catalyst layers also required a porous structure to allow the transport of water and oxygen at the anode, and hydrogen at the cathode. As stated before Ir-based catalysts are used specifically for their high activity and durability [8, 20, 21].

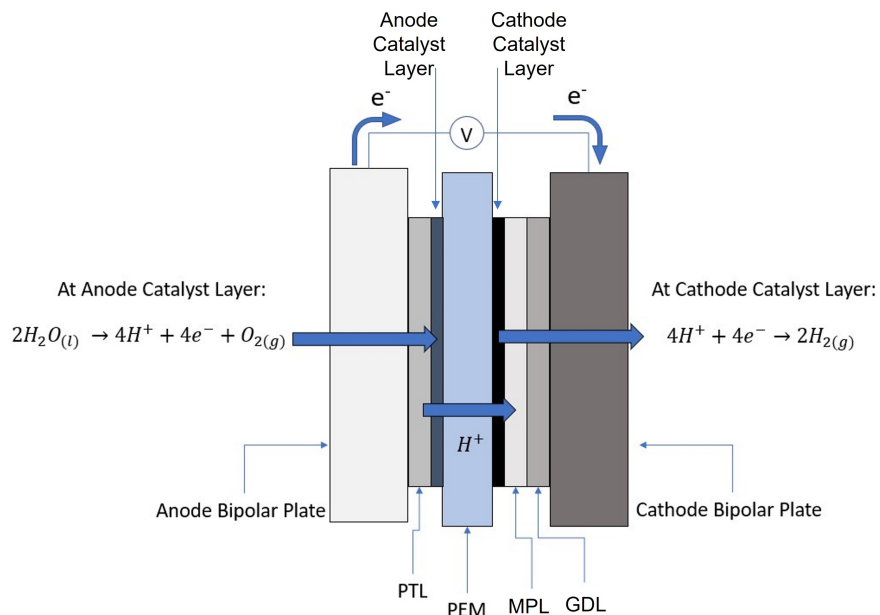


Figure 1.1: Schematic of the PEMWE MEA with components and reactions.

1.2.3 Catalyst Layer Fabrication Method

The catalyst layer can be applied to an MEA in two ways. The first is to print the catalyst onto the membrane making a catalyst coated membrane (CCM) and the second is to print the catalyst onto the PTL or GDL which is known as a gas diffusion electrode (GDE), catalyst coated substrate (CCS) or porous transport electrode (PTE).

It has been found for PEM fuel cells that the CCM method provides better performance [24, 25]. There have been attempts to use GDE/CCS for PEMWE [26, 27] which used electrodeposition to deposit the catalyst onto the PTL. Following fuel cells, in PEMWE the most popular way to deposit the catalyst is directly coating the membrane (the CCM method) [12, 28–31].

There are a few different ways to deposit the catalyst onto a PEM to create a CCM. Possible techniques include Dr. Blade, hand painting, spray coating and inkjet printing [32–35]. Each has benefits and drawbacks as to their use.

Inkjet printing offers two main advantages: precision in loading and in placement. This means that catalyst layers can be accurately deposited in any area or shape within the bounds of the printer while allowing for small loadings

with good uniformity when using an optimized catalyst ink [28]. Additionally, inkjet typically does not require a large amount of ink and catalyst compared to other methods. It only takes about 2 mL to print multiple CCMs of 1 mg/cm².

Other benefits of inkjet printing include the increase in layer height compared to aerosol spraying which could improve layer porosity and the smoothness of the layers [35]. In turn the increased porosity should improve mass transport.

The main downside to inkjet printing is the possibility of nozzles being clogged by agglomerates. This can be improved by ensuring particle size is low and that the colloid is stable and does not settle quickly.

In this work, inkjet printing will be used where the catalyst is directly applied to the membrane to make CCMs which will be assembled into MEAs. This will provide well tuned catalyst loading and uniform catalyst layers while using small amounts of catalyst ink.

1.2.4 Performance and Characterization

Once the MEA is made, there are various ways to characterize and define the performance of the cell and its components. These include in situ techniques such as polarization curves (pol. curves), linear scan voltammetry (LSV), electrochemical impedance spectroscopy (EIS) and cyclic voltammetry (CV) [36]. Ex situ tests such as energy dispersive X-ray spectroscopy (EDX/EDS), scanning electron microscope (SEM), transmission electron microscope (TEM), optical microscopes, and conductivity tests can be used to see physical characteristics of the catalyst layers [36]. Each of the in situ electrochemical characterization methods will be explained briefly as well as why testing in a cell is important.

Polarization Curves

Polarization curves show the overall performance of a cell as it defines the current that a particular applied voltage can produce or vice versa. This provides the amount of power required to run the electrolyzer cell. Ideally the pol.

curve would be flat at 1.23 V since this is the theoretical potential for water electrolysis. There are three distinct regions to a pol. curve that provide information on different processes that occur during operation corresponding to losses in performance, causing the deviation from the ideal curve. The difference between the actual potential and the theoretical potential is known as the overpotential, which will ideally be minimal. High overpotentials decrease the efficiency of the electrolyzer, requiring more voltage or higher catalyst loading to reach the same performance. Figure 1.2 shows an example pol. curve as well as the regions where particular losses occur.

The first is the low current range where the kinetic losses of the reaction dominate. Kinetic losses consist of the activation energy to start the reaction for both the anode and cathode. Due to the low activation energy of the HER at the cathode, the anode OER losses dominate. Since the OER losses are dominant they can be studied by performing another technique, LSV. LSV can be used to generate a current vs voltage plot by changing the voltage at a constant rate from low to high and measuring the corresponding current. The voltage scan rate must be small enough to have a good resolution to look at the small current ranges at which the kinetic processes occur. By looking at this region the kinetic parameters can be found which provide information about the catalyst activity and associated losses. The general equation is the Butler-Volmer (BV) equation,

$$i = i_0 \left(-e^{\frac{-\alpha_c F \eta}{RT}} + e^{\frac{\alpha_a F \eta}{RT}} \right) \quad (1.9)$$

where i is the current density measured during the LSV, i_0 is the exchange current density, α_c is the cathode transfer coefficient, α_a is the anode transfer coefficient, F is Faraday's constant, η is the overpotential found by subtracting 1.179 V (ideal potential at 80 °C) from the applied potential, R is the ideal gas constant and T is the temperature of the cell [36]. The sign convention from the typical BV equation was switched to say that a positive current was generated when applying voltage.

The kinetic parameters within the BV equation are normally estimated

by using the Tafel equation seen in its simplest form in Eqn. 1.10 [36]. The assumptions to use this equation are that the overpotential is high ($>0.1V$), there is only one electron transferred during the reaction, and the process is a one step reaction that is irreversible [36]. In the case of water electrolysis the reaction is a complex four electron transfer process which is why this is considered an estimate. Using these approximations the BV equation can be simplified to the Tafel equation,

$$\eta = \frac{2.3RT}{\alpha_a F} \log(i_o) - \frac{2.3RT}{\alpha_a F} \log(-i) \quad (1.10)$$

where the 2.3 constant is added for the purpose of changing from an original natural log base to a log 10 base. The Tafel slope is given by Eqn. 1.11 which is found by using overpotential on the y-axis and $\log(i)$ on the x-axis and provides information about the reaction rate or how much voltage is required to increase the rate of reaction [36]. In addition the exchange current density represents the activity of a catalyst as it relates to a higher reaction rate. New catalysts are explored to ensure that the most active catalysts are being utilized. The activity of the catalyst can be expressed in either A/cm^2 or A/g_{cat} .

$$Slope = \frac{2.3RT}{\alpha F} \quad (1.11)$$

Following the kinetic region is the linear ohmic region. In this region the ohmic losses are dominant following Ohms law ($V=IR$). Ohmic losses consist of the overall resistance of each component. Ohmic losses are due to the electrons going through the PTL, GDL/MPL and the catalyst layers, contact resistance between these components and the catalyst layers, as well as the proton transport through the Nafion membrane and catalyst layers.

Finally, at high current density there can be mass transport losses which occur when there is insufficient water brought to the electrode and when oxygen bubbles can not escape the catalyst layer. The structure of the catalyst layer is important as low porosity or pore size in the catalyst layer and trapped bubbles can impede the flow of water.

If a catalyst has a high enough activity the losses due to charge and mass transport may dominate. If this is the case, reducing the catalyst loading (which can reduce the catalyst layer thickness) may be beneficial since there is a reduced transport length.

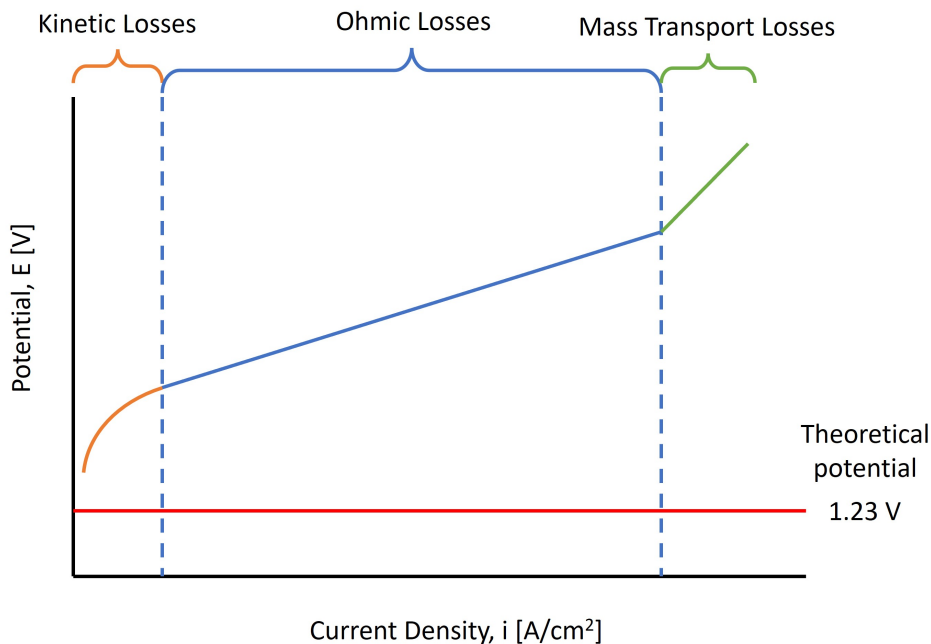


Figure 1.2: Example of the electrolysis polarization curve and the different regions of losses.

Cyclic Voltammetry

Cyclic voltammetry (CV) is performed by sweeping the voltage at a given scan rate in mV/s forward and backwards for one or multiple cycles [36]. CV can be used to estimate the electrochemical surface area (ECSA) of the catalyst layer and double layer capacitance (C_{dl}). Peaks will form along the curve where oxidation (positive current) and reduction (negative current) of species occur [36]. Figure 1.3 shows an example CV for an IrO_x catalyst. IrO_x contains some Ir(III) and Ir(IV) so when the CV starts a peak forms first due to the oxidation of Ir(III) to Ir(IV) at about 0.8 V followed by a second peak due to Ir(IV) to Ir(V) around 1.2 V. Following the second peak the OER begins at about 1.5 V as seen by the sharp increase in current. On the backwards sweep if there is a negative peak, mirrored over the x-axis from the positive

peak, then the reaction is reversible. If the peaks are offset then the reaction is partially reversible as is seen in Figure 1.3. These negative peaks represent a reduction of the Ir which brings the Ir back from Ir(V) to Ir(IV) and then Ir(IV) to Ir(III). ECSA is proportional to the area under the curve from 0.4 to 1.25 V, as found by Tan et. al. [37]. For a given catalyst, the catalyst layer double layer capacitance is usually proportional to the ECSA. The double layer capacitance can be found using the equation [36],

$$C_{dl} = \frac{(\frac{\Delta l}{2})}{\nu} \quad (1.12)$$

where Δl is the current gap between the oxidation and reduction sweeps at the flat region of the CV, in this case about 0.2 V, and ν is the scan rate in V/s. The double layer capacitance is another indicator of the catalyst area within the catalyst layer.

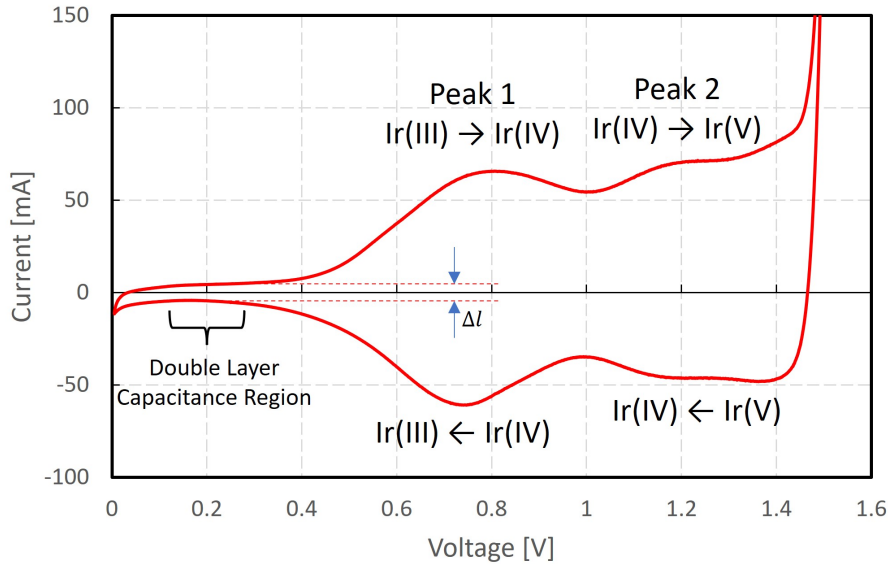


Figure 1.3: Example CV for a catalyst containing IrO_x .

Electrochemical Impedance Spectroscopy

Electrochemical impedance spectroscopy (EIS) is a process that is used to find the timescales for different physical phenomena occurring in a PEMWE [36]. Impedance is measured at different potentials by perturbing the cell with a sinusoidal current/voltage input and measuring the voltage/current response at different frequencies. The impedance is then obtained as the voltage to current ratio and is broken down into real and imaginary components as the ratio itself is a sinusoidal signal. The real component consists of ohmic resistances, while the imaginary component can contain inductive and capacitive effects. The impedance spectra is usually visualized using a Nyquist plot where the real and imaginary components are graphed on the x and y axes respectively [36]. On an example plot (shown in Figure 1.4) the first point on the x-axis is the high frequency resistance (HFR) which is also the ohmic resistance of the cell. This represents the ohmic resistance because the capacitance effects do not show an impedance at high frequencies so in this region only the ohmic resistance is found [36]. The larger the HFR, the more losses there are in the ohmic region. The real component of the diameter of the curve gives the charge transfer resistance, or in the case of Figure 1.4, where there are multiple portions of the curve then there might be more than one charge transfer resistance. The larger the charge transfer resistance, the slower the reaction is. Additionally, the double layer capacitance of the catalyst layer can be found from the peak of each section [36].

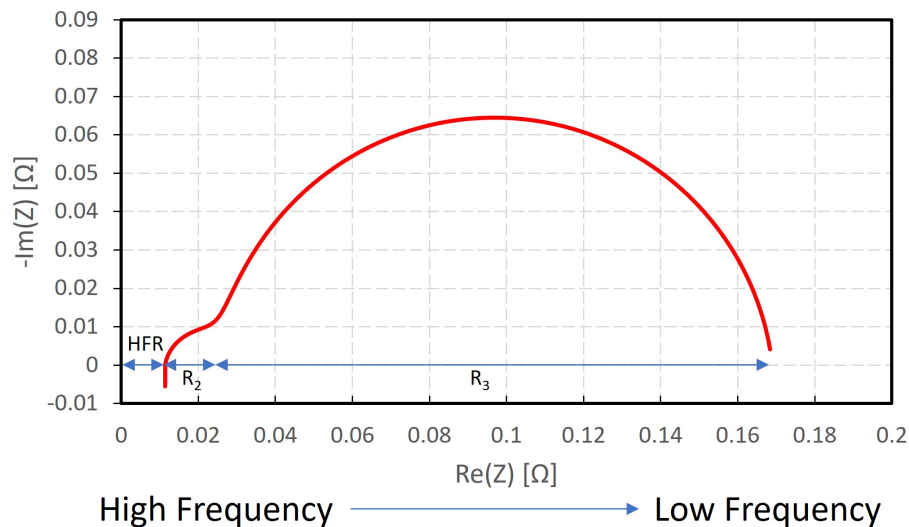


Figure 1.4: Example of a Nyquist plot. Tests go from high to low frequency as the curve goes from low to high resistance.

RDE vs Cell Testing

OER catalysts are tested in RDEs and MEAs, but there are major differences between the two methods that need to be explored. The differences will help explain why, even though promising catalysts have been shown in an RDE or three-electrode cell, there is still a need for further testing in an MEA.

RDEs are used for initial catalyst characterization at low current densities usually below 10 mA/cm^2 . MEA allows for testing in more realistic operating conditions and higher current densities. However, MEAs tend to not perform as well as an RDE per gram or per active site of catalyst [14]. The changes in performance are due to the RDE operating in low current density, using rotation to minimize mass transport losses (the action of spinning brings more reactant to the surface), as well as the thinner catalyst layer being in contact with a liquid electrolyte, therefore having better ion transport. In an MEA the layers are usually thicker due to using a higher loading (100's of μg to mg scale) and depend on the structure of not just the individual catalyst particles, but the entire catalyst layer to determine the transport of water, oxygen, electrons and protons. Requiring a larger amount of catalyst, along with equipment and extra setup, hinder the use of MEAs as well, in favour of RDE testing for initial

screening [38]. Further, if the catalyst has a low electrical conductivity, the losses are more pronounced in an MEA due to the thicker layer and contact resistance with a PTL. In comparison, in an RDE the layer is so thin that these effects are minimized [39].

The membrane of the MEA can also cause losses which are not seen in RDE testing. Ion transport from the catalyst layer into the membrane could deteriorate the membrane and cause poisoning, possibly limiting the proton transport and therefore increasing losses [40].

While the performance of the RDE is better than in an MEA, the durability of the catalyst has been found to be less when using RDEs due to oxygen bubbles blocking active sites over the long testing periods [41].

1.3 Literature Review

Currently, Ir-based catalysts are the best available to use for OER. As explained in section 1.2.1 Ir-based catalysts have superior activity while maintaining durability in acidic media [19–21].

Since Ir catalysts are expensive [42, 43], finding ways to reduce the amount of Ir used is essential for the further commercialization of PEMWEs [13–15]. This thesis will look at two different ways of approaching reduction of Ir loading. The first method of reduction is to simply reduce the loading of an Ir catalyst layer with low electrical conductivity and high activity. The second is to increase the activity of the Ir catalyst by combining Ir with another metal.

1.3.1 Variations in Loading

Ahadi [44] found that the through-plane conductivity of a catalyst layer can be up to three orders of magnitude less than the in-plane conductivity showing the need for more investigation of through-plane effects. Mandal et. al. [29] aimed to look at the through-plane electrical conductivity and found that Umicore Ir had higher electronic and protonic conductivity for similar Nafion volume fractions than IrO_x from TKK. Moore hypothesized that electrical conductivity might limit the performance of anode PEMWE electrodes [45]. If this is the case, decreasing the amount of iridium in the anode catalyst layer might improve cell performance by decreasing ohmic resistance and increase catalyst layer utilization. Moore et. al., then used this data to create a model in which he predicted where the catalyst layer is being utilized [45]. Based on the protonic and electronic conductivity, Moore’s model suggests that, for Umicore Ir, a large amount of catalyst layer was utilized whereas the more active IrO_x TKK utilized only a thin slice of the layer close to the PTL-CCM interface. So, the expected trend to see when reducing the loading of a catalyst with low electrical conductivity and high activity is a reduction of the slope in the ohmic region of polarization curves while maintaining the same kinetic performance therefore increasing overall performance.

Many loading studies have been done and show a variety of trends [12,

13, 46–52]. Figure 1.5 shows the overall cell performance at 2 A/cm² and the current density achieved at 1.5 V iR-free for different loadings in each study. The composition of the cell and the catalyst used determines the cell performance, which is why there is a wide range of voltages seen for cells at similar anode loadings. When loading decreases, it is common for the overall performance to decrease [12, 13, 46, 47, 49, 50, 53]; these losses might not be due to the low catalyst layer loading or activity, however, but due to poor connectivity within a layer at low loadings due to crack formation. Cracks could cause a decrease in the in-plane conductivity, particularly for electron transfer. In-plane conductivity was studied and, when low, has been shown to limit catalyst utilization as the reaction was observed to be not uniform across the catalyst surface [54–56]. Even though the overall performance decreases, it is not significant in the case of Babic [50], Lewinski [46] and Taie [12] until loadings are below 0.1 mg/cm².

Alia [48] found that the performance remained about the same over a small IrO₂ loading range of 0.1-0.4 mg/cm² which is promising.

Jang [51] observed improved performance with decreased loading, but the conductivity of IrO₂ from Alfa Aesar was not known. Jang attributed the increase in performance at low loadings to a decrease in layer thickness, allowing for less proton transport losses. However, it could be argued charge transport was limiting. Given that IrO_x TKK has a low electrical conductivity, according to Moore, this trend should also be observed. Taie [12] and Fujita [57] have both used IrO_x TKK at various loadings. Taie studied very low loadings of less than and equal to 0.17 mg/cm². Ultra low loadings between 0.026 and 0.17 mg/cm² had better performance than a commercial MEA with a 2.5 mg/cm² loading from Greenerity GmBH. However, when all the low-loading catalysts fabricated by the same process are compared, the overall performance decreased as loading decreases. Fujita fabricated CCMs from 0.1 to 1 mg/cm² and found that the performance at 2 A/cm² at 50°C is similar for all loadings above and including 0.3 mg/cm². Jang and Fujita’s results support the idea that current iridium loadings for active catalysts, such as IrO_x, are unnecessarily high and an optimum loading could be achieved that provides a better

trade off between catalyst layer activity and charge transport losses. This supports Moore’s model for IrO_x loadings between $0.3\text{-}1\text{ mg/cm}^2$. Perhaps there is a range of loadings where the decrease in ohmic losses is optimized.

In this work loadings of $0.25\text{-}1\text{ mg/cm}^2$ of IrO_x TKK will be printed using inkjet printing and tested in a PEMWE to determine if the trend Fujita showed is seen at 80°C and at current densities as high as 4 A/cm^2 , as well as validate the proposed hypothesis and numerical model. In addition further investigation will be conducted on the through-plane electronic conductivity of the anode catalyst layers.

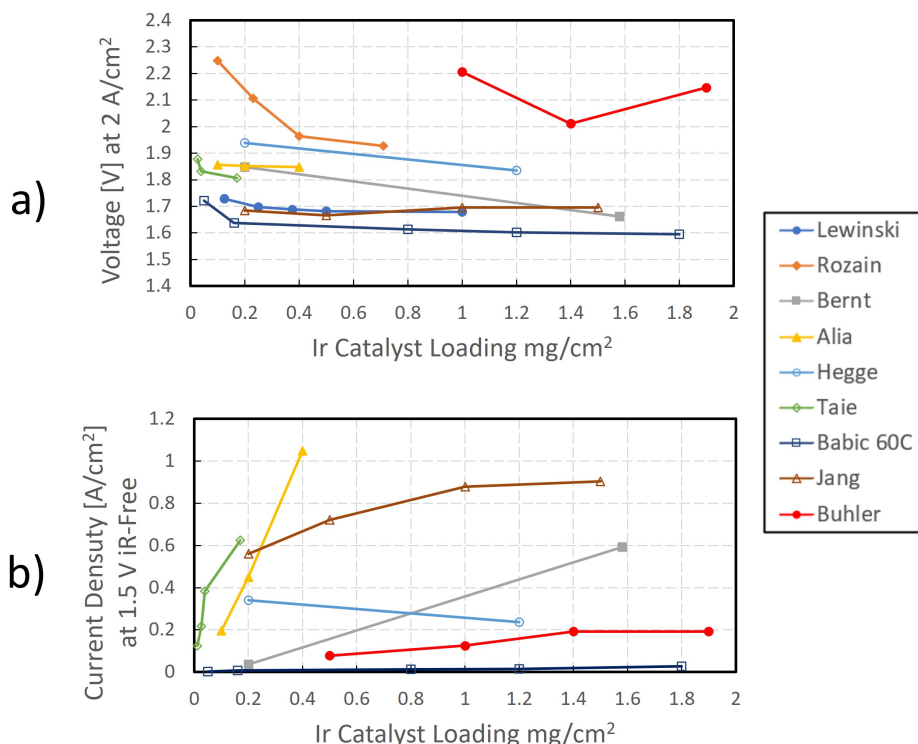


Figure 1.5: a) Overall performance at 2 A/cm^2 , and b) kinetic performance at 1.5 V for various studies. Cell architecture and catalyst vary. Testing was performed at 80°C except for Babic’s which was at 60°C . References and catalysts used are Lewinski (Ir-NSTF) [46], Rozain (IrO_2 Surepure Chemicals) [47], Bernt (IrO_2 on TiO_2 from Umicore) [13], Alia (IrO_2 Alfa Aesar) [48], Hegge (IrO_2 Alfa Aesar + IrO_x nanofibers) [49], Taie (IrO_x TKK) [12], Babic (IrO_2 on TiO_2 from Umicore) [50], Jang (IrO_2 Alfa Aesar) [51], Buhler (IrO_2 Alfa Aesar) [52].

1.3.2 Iridium Bi-Metallic Catalysts

Combining metals together has been done for thousands of years [58]. One of the most commonly known being the invention of the bronze by combining copper and tin [59]. Bronze is more durable than the initial metals used to create it [60]. Combining materials can enhance properties to exceed what can be done by the individual components. The enhancement of a metals properties is why looking at Ir bi-metallic catalysts could be beneficial to the enhancement of the water oxidation catalyst and reduce the Ir loading by replacing portions with another metal.

Two properties that could be enhanced when adding other metals to Ir is the d-band electronic structure [61] and the geometry of the catalyst [62]. The electronic band structure affects the catalysts binding energy with oxygen atoms and intermediates as they adsorb and desorb from the catalyst surface. The geometry can open new areas for active sites.

To improve the electronic structure as well as create different geometries, other D-Block elements have been combined with Ir, including manganese [63], platinum [64], gold [65], nickel [66, 67], cobalt [68–70], iron [62], rhodium [71], tungsten [72], copper [73] and ruthenium [74].

Of the metals that can be combined with Ir, it would be ideal for upscaling to choose one that is inexpensive, abundant, and has the best improvement in performance. Figure 1.6 shows the cost and abundance of each material.

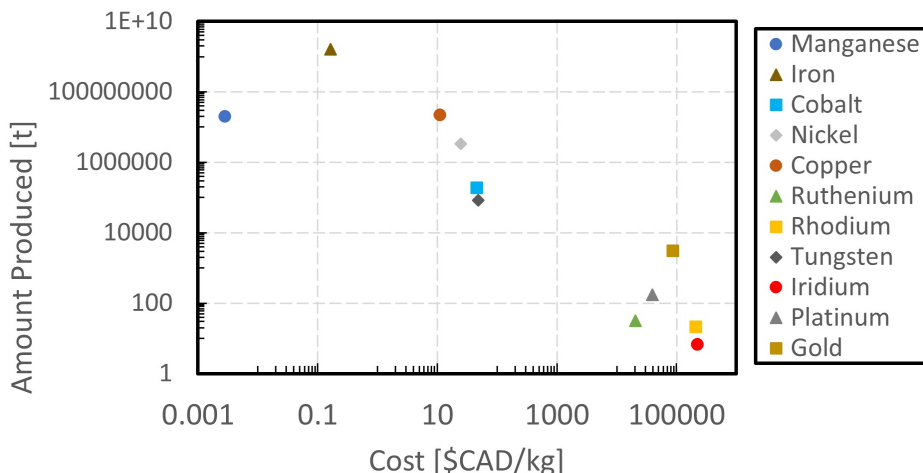


Figure 1.6: Cost [42, 43] and amount mined/produced [75, 76] for each metal that can be combined with Ir along with Ir itself. Logarithmic axis are base 100.

Inexpensive and abundant metals include Mn, Co, Ni, Fe and Cu. Co, Fe and Ni have been directly compared by Wang et. al. in an RDE [62]. They found that IrNi, IrCo, IrFe and IrO₂ had mass activities of 0.732, 0.475, 0.382 and 0.115 A/mg_{Ir} at 1.53 V, and overpotentials of 283, 295, 302 and 342 mV, respectively at 10 mA/cm². IrNi has the higher performance in terms of mass activity and Wang also found that it had the best durability. Wang explained this was due to the IrNi catalyst having the most stable adsorption geometries for oxygen intermediates. This means that the placement of the atoms allows for good binding with the intermediates. The geometry forms due to dealloying of the Ni off the surface of the Ir particles using acidic media. It improves the specific surface area of the catalyst which further promotes the OER.

Pi et. al. also compared IrCo, IrFe, IrNi and Ir in acidic media finding mass activities of 485, 557, 1203, and 492 A/g_{Ir} [77]. Again showing Ni to have the highest activity.

IrCu and IrNi was tested in a three-electrode cell by Wang [73] and Moghadam [67], respectively, in the same laboratory both using an aqueous alkaline synthesis method. Although they used different acidic solutions for testing the electrodes, H₂SO₄ for IrNi and HClO₄ for IrCu, they found similar activities for their catalysts of about 140 A/g_{Ir} compared to IrO_x which was 93 A/g_{Ir}

at 1.48 V. They also found overpotentials of 270, 260, 310 mV for Ir_8NiO_x , IrCu and IrO_x , respectively at 1 mA/cm².

Another comparison was made by Lv [78] between Ir, IrCo, and IrNi nanoflower catalysts using an RDE. They found a mass activity of 125, 168 and 379 A/g_{Ir} for Ir, IrCo, and IrNi nanoflowers, respectively at 1.51 V.

Other IrNi catalysts compared to Ir/IrO_x are given in Figure 1.7 where IrNi has higher activity compared to Ir/IrO_x catalysts from the corresponding paper. Overall it also appears that IrNi has greater activity than Ir or IrO_x. Due to increased activity, and possibly stability, Ni is suitable to combine with Ir compared to the other earth abundant elements. There are many ways to make an IrNi catalyst which come in various oxide forms and structures. The focus for the next part of this section will be on these synthesis methods for IrNi and determining which one should be used to make the IrNi catalyst which will be later tested in an MEA.

All of the IrNi catalysts listed previously have been tested in RDE's and other three-electrode cells which require less catalyst, on the μg scale, than an MEA, on the mg scale. As discussed in section 1.2.4, moving to MEA testing is required for future commercial use and there are performance differences that must be explored. When the work in this thesis began there were no known literature utilizing an IrNi catalyst in a PEMWE. As of 2023, there have been at least three articles utilizing a combination of Ir and Ni in a PEMWE [27, 79, 80]. As the amount of literature at this scale is small it is necessary to continue studying IrNi catalysts at the PEMWE scale.

There are many different synthesis processes used for the formation of IrNi alloys and bi-metallic catalysts which include the popular polyol method [81–85], physical mixtures [86, 87], alkaline aqueous reaction [67, 88, 89], high pressure reactor [77], electron beam co-evaporation [90] and melting metal down together [62]. For the IrNi synthesis, the process should be easily scalable.

The alkaline aqueous reaction was originally developed by Berkermann in his dissertation [91] where iridium chloride was mixed with KOH to create an oxide form. Moghaddam extended this method for use with Ni to make an IrNiO_x [67]. This is a simple synthesis method since it only requires the

addition of the two metal salts, IrCl_3 and $\text{NiCl}_2 \cdot 6\text{H}_2\text{O}$, and then is stirred for two days in a 0.1 M KOH solution. From Wang et. al., following centrifugation solid IrO_x , and IrNiO_x particles can be obtained [73]. Due to the simplicity of the alkaline aqueous reaction, it can be done with available equipment at room temperature with no extra calcination/heating steps, this will be the method used to study the up-scaling of IrNiO_x . Since MEA and RDE test conditions and electrode structure are different, it is difficult to predict if a well performing catalyst in an RDE will also perform well in an MEA so it is reasonable to extend the testing of the aforementioned promising IrNiO_x catalyst to an MEA setup.

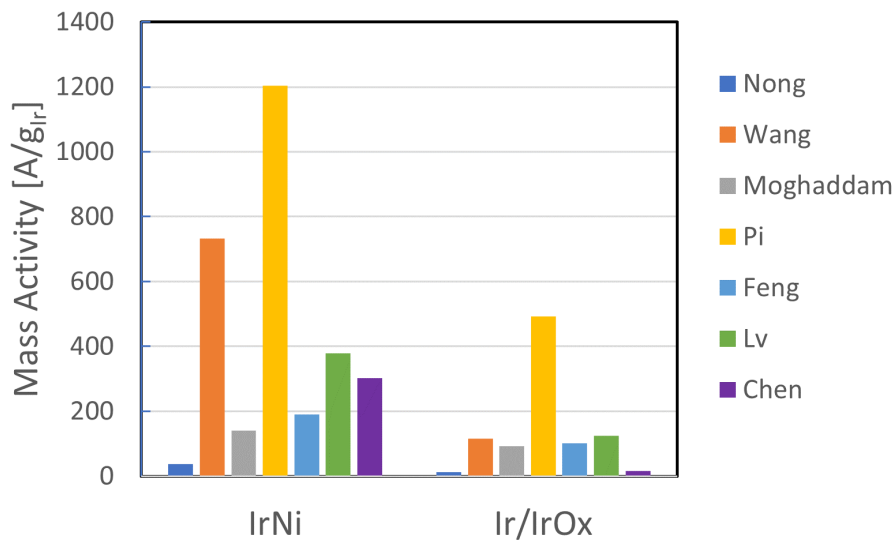


Figure 1.7: Mass activity of IrNi catalysts compared to Ir or IrO_x catalysts from the corresponding article. References are Nong [81], Wang [62], Moghaddam [67], Pi [77], Feng [82], Lv [78], Chen [87].

1.4 Thesis Objectives

The objective of this thesis is to reduce iridium loading in two ways.

1. Reduce the loading of IrO_x TKK catalyst layers to evaluate the effect of catalyst loading.
 - Research Question: Can reducing the loading of IrO_x TKK decrease ohmic losses while maintaining kinetic performance, in accordance with Moore's model?
 - Hypothesis: Smaller loadings produce similar or better performance on pol. curves due to same kinetic activity and decreased ohmic losses therefore validating Moore's model.
2. Evaluate the performance of an IrNi catalyst in a PEMWE.
 - Research Question: Does the incorporation of Ni increase the performance of an Ir based catalyst layer in a PEMWE while maintaining a stable catalyst layer structure?
 - Hypothesis: IrNi has increased overall performance due to enhanced activity.

Chapter 2

Methodology

2.1 Catalyst Synthesis

As discussed in Chapter 1, Ni has been shown to enhance the electrical properties of Ir catalysts for water oxidation. The goal of this work is to scale up the catalyst made by Moghaddam [67] and test its performance in an MEA. In the work done by Moghaddam [67] the reaction took place in a total volume of 22.5 mL using 59.7 mg of IrCl_3 and 3.2 mg of NiCl_2 precursors. For this work, the process was scaled up since about 100 mg of catalyst powder is needed to make an ink for inkjet printing. In addition, Moghaddam drop coated the catalyst directly from a dilution of the original reaction solution whereas here there is a need for precipitation of the catalyst so it can be re-dispersed in the appropriate solvents during ink preparation. This is where a modified procedure by Wang [73] was used to precipitate the Ir_8NiO_x particles. The following sections will go over the exact process used to prepare and run the reaction, as well as the precipitation of the Ir_8NiO_x catalyst particles.

2.1.1 Catalyst Preparation

Reaction

To synthesize the Ir_8NiO_x catalyst powder the method used by Moghaddam et. al. [67] was scaled up. First, 0.704 g of $\text{IrCl}_3 \cdot x\text{H}_2\text{O}$ (Pressure Chemical, PCC Item 5730) and 0.0646 g of $\text{NiCl}_2 \cdot 6\text{H}_2\text{O}$ (J.T.Baker Chemical Co., Prod. 2768, 98%) were combined in a 500 mL round bottom flask, giving an atomic ratio of 8:1 Ir:Ni which is why it is referred to in this work as Ir_8NiO_x . Next,

100 mL of triply distilled water (TDW) (See Appendix A.1 for distillation procedure) was used to disperse the solid. A magnetic stir rod was added to the flask and it was spun on a magnetic stir plate (Corning, PC-351) at the 3rd tick mark on the dial (≈ 100 rpm) until most of the solid at the bottom of the flask was suspended (About 5-10 min). Then 22.5 mL of 1 M KOH (Sigma-Aldrich, 99.99%, LOT: MKCD8556) was added dropwise in groups of 4-7 drops every 10 seconds using a pipette. The solution is initially brown and after the addition of KOH the colour becomes a dark purple. After KOH was added parafilm was placed on the top of the flask and 50 holes were poked into the parafilm using a needle. The purpose of this is to allow oxygen in. The solution was left on the magnetic stirrer at ≈ 100 rpm for at least two days to allow the reaction to go to completion.

Catalyst Powder Precipitation

The primary difficulty with making the catalyst was the scaling up of the process and attempting to precipitate enough catalyst to make an ink. This is due to the fact that the Ir_8NiO_x catalyst disperses very well in water. So, when cleaning of the catalyst is performed between centrifugation, tert-butanol must also be used or else the yield is incredibly small, likely only a few milligrams.

To precipitate the catalyst powder a modified method of the one found in the IrCu study by Wang et al. [73] was used. Before beginning to precipitate the catalyst, the flask was placed in an ice bath which had table salt (NaCl, Fisher Chemical, Certified ACS, LOT: 223105) added to it to further decrease the temperature to as low as -10 °C. To precipitate the powder, 250 mL of tert-butanol (Fisher Chemical, LOT: 224104) was added to the Ir_8NiO_x solution while continuing to stir for 10 mins. Then stirring was stopped and another 100 mL of tert-butanol was added. The solution was left to sit still for 30 min then poured equally into twelve 50 mL centrifuge tubes. The tubes were then centrifuged at 4500 rpm using a SX4400 attachment (Beckman Coulter, Allegra X-30R centrifuge) for 20 min with the temperature set to 0 °C. After centrifuging the supernatant was decanted into a 500 mL Erlenmeyer flask with a small portion of fluid, probably about 5 mL, remaining in each tube.

The solid which was left at the bottom of each tube was transferred to four of the tubes. Any solid remaining in the original flask was rinsed using 40 mL of supernatant which was spread across the four tubes. They were then all filled to about 40 mL each using the previous supernatant. The solid was re-dispersed by shaking the tubes. The four tubes were placed in a table salted ice bath for 10 mins. They were then centrifuged again at the same conditions as above. Once complete, the supernatant from each tube was decanted and the solids were transferred to just two tubes. 80 mL of a 80:20 tert-butanol:water by volume solution was prepared and added equally to each of the remaining two centrifuge tubes. They were again placed in a table salted ice bath for 10 min, then centrifuged again at the same conditions as before. After decanting the supernatant this final time, the two tubes were placed in a vacuum desiccator (Kimax with 40/35 Pyrex Brasil Lubricate) and run for two hours to dry the solid. The tubes were left in the desiccator until the powder was to be collected and used.

Powder Preparation

Once the catalyst was to be used, the centrifuge tubes were taken out of the desiccator and the solid was scraped into a mortar. Using the mortar and pestle the solid was ground into a fine powder that was then scraped out of the mortar and into a vial to be weighed to determine the yield.

2.1.2 Ex Situ Characterization

To characterize the precipitated Ir_8NiO_x Transmission Electron Microscopy (TEM) and Energy Dispersive X-ray Spectroscopy (EDS or EDX) was used (JEOL JEM-ARM200CF S/TEM). To prepare the sample a small amount of the catalyst powder was placed in a small centrifuge tube and isopropanol (IPA) (Fisher Scientific, LOT: 223457, ACS Plus) was added. It was then bath sonicated for a couple minutes to try and break up any agglomerates and get a few very small particles to disperse throughout the solution. Once dispersed, a pipette was used to take out a small portion of the solution and place 1-2 drops onto a copper grid. The grid was then placed in a watch glass

and left in an oven at 60 °C for two days to allow the IPA to fully evaporate. Then the sample was brought for testing. TEM uses an electron beam that is transmitted through the sample and scattered. Based on the thickness and material of the sample it will show up lighter or darker in the image. In addition elements can be identified with EDS due to the way that the elements interact with the electron beam. When the sample is excited by the electron beam it ejects a core shell electron which then is replaced by an outer shell electron. This reduction in electron energy level releases the energy as an X-ray which is different for each element allowing the approximate composition to be known.

2.2 Electrode Fabrication

2.2.1 Catalyst Ink Development

To bring the catalyst into an MEA it must first be deposited onto either a membrane or the PTL. In this case, it was deposited directly onto the membrane, as is common practice as well as for the potential for better performance as explained in section 1.2.3. This was done with inkjet printing (DMP-2800 Series, Dimatix) and therefore required a suitable ink. The method for making an ink can be complicated due to the requirements for viscosity, surface tension, and particle size to be in a certain range for the printing cartridges. The values from the manufacturer, Dimatix, are given in Table 2.1. There are two sets of values, one for a 10 pL cartridge and one for a 2.4 pL cartridge (Samba cartridges). When this project started the 10 pL was used, however since then the lab has transitioned to using Samba cartridges as the 10 pL cartridges are no longer available.

Table 2.1: Dimatix print nozzle ideal ink properties

Cartridge	Nozzle Size, d_n (um)	Viscosity, μ (mPa·s)	Surface Tension, γ (mN/m)	Ideal Particle/Aggregate Size (μm)	pH
DMC-11610, 10 pL	21.5	10-12	28-33	< 0.2	4-9
Samba, 2.4 pL	18.5	4-8	28-32	< 0.2	Neutral

Each ink that is made attempts to fit into each fluid property range, but even when not exactly in the range, an ink can still work as this is just the manufacturers suggestion for printing an ideal droplet. In a paper by Derby [92] inkjet printing in general is discussed along with what they found to be the ideal fluid properties for an ink. They characterize the fluid by the Ohnesorge number, which is the ratio of viscous to surface tension effects given by,

$$Oh = \frac{\sqrt{We}}{Re} = \frac{\mu}{\sqrt{\gamma\rho d_n}} \quad (2.1)$$

where We is the Weber number, Re is the Reynolds number, μ is the dynamic viscosity, γ is the surface tension, ρ is the density and d_n is the characteristic length of the nozzle from which the droplet is formed. When it was first introduced, a value Z , which was defined as the inverse of the Ohnesorge number,

$$Z = \frac{1}{Oh} \quad (2.2)$$

was used as the standard to compare to. They found that inks were printable within the range of $10 > Z > 1$ where values less than 1 were too viscous and values greater than 10 formed multiple droplets instead of one uniform droplet. Derby also noted that the Weber number needed to be greater than four to overcome the surface tension at the nozzle tip. These parameters will serve as the targets for properties of the inks. For this work, Samba cartridges are primarily used, which have a smaller ideal range for Z of 3.1-5.8.

The primary components of the ink are the catalyst followed by an additive to increase the viscosity, a solvent, and an ionomer. The anode catalysts used in this thesis are the Ir_8NiO_x previously mentioned and the state-of-the-art IrO_x catalyst which is made by Tanaka Kikinzoku Kogyo (TKK) (TKK, ELC-0110, SA = 100). The results section will compare these two anode catalysts. On the cathode side, platinum supported on carbon (TKK, 46.7 wt.% Pt metal) is used. The additive used is propylene glycol (PG) (Sigma-Aldrich) which is used to increase the viscosity of the ink. Solvents used in this work are IPA and DI water (Millipore, Direct-Q 5 UV Ultrapure DI water, 18 M Ω -cm). The solvent is used to disperse the catalyst particles. Finally, the ionomer used is Nafion (Ion Power Inc., Liquion LQ1105 1100EW 5%) which is used to

transport the protons through the catalyst layer and to the Nafion membrane when in an MEA.

The specifics of the ink recipes used can be found in Table 2.2. The viscosity and particle size results will be given in the results section 4.2 for Ir_8NiO_x and section 3.1 for IrO_x .

IrO_x TKK is the state-of-the-art catalyst which the Ir_8NiO_x will be compared to. The recipe used to make the IrO_x TKK ink for the samba cartridge was 2.4 mg of a 1:1 PG:IPA ratio, 117 mg of IrO_x and 780 mg of Nafion (5 wt.%).

Table 2.2: Ideal ink recipes for each nozzle and catalyst type

Catalyst	Cat. Amount, (mg)	PG, (mg)	IPA, (mg)	DI Water, (mg)	Nafion, (mg)	Nafion, (wt%)	Nozzle
IrO_x	117	2080	390	0	780	25	10 pL
IrO_x	117	1235	1235	0	780	25	Samba
Ir_8NiO_x	117	2100	0	900	780	25	Samba
Pt/C (46.7%)	37.5	1.6	1.5	0	321	30	10 pL / Samba

Ink Preparation Procedure

The procedure for making the inks, whose recipes were given in the previous section, is as follows. First, the catalyst mass was measured into a vial. In the case of IPA being used as the solvent, PG must be added first, since adding IPA directly to the catalyst powder may create a fire hazard. In the case of water being used as the solvent, it can be added directly and the PG is added after. The specified amount of both solvent and additive were added in the order described above. Then a magnetic stir bar was added and the ink magnetically stirred at 1100 rpm for 5 mins. The ink was then bath sonicated (Branson 1800) for 30 mins. Following that the ink was taken out of the bath and re-weighed and tared so the addition of the ionomer is accurately measured. Nafion was added to the ink dropwise using a pipette while the ink was in the sonication bath. The spacing between drops is five seconds to allow the ionomer to disperse. Once the desired mass was met, the ink is bath sonicated for 15 min. Following this, the ink was probe sonicated (Branson S-4000 Ultrasonicator) at 20 amplitude for 15 min, alternating for 2 mins ON

and 1 min OFF. Before probe sonication it was ensured that the magnetic stir bar was removed as this could damage both the stir bar and the sonication probe if left in. Also, during probe sonication the vial was placed in a water bath and parafilm was wrapped around the top to keep the ink temperature from increasing too much and decrease the liquid lost through evaporation, respectively, as the probe can become quite hot. After probe sonication the magnetic stir bar was returned to the ink and the ink was placed on a magnetic stir plate spinning at 300 rpm until it was ready to use. Ideally it is used within a day or two of making the ink to make sure that the ink is still stable.

2.2.2 Ink Characterization

Viscosity and Density Measurement

To begin characterizing the ink, the kinematic viscosity and density are measured. As noted above, the dynamic viscosity is required to help determine if the ink will jet (be pushed out of the nozzle) well during printing but it is also needed, alongside the density, because the dynamic viscosity is used for particle size measurements. The density is needed to convert the measured kinematic viscosity to dynamic viscosity using the relation

$$\mu = \nu\rho \tag{2.3}$$

where μ is the dynamic viscosity, ν is the kinematic viscosity and ρ is the density.

The density was simply measured using a 1 mL vial. The vial was placed in another container so it did not fall over and was put on the weigh scale and tared. Then ink was transferred into the vial up to the 1 mL line and weighed. The mass was recorded four separate times, removing the ink and adding it back each time, and the average was taken. Then the density was found as the average mass divided by the 1 mL volume, which is also equivalent to 1 cm³.

To measure the viscosity a Zeitfuchs cross-arm viscometer (Cannon Instruments) was used. The full apparatus is shown in Figure 2.1.

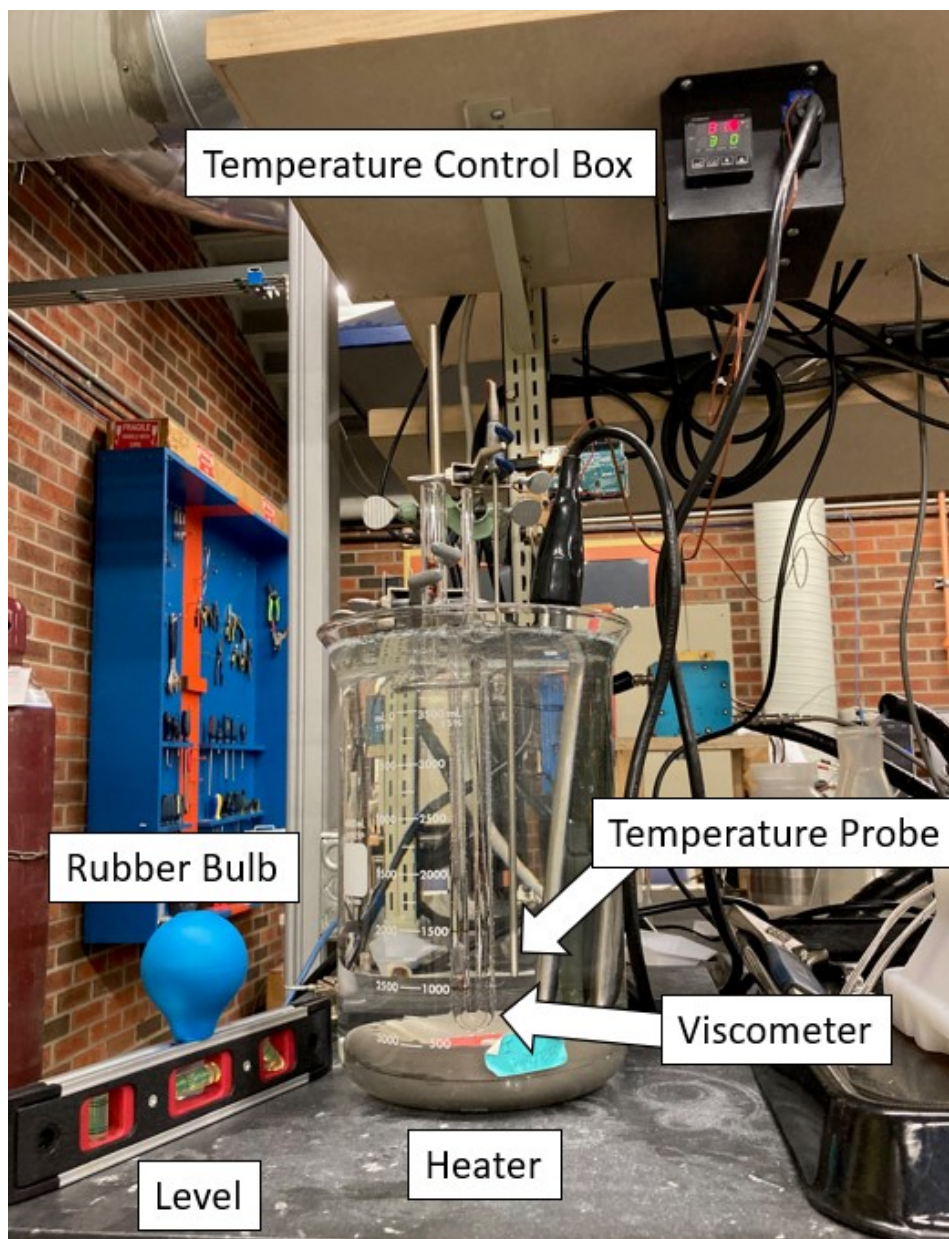


Figure 2.1: Setup for measuring the kinematic viscosity of an ink.

The process for using the viscometer is as follows. First, a 4 L beaker was filled with de-ionized (DI) water in which a heater (Electra Inc. MODEL 3150SS) was submerged. Using a stand with clamps, a temperature probe was placed in the water such that the tip is close to where the viscosity measurement takes place near the bottom of the viscometer. The temperature was set to 32 °C and time was allowed for the water temperature to stabilize, which can take up to a couple of hours. This temperature was chosen since it is

the starting temperature that the nozzles are set to when printing. Next, the viscometer was lowered into the water such that the area where the ink sits is submerged. A level was used to ensure that the viscometer is as vertical as possible since we want to maintain the same effect of gravity between measurements. The ink was added using a syringe to the cross-arm of the viscometer where it stayed for 15 min to allow the temperature of the ink to also rise to 32 °C. This area is shown in Figure 2.2.

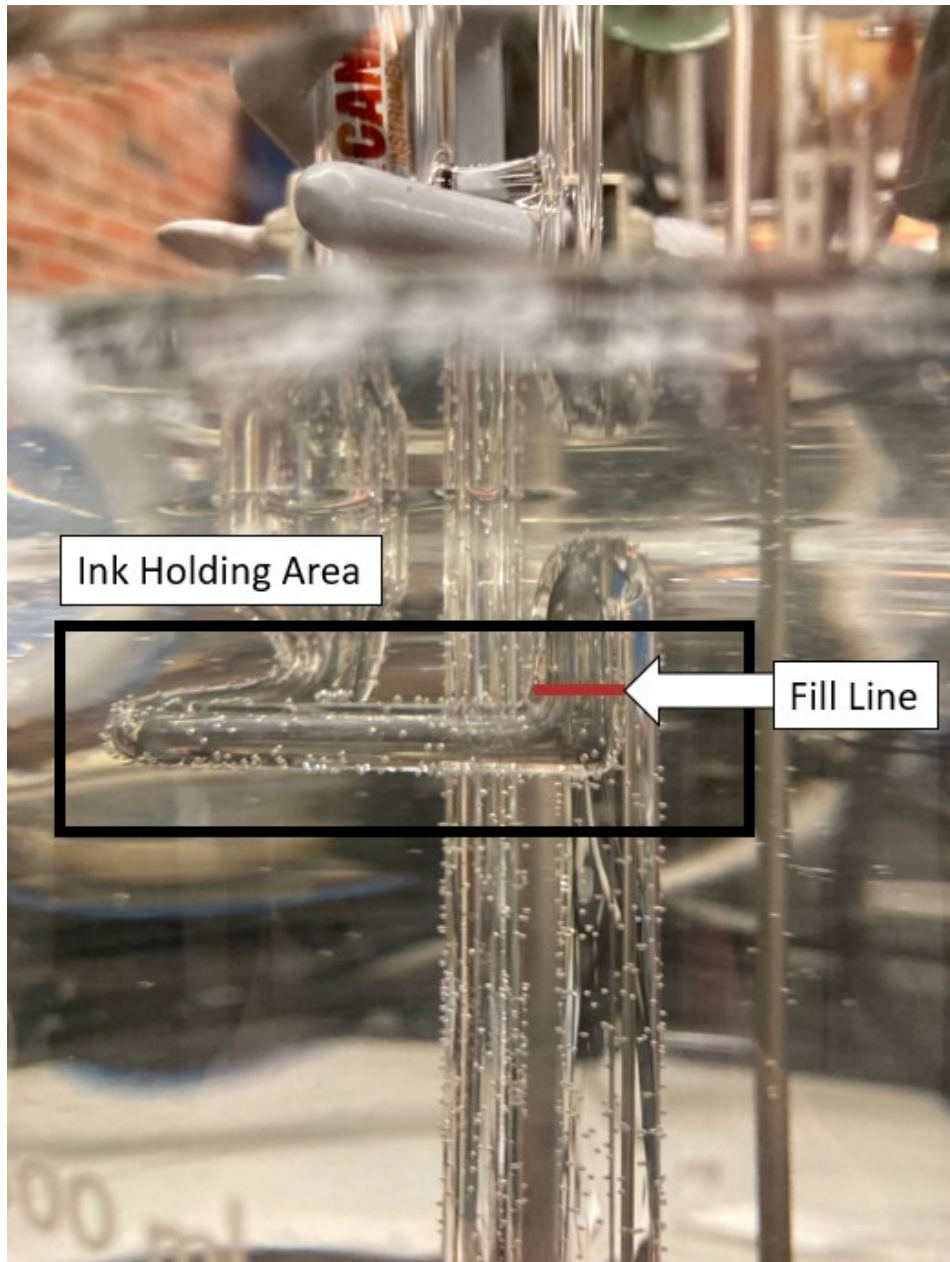


Figure 2.2: Area where the ink is inserted and left to heat to 32 °C.

A small piece of parafilm was used to cover the openings at the top to limit evaporation of the ink. After the 15 minutes a rubber bulb was used to apply pressure to push the ink over the hump in the cross-arm and into the capillary. Once the ink has flowed a few centimeters down the capillary, the bulb was taken off as the ink will stay in motion due to gravity. There is a line at the bottom of the measurement area. Once the ink reaches the line a stopwatch was started and once the ink crosses the line above the measurement area the stopwatch was stopped and the time recorded (See Figure 2.3). The test was repeated until the difference in the values was less than 2% and then the measured times were converted to seconds and averaged (t_{avg}).

The kinematic viscosity was found by multiplying the average time by a calibration constant. The manufacturer provided a certificate of calibration shown in Appendix A.2 with the calibration constant $C = 0.009463 \frac{mm^2}{s^2}$. Since this constant is dependant on the acceleration due to gravity it is corrected for the specific value at the location the viscometer is used. At the University of Alberta the gravitational constant is $9.812 \text{ m}^2/\text{s}$ [93]. Using the correction equation given on the certificate the corrected calibration constant is,

$$C_{cor} = \frac{9.812}{9.801} \cdot 0.009463 \frac{mm^2}{s^2} = 0.009474 \frac{mm^2}{s^2}. \quad (2.4)$$

So the kinematic viscosity is found as,

$$\nu = t_{avg} \cdot 0.009474 \frac{mm^2}{s^2}. \quad (2.5)$$

Multiplying by the density gives the dynamic viscosity.

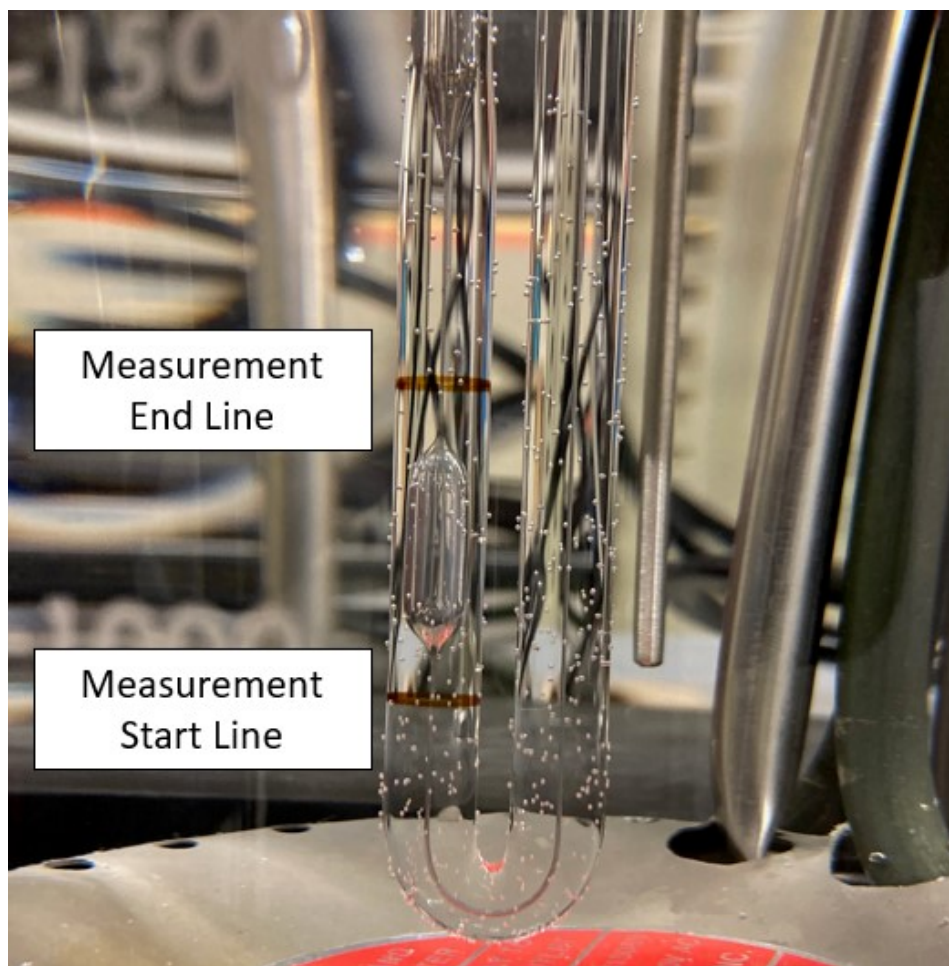


Figure 2.3: Measurement area of the viscometer showing the lines where the timer was started and stopped.

Particle Size Measurements

The catalyst inks used in this work are colloidal suspensions which to be printed well require a particle size on the order of 200 nm. To determine particle size the Litesizer 500 (Anton Paar) was used along with the Kalliope Software (Version 2.28.0) to run dynamic light scattering (DLS).

The following DLS theory along with how the Litesizer and Kalliope obtain and analyse the data is a summary from the Anton Paar Litesizer reference guide and white papers [94–96]. For a more in depth mathematical description of the algorithms and analysis tools used by the software see reference [96].

Particles at this size are subjected to movement caused by the random collisions with other particles known as Brownian motion. The diffusion of

a particle through Brownian motion is determined by the temperature of the solution, viscosity and the hydrodynamic diameter of the particle, assuming a perfect sphere.

The DLS technique shines a 658 nm laser at the colloidal solution where the light is then scattered by the particles in solution. In this work a backscatter angle of 175° was used since it is good at measuring turbid samples. The fluctuations of this scattered light over time can be used to determine the particle size. Larger particles will move slower and have less fluctuation in scattered light whereas the smaller particles will cause more fluctuations to occur. At small time intervals these fluctuations in light intensity are put through a correlation function which decays rapidly for small particles and decays slower for large particles. The Kalliope software then uses a cumulant model to analyze the correlation function using either the ISO 22412 standard or a more advanced algorithm developed by Anton Paar. The advanced algorithm was used in this work. Analysis of the correlation function yields the polydispersity index as well as the diffusion coefficient for a given particle. The polydispersity index provides information on how many different particle sizes are present in a sample which is given as a percentage. A polydispersity value less than 10% is considered to be almost monodisperse. Using the diffusion coefficient the hydrodynamic diameter can be calculated by rearranging the Einstein-Stokes equation,

$$D = \frac{k_b T}{3\pi\mu D_h} \quad (2.6)$$

where D is the diffusion coefficient, k_b is Boltzmann's constant, T is temperature, μ is dynamic viscosity and D_h is the hydrodynamic diameter. The assumptions made by the algorithm are that the sample is monomodal (only one particle size present), particles have spherical shape, and the particles are well dispersed with little aggregation. As will be seen in future chapters these conditions are not met. However, Anton Paar also implements a non-negative least squares algorithm with Tikhonov regularization analysis which is able to better analyze samples with high polydispersity. In this work the "General"

analysis model was used to get a more accurate representation of the various particle sizes. For this work the particle sized obtained from the Litesizer will be used as an estimate for the average particle size to see if it is reasonable to assume that the ink will be jettable.

The procedure to run these experiments begun with cleaning a quartz cuvette by rinsing the inside and outside with IPA followed by acetone (Sigma-Aldrich, 270725, HPLC $\geq 99.9\%$). A fibre cloth (Texwipe, TX1109, Techni-cloth II), which was dampened with acetone, was used to clean the outside of the cuvette further. Dust or other particles on the walls of the cuvette could effect the measurement. Next, 1 mL of ink was added to the cuvette and placed in the DLS equipment. The inks viscosity will be given in the results section but the appropriate dynamic viscosity was used for each ink at 32°C.

The refractive index of solution and each metal was not found exactly. For simplicity, the solution refractive index of propylene glycol at 25°C, which is 1.43, was used as it makes up the majority of the inks [97]. In addition Scott Storbakken found that changing the refractive index between 1.3299 and 1.4290 resulted in a 33.8 nm difference in measured particle size. This error is acceptable since the particle size is considered as an estimate [98]. For the material, Pt metal was selected in the Kalliope software which contains the refractive index and other optical parameters. Storbakken also did a sensitivity analysis of the refractive and absorbance parameters and found that his results did not change. The metal refractive index for the Ir_3NiO_x and IrO_x catalysts the refractive index was changed to 1.3 as this is the measured value for IrO_x thin films [99] but the other optical properties did not effect the results. These DLS tests primarily serve as an estimate for the particle size to get a sense of whether it will clog the printer nozzles or not so the optical parameters of the metals and solution were considered to be sufficient. Tests were run at 32°C to match the viscosity test. Following the DLS test the average hydrodynamic diameter and polydispersity index were found utilizing the "advanced" cumulant model and the "general" analysis which was then used to help guess whether an ink would be print well.

2.2.3 Inkjet Printing

As described in the introduction, inkjet printing is a precise and material saving process which is why it will be used for this work.

Once an ink is ready to be tested it is prepared for the inkjet printer. This device (Dimatix materials inkjet printer DMP-2800 Series, Fujifilm) uses piezo-electrics to push ink through a small nozzle to create picolitre size drops which ideally create a uniform catalyst layer due to the precise placement of droplets as well as their small volume.

The process for inkjet printing starts by bath sonicating the ink for 30 min followed by 60 min of degassing. While this was being done to the ink, the substrate was prepared. Nafion 212 (Ion Power Inc., NR-212, LOT: R2J101045M) was used as the substrate and was prepared by first cutting a 2 inch by 2 inch square for each CCM to be printed. For example, when printing four CCMs a piece of length 8 inches and width 2 inches was used. The Nafion sheet is comprised of the Nafion set between two plastic layers, one thin and one thick. The thin layer is removed and the Nafion sheet is pressed against the back of a clean silicone mat which has holes cut out where the printing is to occur. Then an approximately 4 cm x 4 cm piece of aluminum foil (Alcan) was cut, labelled and weighed as this is the initial mass which will be used to determine the loading of the CCMs. The foil was also pressed onto the back of the silicone sheet then placed on the printer plate which was preheated to 60°C. Once placed in the desired position, the vacuum was activated which sucks the sheet onto the plate ensuring it does not move during printing. Now that the substrate was in its final position, the printer's Fiducial camera was used to determine the coordinates which will be printed over. This was done so that each catalyst area is 23 mm x 23 mm, i.e. a 5.29 cm² active area. This allows for a slight buffer room of catalyst area for when assembling the cell later to be 5 cm². The key ink jetting parameters are the applied voltage, waveform, temperature and cleaning cycles. These are shown in full in section A.3.1 of the Appendix. Briefly, the voltage is 40 V, the waveform is a multi-pulse arrangement where two initial pulses happen to prime the droplet before a third

stronger pulse fires the droplet out of the nozzle, the nozzle temperature is set to 32°C, and the cleaning cycles occur at the start of printing a layer as well as every 180 seconds after. The cleaning cycle consists of the printer jetting some ink into a cleaning pad to try to ensure that agglomerations are not clogging the nozzles.

Once settings and placement were finalized, the printing was started. After a few layers were printed the aluminum foil was removed and placed in an oven for 5 min at 80-90°C to remove excess solvent. Then the foil with catalyst was weighed to assess the current catalyst loading. If the loading was below the desired amount the aluminum foil was replaced back under the silicone sheet and more layers were printed until the desired loading was reached. For the Ir_8NiO_x CCMs, the goal was 1 mg/cm². For the IrO_x loading study the target loadings were 0.25, 0.5, 0.75 and 1 mg/cm². For the Pt/C the target loading was 0.1 mg/cm². A finished set of CCMs is shown in Figure 2.4.

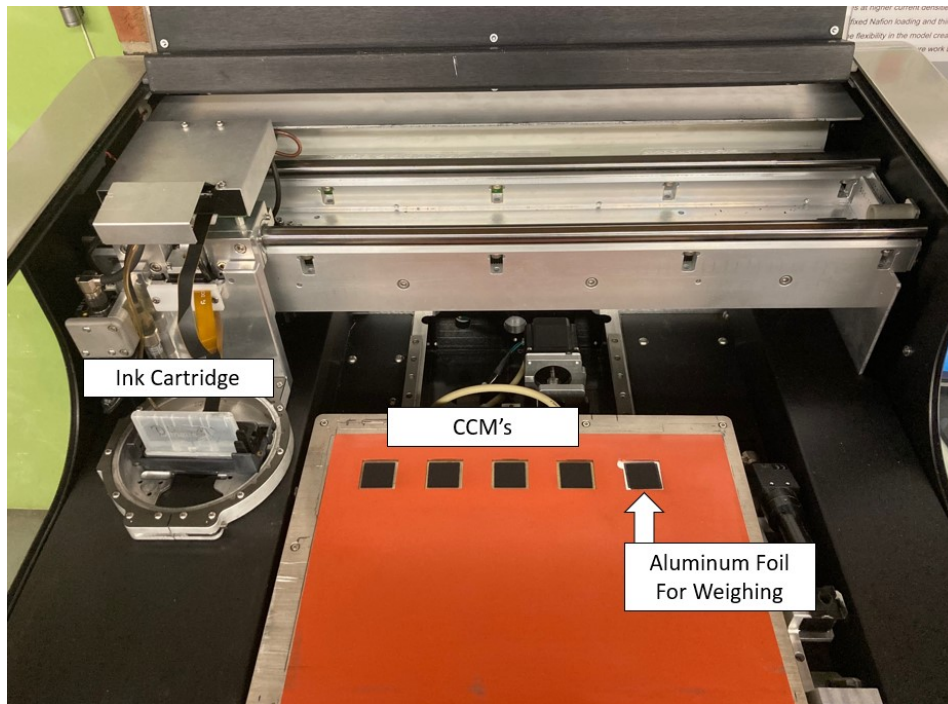


Figure 2.4: Inkjet printer with CCMs on vacuum plate.

Once the desired loading was reached the foil was left in an oven overnight (≈ 17 hours) at 80-90°C to allow any residual liquid to evaporate which will then give a more accurate loading when weighed the following day. The CCMs themselves were covered and left to dry in air.

For this work the anode side (Ir_8NiO_x or IrO_x) was printed first followed by the cathode side (Pt/C). After printing the anode side, microscope images were taken to see what the layer looks like on the surface at 20x and 80x magnification (See section 2.3.1). The primary feature that is observed is the formation of cracks during printing which could potentially effect connectivity of the layer. The formation of cracks will be discussed in the results chapters. Then the Nafion sheet was removed from the the thicker plastic backing, turned over and placed back on the backing with the side with no catalyst layer facing up. This is where the Pt/C was printed. Once both sides have been printed the CCMs are left to dry in air until used.

For this work four CCMs at 1 mg/cm² Ir_8NiO_x (E1, E2, E5, E6) and 16 IrO_x CCMs of various loadings (ML11-ML26) were made, which will be discussed in the results chapters.

For the Ir_8NiO_x layers, SEM images were taken before and after testing (E1-E2 and E5-E6) and for the IrO_x layers a specific batch (ML19-ML22) was made to look at the cross section and surface using SEM.

2.3 Ex Situ Characterization

2.3.1 Imaging

Optical Microscope

Images of the surface of the anode catalyst layers on the Nafion membrane were taken at both 20x and 80x magnification (Leica MC170 HD) to observe any surface characteristics, which were primarily crack formation during the ink drying process and indentations in the catalyst layer after testing in an MEA.

SEM

SEM (ZEISS EVO 10 SEM) imaging was performed by Jiafei Liu on Ir_8NiO_x and IrO_x CCMs to look at the layer thickness, structure, and possible degradation after testing. In addition, EDX was performed on the Ir_8NiO_x CCMs to try to understand how Ni ions might dissolve, degrading the catalyst layer and moving into the Nafion membrane. Four 1 mg/cm^2 Ir_8NiO_x CCMs were sent to SEM/EDX, one without being put in a cell and three tested. Getting a before and after look at the layer will give an idea of how the layer changes in terms of the structure and elemental composition due to testing. Four IrO_x samples were sent for SEM with loadings of 0.241, 0.567, 0.808 and 0.993 mg/cm^2 .

The samples were prepared by first cutting a portion out of the center of the CCM. Liquid nitrogen was poured into a small dish. Using two tweezers the sample was held in the liquid nitrogen and, after five seconds of allowing it to become rigid, the sample was snapped in half. Each half of the sample was then placed on an SEM stub with the cross section facing the outside for imaging as well as the anode catalyst layer facing upwards for surface images. Before the sample was imaged a solution containing carbon is applied to the inner edge of the sample to ensure there is adequate contact (electrical connection) between the sample and the rest of the SEM stub. Once images were received they were analyzed using ImageJ software.

The SEM images of the catalyst layer cross-sections can be used to find the thickness and porosity. Thickness can simply be measured on the image itself as the scale is known. Based on the measured thickness, the catalyst layer composition and assuming the density of each component, the porosity can be estimated. This can be done by first calculating the total volume, V_T ,

$$V_T = A_{CL}t_{CL} \quad (2.7)$$

where A_{CL} is the geometric catalyst layer area of 5.29 cm^2 and t_{CL} is the catalyst layer thickness. Next the theoretical volume, V_{th} , of the catalyst layer can be calculated using the equation,

$$V_{th} = V_{cat} + V_N = \frac{m_{cat}}{\rho_{cat}} + \frac{m_N}{\rho_N} = \frac{A_{CL}L_{cat}}{\rho_{cat}} + \frac{A_{CL}L_{cat}W_N}{(1 - W_N)\rho_N} \quad (2.8)$$

where L_{cat} is the catalyst loading in mg/cm^2 , ρ_{cat} is the density of the catalyst given as $11.7 \text{ g}/\text{cm}^3$ for both Ir_8NiO_x and IrO_x (This is taken from the density of IrO_2 since TKK did not report the density of their catalyst and the density of Ir_8NiO_x was not measured), ρ_N is the density of dry Nafion given as $2 \text{ g}/\text{cm}^3$, and W_n is the solid mass fraction of Nafion. Then the void space, V_{void} , is given by

$$V_{void} = V_T - V_{th} \quad (2.9)$$

and the porosity percentage can be calculated as,

$$\phi = \frac{V_{void}}{V_T} \times 100\% \quad (2.10)$$

where ϕ is the porosity percentage.

2.3.2 Through-plane Conductivity

The electrical conductivity of the catalyst layer contributes to cell resistance as it may promote or deter electron transfer if it is high or low, respectively. In Section 1.3.1 it was found in literature that the IrO_x TKK catalyst has low electronic conductivity and could benefit from decreased loading. To validate the electrical conductivity of the IrO_x catalyst layers previously found in literature, a setup was needed to measure the through-plane electronic conductivity and do so under compression to simulate the conditions inside an MEA.

To measure the conductivity of each catalyst layer, four loadings of approximately 0.25 , 0.50 , 0.75 and $1 \text{ mg}/\text{cm}^2$ were inkjet printed onto gold coated copper plates with a catalyst layer area of about 5.29 cm^2 . An example of the coated gold plate is shown in Figure 2.5. Then once the layer was dry, a copper block, also covered in a layer of gold with a contact area of 4 cm^2 , was placed centered on top of the catalyst layer.

A potentiostat (VersaSTAT4, Princeton Applied Research, Ametek) was connected to the block and gold plate using a 2-probe method shown in Figure

2.6. At each loading chronoamperometry was done at 50 mV until the current stabilized. Then an LSV was run from 0-0.1 V at 0.01 V/s. The resistance can be found from the slope of the LSV graph using Ohms Law ($V=IR$). Then the through-plane conductivity can be found using the following equation,

$$\sigma = \frac{t}{R \cdot A} \quad (2.11)$$

where σ is the conductivity, t is the layer thickness (estimated using SEM images of different loadings), R is the layer resistance, and A is the area of the block in contact with the layer which is 4 cm².

The sequence of chronoamperometry and LSV was repeated at pressures of 5, 10, 15, 20, 40, 60, 80, and 95 psig to study the effect of compression on the resistance and conductivity of the catalyst layer. Compression was applied using a pressurized line from a pressurized nitrogen tank. The pressure was measured using a flow meter (Cole-Parmer, 00307OX) and a valve to maintain the pressure.

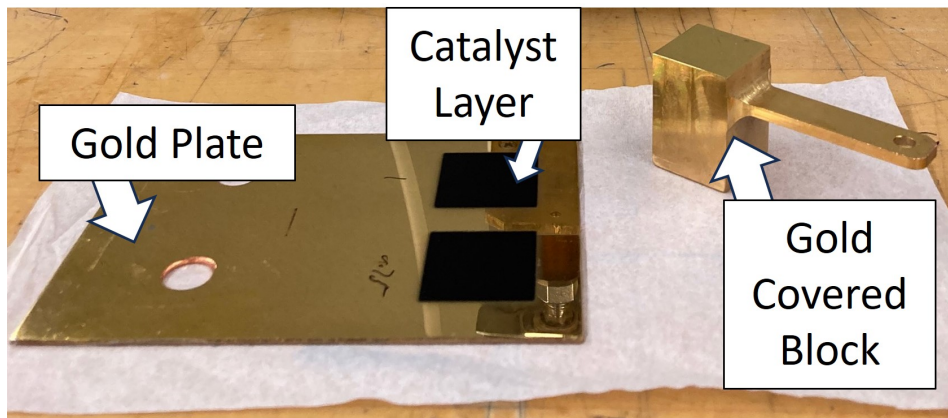


Figure 2.5: Example of the catalyst layers coated on the gold plate along with the gold plated block used to transfer the force and electrical signal to the catalyst layer.

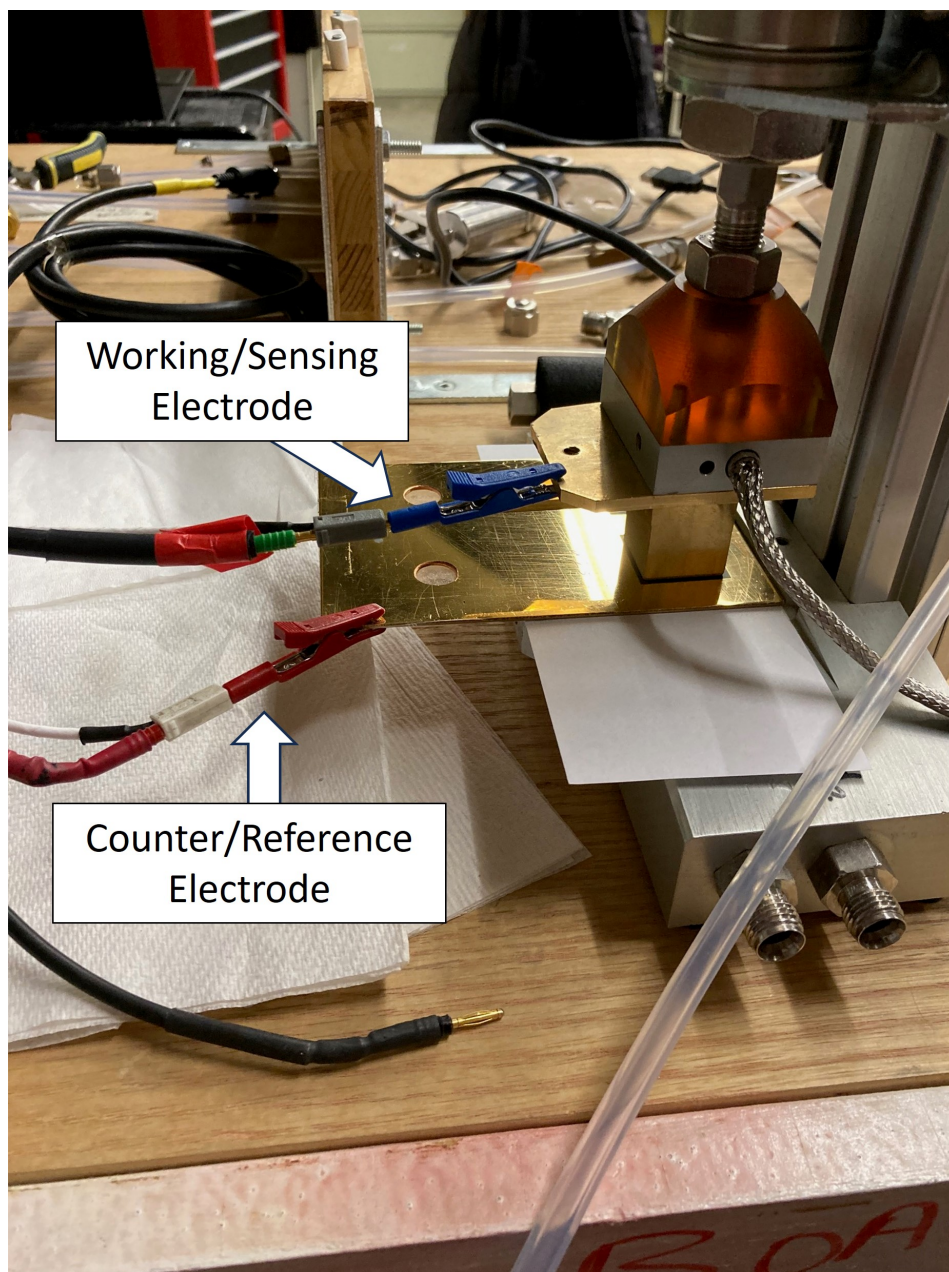


Figure 2.6: Setup for catalyst layer through-plane electrical conductivity tests under compression using 2-probe method.

2.3.3 Profilometry

In the process of compressing the catalyst layers to look at how conductivity changes, the catalyst layer may deform and change its thickness which is relevant to equation 2.11. To investigate the thickness after compression an Alpha-Step IQ (KLA-Tencor) profilometer was used at the University of Alberta nanoFAB. The Alpha Step uses a stylus which was dragged over the surface of the desired material in a straight line which senses the displacement of the stylus relative to a defined datum, which in this case is the gold plate, measuring the step height. The purpose was to look at the step height change from the gold plate to the catalyst layer which was left uncompressed possibly providing validation for the thickness obtained from SEM imaging and then the portion at the center that was compressed. Two line scans of 3 mm length were conducted for each of the four IrO_x loadings, 0.964, 0.723, 0.468 and 0.241 mg/cm^2 . The first step height measured was then taken as the uncompressed height.

2.4 Electrochemical Testing

2.4.1 Cell Assembly

The final step in preparing a cell for testing is assembling the CCM into the Scribner electrolysis cell fixture. It is built by combining the components given in Table 2.3, which also shows some thicknesses which are important for determining the pinch value. This "pinch" is part of what determines the compression and contact that the plates impart onto the CCM. The standard pinch value used in this work is 67 μm . More on the pinch value can be found in section A.4 of the Appendix.

Table 2.3: Cell components and corresponding thickness

Component	Material	Thickness (μm)
PTL	Platinized Titanium	274
MPL/GDL	Sigracet 28BC	240
Catalyst Layer	Various	4
Lamination Sheet	Plastic	75
Gasket	PTFE-Coated Fibreglass Fabric	152.4
Membrane	N212	50
Anode Bipolar Plate	Platinized Titanium	9500
Cathode Bipolar Plate	Graphite	12900
Current Collectors	Gold Plate	1400

The first step was cutting out a piece of lamination plastic which is the same size as the bipolar plate area. Then a 5 cm^2 square was cut out of the centre of the lamination sheet. The CCM to be tested was then placed in the lamination sheet such that the catalyst area completely encompasses the 5 cm^2 opening. Then the sheet was put into a folded piece of paper, to protect the catalyst layer, and sent through a lamination device (GBC Fusion 1100L) to give a rigid CCM. Next, two 152.4 um PTFE-coated fiberglass fabric sheet gaskets (McMaster-Carr, 8577K83) were cut out to cover the bipolar plate area, again with a 5 cm^2 hole in the middle. Holes are punched out of the gaskets and laminated CCM in the location with alignment pegs which hold all the cell components together until the cell is screwed together. Next the platinized titanium PTL (Bekaert Fibre Technologies) and MPL/GDL (sgl carbon, Sigracet 28BC) are cut out to 5 cm^2 squares using scissors and a knife, respectively. The first gasket was placed down on the graphite bipolar plate followed by the MPL/GDL with the darker side, the MPL, facing up towards where the CCM will be. Next the CCM is placed on top with the cathode side in contact with the MPL/GDL. The PTL is placed on top of the anode catalyst area followed by the second gasket.

Before sealing the cell, pressure paper (Fujifilm, LLLW PS, LOT: 0982191804) was placed over the PTL and the cell was sealed. The pressure paper is used to ensure that there is appropriate compression. The bipolar plate screws were turned in a star pattern to compress evenly up to a torque of 50 in-lbs. The

cell is then opened and if there is good compression levels, i.e. defined flow channels, then the pressure paper is removed and the cell is resealed and ready for testing.

2.4.2 Experimental Setup

This section shows the test stations and apparatus used to test an MEA. In the following sections the various methods for preparing and testing the cell are explained. The order of tests that will be conducted are as follows:

1. Conditioning, CV
2. Polarization Curves, LSV, EIS, CV

The actual electrolyzer test station and a schematic are shown in Figures 2.7. The setup when on the fuel cell test station is shown in Figure 2.8 for reference.

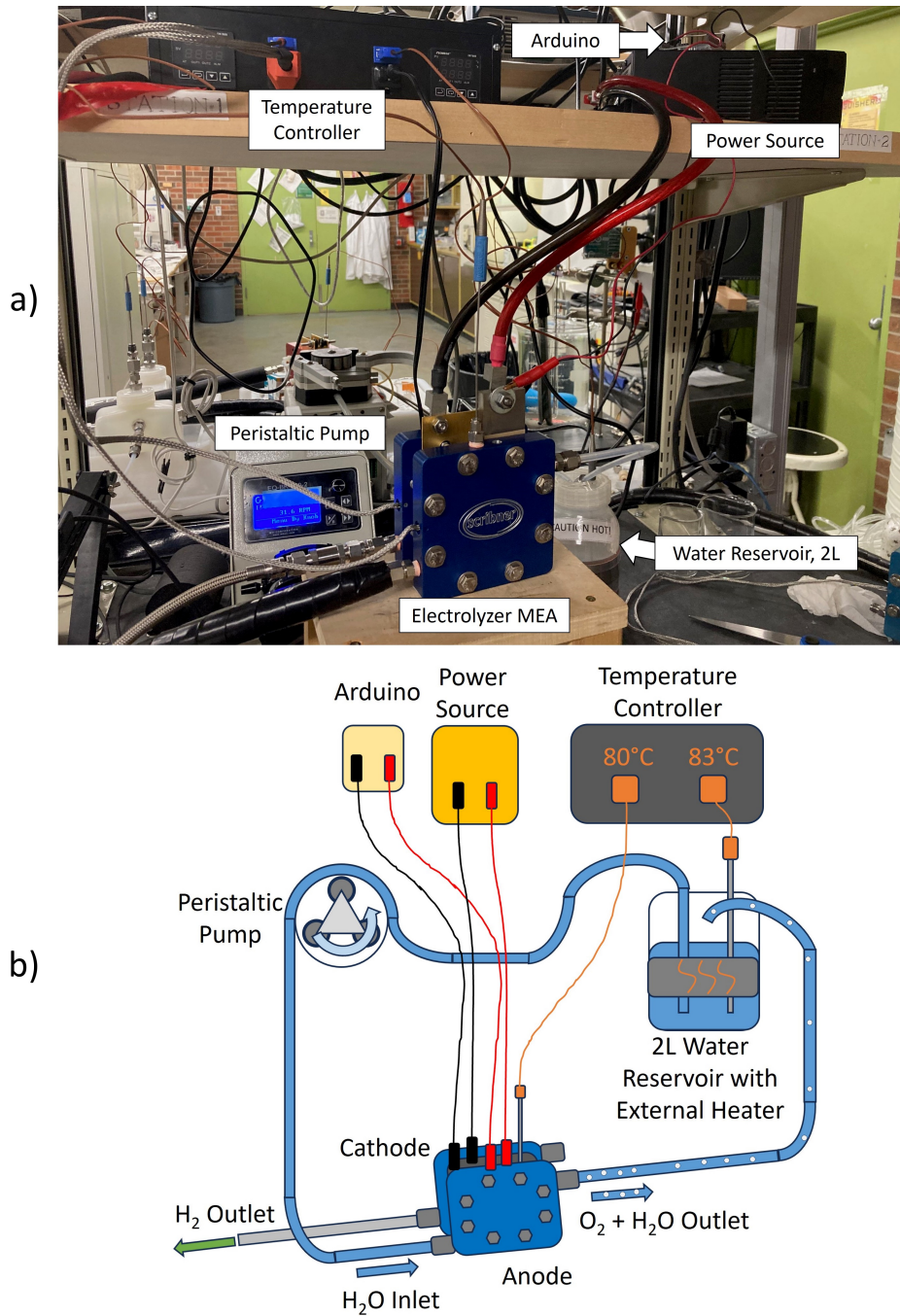


Figure 2.7: a) Electrolyzer setup, b) Schematic of Electrolyzer setup.

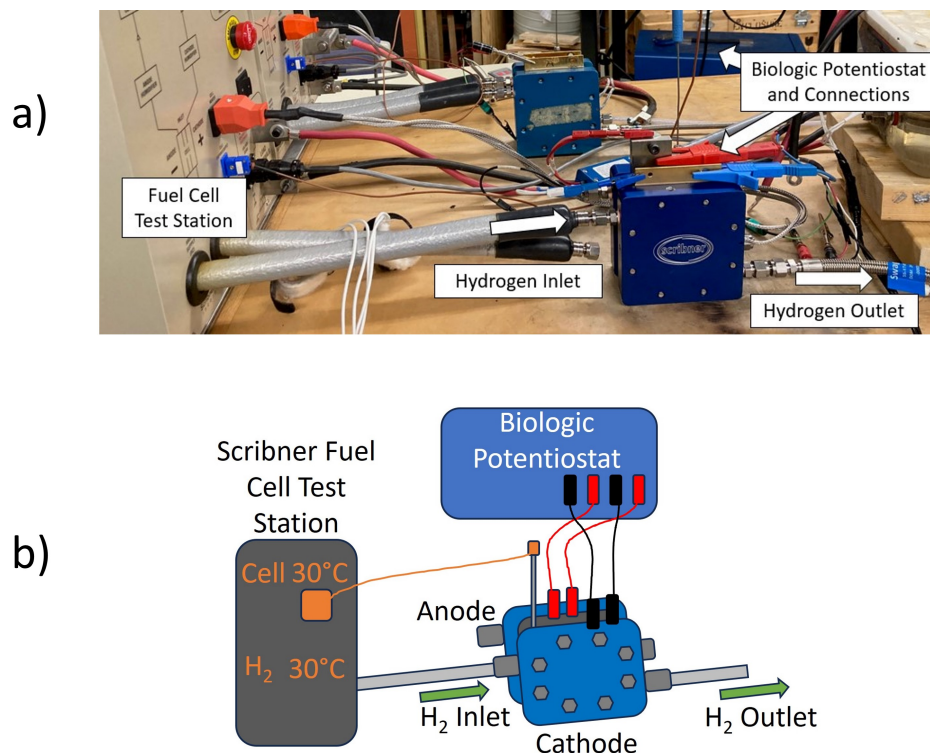


Figure 2.8: Electrolyzer cell connected to the fuel cell test station for when doing CV tests. a) Actual setup, b) Schematic.

2.4.3 Conditioning

Conditioning is the first method used after a new cell has been assembled. It is used to remove impurities from the catalyst layer and also allow for a more stable performance to be measured when doing polarization curves. The procedure for conditioning is as follows:

1. The 2 L externally heated water reservoir in Figure 2.7 was filled with DI water (Millipore, Direct-Q 5 UV Ultrapure DI water, 18 M Ω -cm) up to a few inches above the heaters so that the water level does not go below the heaters over the course of the conditioning.
2. The water reservoir was then heated to 83°C since there is a couple of degrees lost when transporting the water from the tank to the cell.
3. Hydrogen outlet and water lines were attached to the cell. Cell current collectors were connected to the power source (BK Precision 1688B)

which controls the power to the cell and the arduino board which is used to independently measure the current collector voltage.

4. A peristaltic pump (MTI Corp., EQ-BK-380-2) was used to control the flow of water to the cell. The flowrate speed was set to 31.6 rpm to achieve a final flowrate ranging from 29-30 mL/min. This flowrate was estimated by pumping into a beaker and timing how long it takes to fill up to 50 mL. This was repeated four times to ensure that the flowrate was within 29-30 mL/min.
5. The cell was heated to 80°C using the temperature controller.
6. The power source was turned on and an in-house program was used to set the desired current step and duration to be applied.
7. The cell is conditioned as per Table 2.4 for IrO_x cells and the first Ir₈NiO_x cell and Table 2.5 for subsequent Ir₈NiO_x cells. As will be discussed in the results section the Ir₈NiO_x did not perform as well under high current densities, so the conditioning current was lowered as to not completely degrade the cell before testing.

Table 2.4: Applied current and time for conditioning IrO_x cells and first Ir₈NiO_x cell (E1)

Time (s)	Current (A)
600	0
900	0.1
900	0.5
1200	1
1200	5
1200	10

Table 2.5: Applied current and time for conditioning subsequent Ir_8NiO_x cells (E5, E6)

Time (s)	Current (A)
600	0
900	0.1
900	0.5
1200	1
1200	4

2.4.4 Cyclic Voltammetry

Cyclic voltammetry is a method typically used to see oxidation and reduction processes. In this case it will be used to investigate the oxidation peaks of Ir which will allow the measurement of the ECSA. CV's were run after conditioning and polarization curves to see how each process effects the ECSA. CV was run using the Biologic SP-300 potentiostat and the Scribner fuel cell test station (850e Multi Range) following the steps below:

1. Once the cell was at room temperature after running conditioning or pol. curves/LSV/EIS the anode side was filled with DI water by running the pump.
2. Then all inlet and outlet tubing was disconnected from the cell and on the anode side they were capped to hold the water in the cell.
3. Then the cell was brought over to the fuel cell test station. The hydrogen lines were connected to the cathode side of the cell while keeping the cell anode side closed.
4. The fuel cell test station and corresponding program were started. The temperature was set to 30 °C for both the cell and hydrogen while the flowrate was set to 0.2 L/min for hydrogen and 0 L/min for nitrogen.
5. The potentiostat was connected to the cell. Using the EC-Lab program, a cyclic voltammogram was run from 0.005 to 1.5 V at a scan rate of 40 mV/s for 11 cycles with the last cycle being the one analyzed in the results.

6. Once done the fuel cell test station was turned off and the cell was returned to the electrolyzer test station.

The method used to calculate the ECSA was proposed by Tan et. al. [37]. The first step is to find the total anodic charge by integrating from 0.4-1.25 V while correcting for the double layer charging estimated at 0.2 V. For example see Figure 3.9 a) for cell ML14. Then use the following equation to estimate the ECSA,

$$ECSA = \frac{A_I}{A_{geo}SqL} \quad (2.12)$$

where A_I is the integrated area for anodic charge between 0.4-1.25 V, A_{geo} is the geometric area of the catalyst layer, S is the voltage scan rate, q is the deprotonation charge constant approximated by Tan to be $440 \pm 14 \mu\text{C}/\text{cm}^2_{ECSA}$, and L is the catalyst loading.

2.4.5 Polarization Curves

Polarization curves are found to observe the overall performance of the cell. The procedure is given below:

1. After doing the first CV the electrolyzer test station was set up the same way as for the conditioning (Water reservoir at 83°C, cell at 80°C and the flowrate at 29-30 mL/min (31.6 rpm)).
2. Polarization curves were obtained using the power supply by first allowing the cell to stabilize at 0 A for 10 minutes and then using the in-house code to apply current densities from 0.02 to 0.2 A/cm² in 0.02 A/cm² increments (0.1-1 A in 0.1 A increments) and from 0.2 to 4 A/cm² in 0.2 A/cm² increments (1-20 A in 1 A increments) and then reversed to go backwards at the same intervals. The cell was run for 2 minutes at each current density and the data was averaged over the last 10 seconds. Three forward and backward sweeps were run in total. Since it is a long continuous test if the water began to run low it was refilled between curves during the 10 min stabilization period at 0 A.

2.4.6 Kinetic parameters

After getting the polarization curve using the power supply, the kinetic parameters were measured using the Biologic potentiostat.

1. Maintaining the same cell conditions as it was with the polarization curve the cell was disconnected from the BK precision power source and connected to the Biologic potentiostat.
2. Using linear scan voltammetry, the potential was scanned from 1.3 to 1.75 V with a scan rate of 2 mV/s to give a high resolution to the kinetic region. If at any time the current would approach 10 A the test was stopped since this is the current limit of the potentiostat.

2.4.7 EIS

The EIS test can be performed immediately after obtaining the LSV.

1. Again, the cell was tested on the electrolyzer station set up and maintained at 80°C and the water flowrate is set to 29-30 ml/min for the duration of the tests.
2. Galvanostatic EIS measurements were performed at constant current densities of 0.02, 0.2, and 0.2 A/cm² with the amplitude of each wave being 30, 60 and 150 mA, respectively. The frequency range of the each test starts at 100 kHz and goes down to 20 mHz.

Resistance and capacitance values can be found by fitting the impedance spectra, i.e. the impedance vs frequency signal, using an equivalent circuit which for PEMWE is shown in Figure 2.10, where L_1 is an inductance which is due to effects from crossing of wires and how the electric and magnetic fields interfere with one another. R_1 is the HFR, while R_2 and R_3 are the charge transfer resistances for the first and second semicircle, respectively, and Q_2 and Q_3 are constant phase elements (CPE). The equivalent circuit was modelled such that the first semicircle ($Q_2 + R_2$) corresponds to the cathode and the second semicircle ($Q_3 + R_3$) corresponds to the anode [36]. An ideal

EIS curve containing capacitance forms a perfect semicircle from which double layer capacitance can be directly calculated, however it is typical for curves to be slightly depressed vertically due to the catalyst layers not being ideal capacitors which is accounted for by the CPE. The curve fitting software used in this work, EC-Lab, calculates a pseudo capacitance from the CPE value using the equation,

$$C_i = \frac{(R_i Q_i)^{\frac{1}{a_i}}}{R_i} \quad (2.13)$$

where i is the index for the first or second semicircle, C_i is the capacitance, R_i is the charge transfer resistance and a_i is a constant factor associated with the CPE fit. The psuedo capacitance can be related to the double layer for the associated anode or cathode. Then the double layer capacitance can be related to the surface area within the catalyst layer and compared to values obtained from CV.

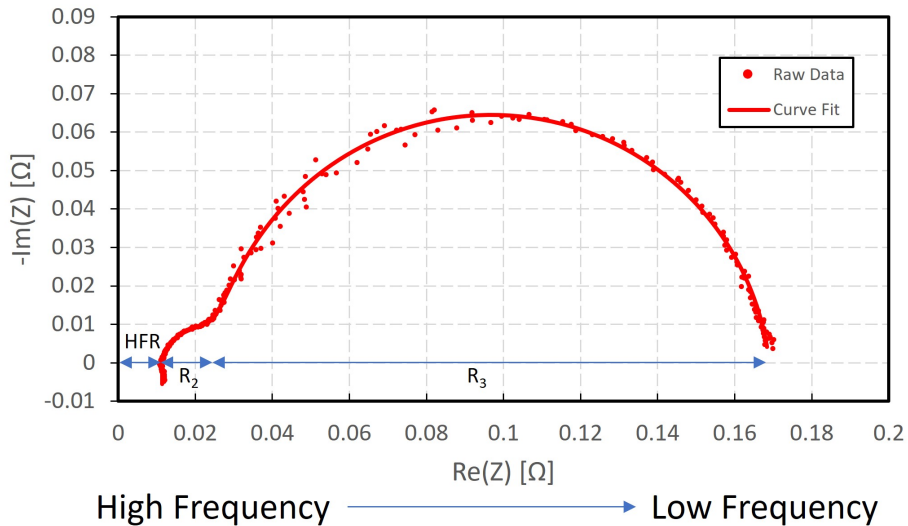


Figure 2.9: Example of a Nyquist plot with data fitted using an equivalent circuit. Tests go from high to low frequency as the curve goes from low to high resistance.

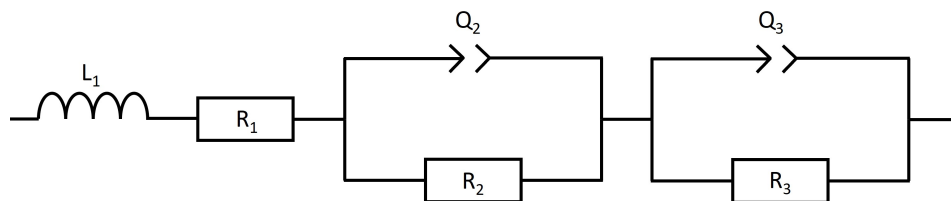


Figure 2.10: Equivalent circuit used to fit EIS data for PEMWE.

Chapter 3

Study of Reducing IrO_x Anode Catalyst Layer Loading for Improved Cell Performance

3.1 Ink Characterization and Printing

The IrO_x ink presented in section 2.2.1 was analyzed to measure the density, viscosity, and particle size. The IrO_x TKK Samba ink was found to have a density of 0.886 g/cm^3 , viscosity of $5.38 \text{ mPa}\cdot\text{s}$, surface tension of 24.95 mN/m (found for a 1:1 PG:IPA solution by Jasper Eitzen), which corresponds to a Z value of 3.76. The viscosity is in the correct range of $4\text{-}8 \text{ mPa}\cdot\text{s}$ while the surface tension is slightly below the desired range for the Samba cartridge of $28\text{-}32 \text{ mN/m}$. Even so, the Z value is between 1-10 so the ink should still be jettable assuming an appropriate particle size [92].

Figure 3.1 shows the particle size distribution obtained from DLS. The average hydrodynamic diameter is $194.17 \pm 14.24 \text{ nm}$ with a polydispersity of $20.3 \pm 5.1\%$ which is suitable for printing. The average hydrodynamic diameter is fairly constant over the course of the 10 runs but begins to increase just above 200 nm by the 10th run which could be a sign of agglomeration.

The cathode side was made using the standard Pt/C ink given in section 2.2.1. The Pt/C TKK Samba ink was found to have a density of 0.910 g/cm^3 , viscosity of $5.353 \text{ mPa}\cdot\text{s}$, surface tension of 24.95 mN/m (found for a 1:1 PG:IPA solution by Jasper Eitzen since the PG:IPA ratio is about 1:1), which corresponds to a Z value of 3.83. The average hydrodynamic particle

size is found from Figure 3.2 to be 291.90 ± 49.22 nm with a polydispersity of $24.45 \pm 2.24\%$. Although the average hydrodynamic diameter is higher than 200 nm the ink may still be printable as inks with an average diameter under 1000 nm have been printed and the properties for this ink are similar to that of the IrO_x ink above meaning that both should print well as they are within the majority of the guidelines for printable inks.

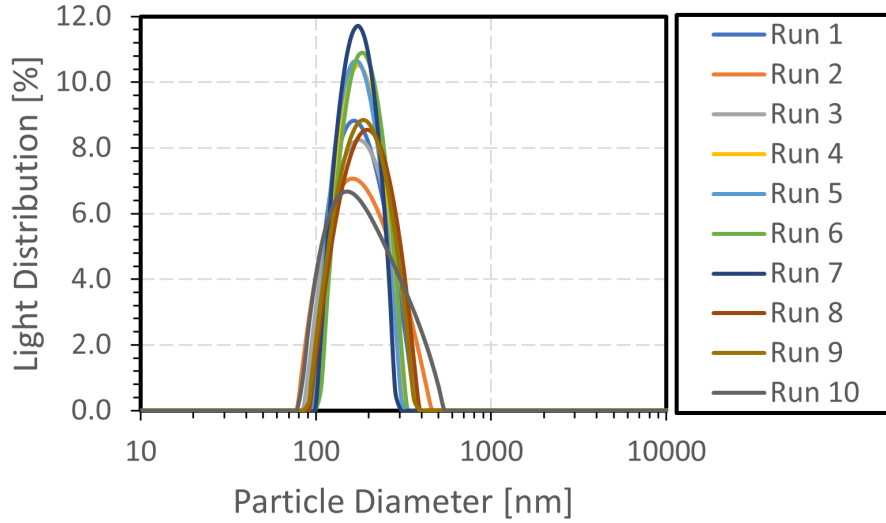


Figure 3.1: DLS light sensitivity distribution of the 1:1 PG:IPA IrO_x TTK ink made for the Samba cartridges.

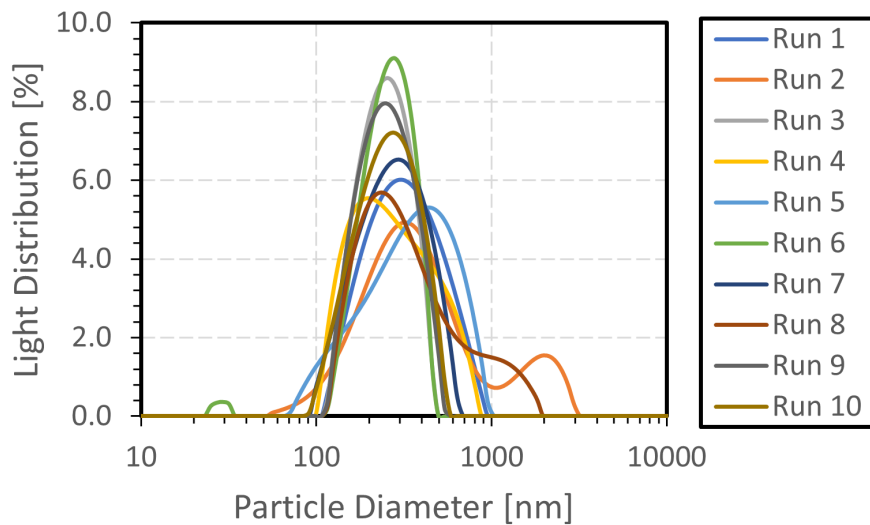


Figure 3.2: DLS light sensitivity distribution of the 46.7% Pt/C TTK ink.

Four IrO_x TTK catalyst layer loadings were printed, i.e., 1, 0.75, 0.5 and 0.25 mg/cm² where the loading was measured as discussed in section 2.2.3. Four batches were made with the cells being shown in Table 3.1. CCMs ML11-ML14, ML15-ML18, and ML23-ML26 were tested whereas ML19-ML22 were used for characterization of the catalyst layers given in Section 3.2. As can be seen in Table 3.1 the amount of layers it takes to form a layer of a specified IrO_x loading can vary by about 2-5 layers when using the Samba cartridges whereas Pt loading was printed more consistently after batch 1.

Table 3.2 shows the loading and layers required to make cells ML5, ML6, ML9 and ML10. These CCMs were fabricated utilizing an older generation of cartridges (Dimatix Mat. Cartridge 10 pL, DMC-11610). The 10 pL cartridge nozzles were heavily used prior to printing these cells, therefore prone to clogging, which resulted in 2-3 times as many layers needed to reach a similar loading to the cells made with the next generation Samba cartridge. However, ML5, ML6, ML9 and ML10 will be discussed only briefly in Section 3.3.5 to show some effects of varying the pinch value.

Table 3.1: CCMs printed for electrochemical and ex-situ testing using the Samba cartridges.

Batch	Cell	Anode IrO _x TTK Loading (mg/cm ²)	No. IrO _x Layers	Cathode Pt Loading (mg/cm ²)	No. Pt/C Layers)
1	ML11	1.078	20	0.111	18
	ML12	0.794	15	0.111	18
	ML13	0.510	9	0.111	18
	ML14	0.269	5	0.111	18
2	ML15	1.064	15	0.111	9
	ML16	0.723	9	0.111	9
	ML17	0.468	5	0.111	9
	ML18	0.284	3	0.111	9
3	ML19	0.993	14	0.117	10
	ML20	0.808	10	0.117	10
	ML21	0.567	7	0.117	10
	ML22	0.241	3	0.117	10
4	ML23	1.007	22	0.146	9
	ML24	0.737	14	0.146	9
	ML25	0.510	9	0.146	9
	ML26	0.255	5	0.146	9

Table 3.2: CCMs printed for electrochemical testing with changes to compression using the 10 pL cartridges. *Made by Manas Mandal.

Cell	IrO _x TKK Loading (mg/cm ²)	No. IrO _x Layers	Pt Loading (mg/cm ²)	No. Pt/C Layers
ML5	0.255	10	0.105	30
ML6	0.99	49	0.105	30
ML9*	0.99	-	0.1242	-
ML10*	0.285	-	0.1242	-

3.2 Initial Ex Situ Characterization

3.2.1 Optical Microscopy

Figure 3.3 shows the images taken with the Leica optical microscope for the IrO_x TKK catalyst layer of each CCM with each batch in columns and loadings from 1 to 0.25 mg/cm² in rows from top to bottom. The main difference between the CCMs is that the amount of cracks increases with a decrease in loading which means the higher loadings have more uniform layers. It can also be noted that the grain size of the cracked areas decreases with a decrease in loading.

The difference in lighting is not a reflection of the uniformity and catalyst coverage. It is primarily due to the exposure time used to take the image, with higher exposure times leading to brighter images. The brightness and contrast was adjusted using ImageJ software to try and achieve a similar view of the layer for all CCMs.

Although there are differences in the amount of layers printed, all batches have a similar number and size of cracks. The only exception may be Batch 2 which appears to have more cracks in the 1 mg/cm² layer. Cracking in the catalyst layer has primarily been studied for fuel cells but can be related to electrolyzers as the only difference is the catalyst. The ink and deposition process remains the same. The primary causes of cracking are due to the drying process where evaporation of solvents happens faster at the surface than inside the layer causing a difference in stress from the shrinkage of the layer [100] and excessive bending of the membrane since the catalyst layer is more rigid than the membrane [101]. If more material is being deposited at once, i.e. less layers printed, then the difference in evaporation rate between

the top of the layer and bottom may be higher possibly leading to more cracks as seen with Batch 2.

The impacts of cracks on performance are a challenge to determine as it is difficult to control crack formation but it has been found in the case of fuel cells that it can be beneficial or harmful. Cracks could be positive in that they improve mass transport by providing pathways for gas to leave and water to go deeper into the layer [102, 103]. Cracks could have a negative effect if they cause islands to form in the catalyst layer, meaning that there is less connectivity particularly for electron transport which would lead to less area of the catalyst being utilized therefore lowering performance [101]. In addition cracks could have a negative effect on the durability of the catalyst layer which could decrease performance over time [104, 105].

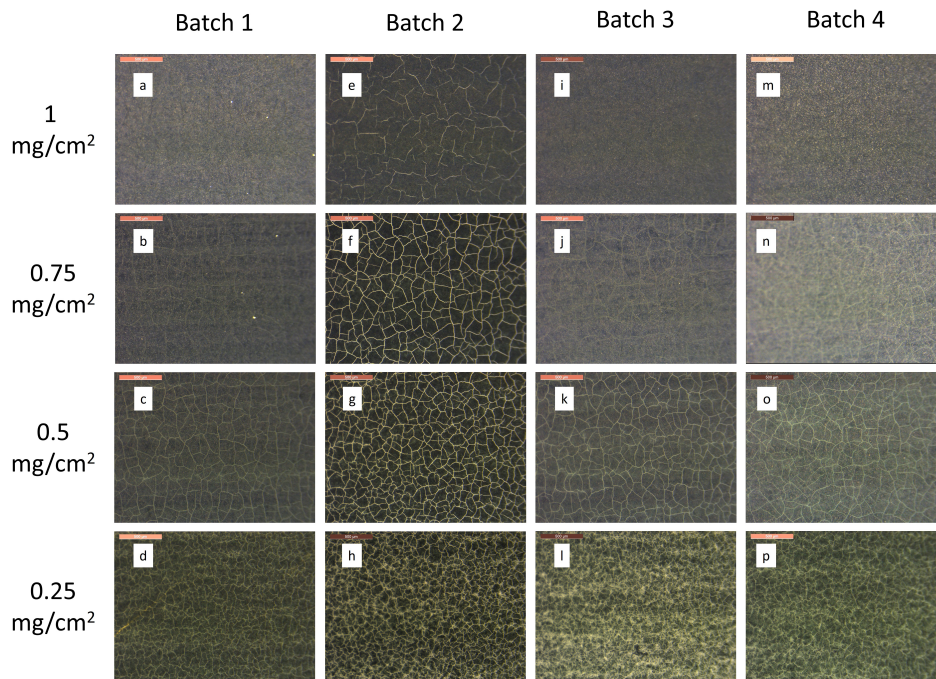


Figure 3.3: Optical microscope images at 20x magnification of the anode side of each CCM. a-p corresponds to ML11-ML26. Each column is a batch and each row is a different loading with 1 mg/cm^2 at the top and 0.25 mg/cm^2 at the bottom. Exposure and brightness was adjusted in each image to see cracks formed during printing.

3.2.2 Catalyst Layer Thickness and Porosity

Figure 3.4 shows cross section images each loading at 5000x magnification. Each layer was imaged in 3 locations and the catalyst layer thickness was measured 10 times for each image with the measurements approximately 2 μm apart. There were 30 measurements in total for each loading.

Figure 3.5 shows the average thickness for each loading. A linear trend between loading and layer thickness is observed which means the layer does not compact as more layers are printed on top of the original ones. Furthermore, based on the linear regression, every 0.1 mg/cm^2 results in an additional 0.5 μm of added thickness. An Alpha Step stylus profilometer was also used for validation of the layer thickness as shown in Figure 3.5 which follows a similar trend as the measurements from SEM. The Alpha Step measurements (see section 2.3.3) were made on catalyst layers printed on gold plates which could lead to some differences in thickness. Due to not being printed in the same way, the SEM measurements are used for the linear fit. Since, the loadings at 0.576 and 0.993 mg/cm^2 have a large standard deviation in layer thickness, t-test statistical analysis was applied to ensure that each loading truly has a different average thickness. The t-value and P-value were calculated and are given in Table 3.3 which shows that there is a statistical difference between the layers as the P-value is less than 0.05 rejecting the null hypothesis that the means of each set are the same. This was done against subsequent samples of data since if one is statistically different than the one closest to it then it will also be statistically different than the other sets of data. In addition, the t-value is greater than the standard t-value at a 95% confidence interval for a 2-tailed t-test with 58 degrees of freedom (30+30-2) which is about 2.00 again indicating a statistical difference.

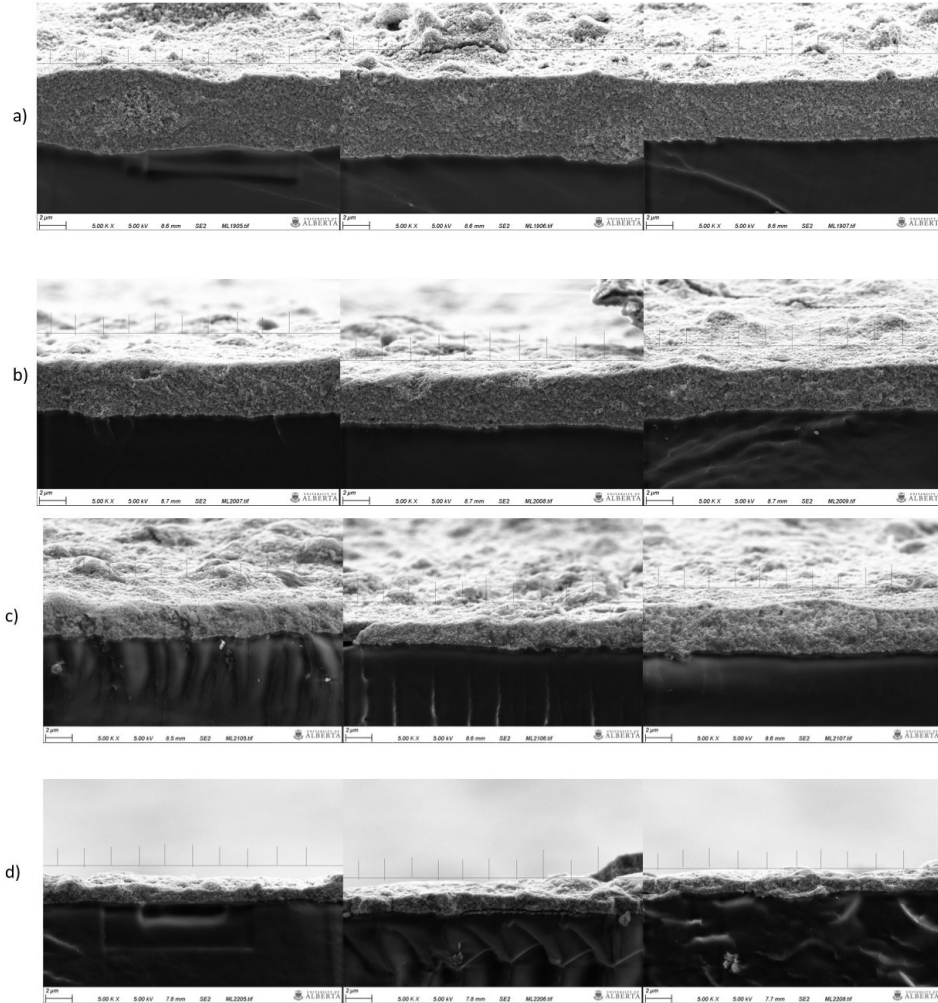


Figure 3.4: SEM images of 5000x magnification IrO_x Layers. a) ML19 0.993 mg/cm², b) ML20 0.808 mg/cm², c) ML21 0.567 mg/cm², d) ML22 0.241 mg/cm². The faint grey lines above the catalyst layer were the guidelines used to indicate where measurements were taken.

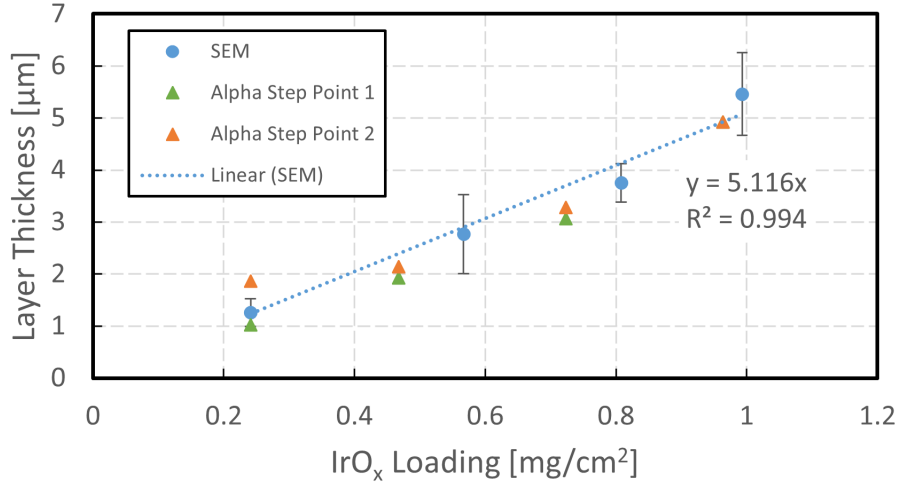


Figure 3.5: Catalyst layer thickness depending on the the IrO_x TKK loading using both SEM images and stylus profilometry. Error bars are the standard deviation.

Table 3.3: T-tests between samples for layer thickness

Cells Samples Compared	Loading's Compared (mg/cm ²)	t-value	P-value (95% CI)
ML19 vs ML20	0.993 vs 0.808	10.6	2.94*10 ⁻¹⁵
ML20 vs ML21	0.808 vs 0.567	6.4	3.00*10 ⁻⁸
ML21 vs ML22	0.567 vs 0.241	10.3	1.04*10 ⁻¹⁴

The porosity was calculated as shown in section 2.3.1 for the layers that SEM was performed on which are ML19-ML22. Then using the linear equation for thickness from Figure 3.5 the theoretical thickness of all the tested CCM catalyst layers was found and therefore their porosity.

Figure 3.6 displays the porosity as a function of catalyst loading which shows the porosity of the imaged samples ML19-ML22, which have 25 wt.% Nafion loading, initially decreasing from 51.8% to 45.7% from 0.24-0.81 mg/cm², respectively and then up to 54.1% at 0.99 mg/cm². So there is no distinct trend when it comes to the porosity of the measured samples ML19-ML22. However, if the linear trend is assumed for the tested cells then the porosity obtained from the calculated thicknesses is constant at 50.7%. These values differ from that found by Mandal [106] who obtained a porosity of 22% for a 25wt.% Nafion IrO_x catalyst layer. The difference could be due to the different ink

recipe and print nozzles used. Mandal used 10 pL whereas the Samba cartridge was used in this work. This also makes sense given that he also saw a catalyst layer thickness of $3.3 \mu\text{m}$ for a 1.035 mg/cm^2 layer.

Figure 3.7 shows a 20000x magnification image of the four IrO_x catalyst layers to view the internal structure which can be seen to be uniform, porous and visually similar between all loadings. Since the structures are not visibly different in these images it shows that the porosity is likely also similar but may have some variation depending on where the catalyst layer thickness is measured.

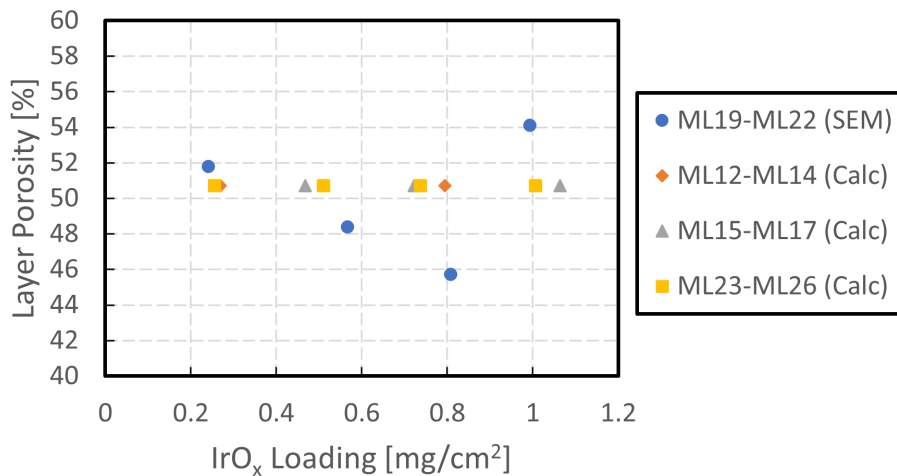


Figure 3.6: Calculated porosity of SEM imaged and tested catalyst layers. Measured thickness was used for ML19-ML22 and calculated theoretical thickness was used for the remaining cells.

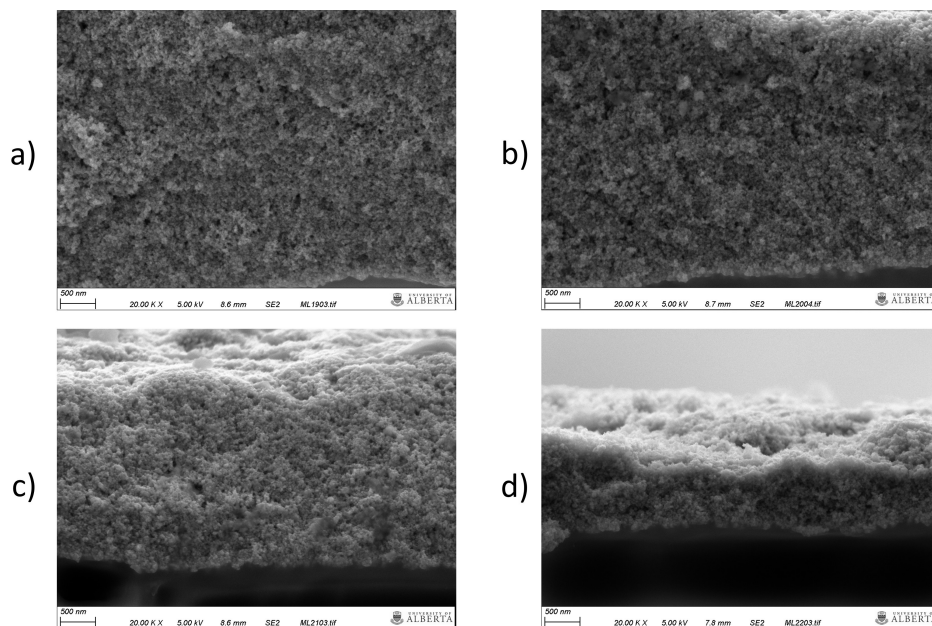


Figure 3.7: SEM images of ML19-ML22 (a-d) at 20000x magnification showing the internal structure of the IrO_x catalyst layer.

3.2.3 Uniformity and Adhesion

As seen in Figure 3.5, for some of the catalyst layers there is a large standard deviation which shows that the variation of thickness of the layer can be up to $\pm 1.5 \mu\text{m}$. Ideally the inkjet printing would result in perfectly uniform layers but due to inconsistencies with nozzles, droplet size, and catalyst particle size throughout the course of printing multiple layers there is some deviation from a flat surface. The change in thickness of up to $1.5 \mu\text{m}$ is significant due to the fact that it could make up a large percentage of the catalyst layer thickness since the average of the layers measured are only $1.26\text{-}5.46 \mu\text{m}$ thick.

Figure 3.8 shows SEM images for ML19 at 1000x, 500x, 200x and 100x magnification which show that on a larger scale the layer contains small bumps which are the likely cause of the standard deviation previously discussed. This is similar for all CCMs imaged. Bumps and cracks could be formed by the clogging of nozzles during printing which result in inconsistencies. Since the small bumps appear to be present at random and not in uniform lines or forming ridges, it is more likely that this is due to how the catalyst layers dries on the membrane surface or satellite droplets when the droplet is jetted

from the nozzle. If it were purely nozzles clogging then there would be defined lines of ridges and valleys where catalyst ink was not printed. But beyond the small μm sized bumps the layer is quite uniform in terms of thickness however there are still cracks that cause discontinuities in the layer as seen previously in Figure 3.3. Images of the other samples ML20-ML22 are given in the Appendix (Figures C.1-C.3).

Adhesion of the catalyst layer to the Nafion membrane below appears to be good as there is only slight separation in small sections such as the circled section on Figure 3.8 a). Other than this location there is good contact between the catalyst layer and the membrane. This is similar for all CCMs imaged. Adhesion between the catalyst layer and membrane is important to maintain as this allows the efficient transfer of H^+ . Areas with poor adhesion will result in an increased cell resistance as there is less area to move H^+ ions to the membrane.

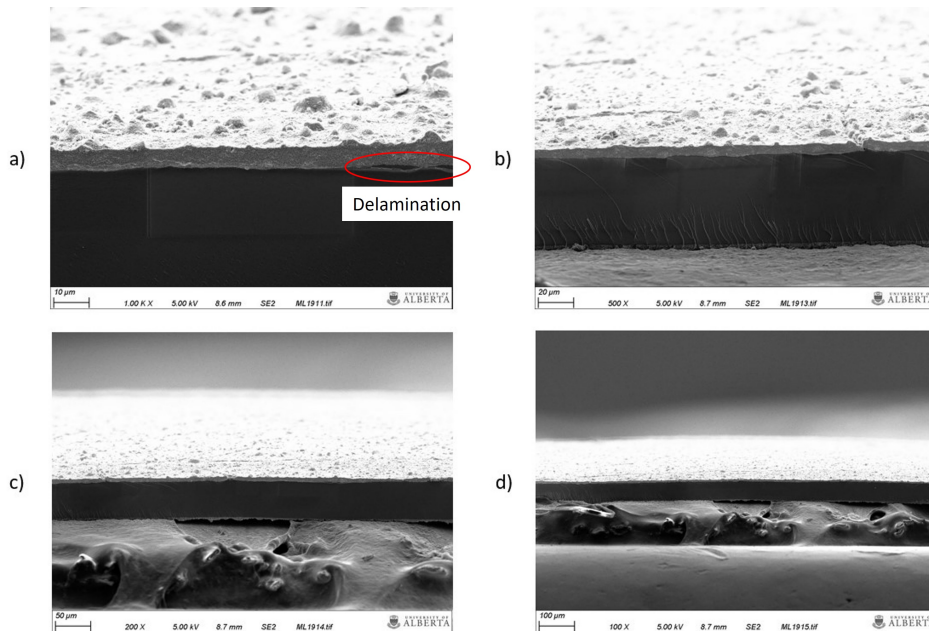


Figure 3.8: SEM images of ML19, $0.993 \text{ mg/cm}^2 \text{ IrO}_x \text{ TKK}$ at a) 1000x, b) 500x, c) 200x, d) 100x.

3.3 Electrochemical Characterization

3.3.1 Cyclic Voltammetry

CV was run before and after the pol. curves to see what degradation occurs over the beginning of life of a cell. Figure 3.9 shows the CV curves after 11 cycles in order to allow the CV to stabilize. The figure shows that the area under the curve between 0.4 and 1.25 V, which is used to estimate the ECSA and correspond to iridium oxide formation, increases with increasing iridium loading as expected.

Figure 3.10 shows the ECSA, calculated using equation 2.12, for each cell which shows a nearly constant ECSA with an increase in loading except for batch 2, ML15-ML17. Assuming a uniform layer, this was expected since the ECSA normalized by the mass of the catalyst and the same catalyst is used.

Relating to literature, in Tan's work [37] they found ECSA for IrO_x TKK of around $80 \text{ m}^2_{\text{ECSA}}/\text{g}_{\text{Ir}}$ but here it is between $25\text{-}60 \text{ m}^2_{\text{ECSA}}/\text{g}_{\text{IrO}_x}$. They used a Nafion percentage of 5 wt.% whereas in this work it is 25 wt.%. In addition they used an RDE so there was a liquid electrolyte and very low loadings in the μg range. Due to the increased coverage by the liquid electrolyte compared to the solid electrolyte used in this work, this difference in ECSA makes sense. Mandal [106] found an ECSA of $28 \text{ m}^2_{\text{ECSA}}/\text{g}_{\text{IrO}_x}$ for a $1 \text{ mg}/\text{cm}^2$ catalyst layer with 35 wt.% Nafion compared to the 41.3 and $59.2 \text{ m}^2_{\text{ECSA}}/\text{g}_{\text{IrO}_x}$ of this works 1.007 (ML23) and $1.064 \text{ mg}/\text{cm}^2$ (ML15) catalyst layers at 25 wt.% Nafion, respectively. This difference could be due to the porosity of the sample as his sample had a porosity of 15% whereas this works has a porosity of 54.1%. A higher porosity should allow for more area to be exposed for reactions to occur therefore increasing the ECSA.

Figure 3.10 also shows that the ECSA maintained a similar value before and after running the pol. curves. This indicates that the processes involved in testing the cell performance is not negatively effecting the ECSA within the cells beginning of life.

Figure 3.11 shows a closer look at the region used to estimate the double layer capacitance. The double layer capacitance was estimated using equation

1.12 at 0.2 V by looking at the magnitude of the current gap between the oxidation and reduction portions of the curve. Ideally this region is flat as the double layer is established. However, in the case of IrO_x there is not a stable double layer region as the catalyst is already in oxide form and the curve quickly diverges as reactions begin and there is faradaic current. Lower loadings experience a flatter more stable double layer than higher loadings. This may be due to there being more reaction sites in a layer with higher loading.

Figure 3.12 shows the calculated double layer capacitance for each cell before and after the pol. curves. The higher loading cells have a higher double layer capacitance which is expected since the value is not normalized by mass. However, the double layer capacitance does not increase at the same rate as the loading which is unexpected. The change from 0.25 to 1 mg/cm^2 for ML26-ML23 is only 1.4x when it should be 4x. This may be due to the beginning of oxidation and reduction peaks occurring sooner (lower voltages) for higher loadings. In addition the curves before the pol. curves in Figure 3.11 show more deviation here from the after pol. curve CVs than when looking at the oxidation peaks at higher voltage. This is also seen in Figure 3.12 where the before pol. curve double layer capacitance is about 8-10 mF/cm^2 higher than the after pol. curve CVs. Although the ECSA was not lowered for all cells due to testing, the double layer capacitance did. Since the region used to estimate the double layer capacitance was not flat it may be inaccurate and in section 3.3.4 the capacitance found by EIS will be taken as being potentially more accurate.

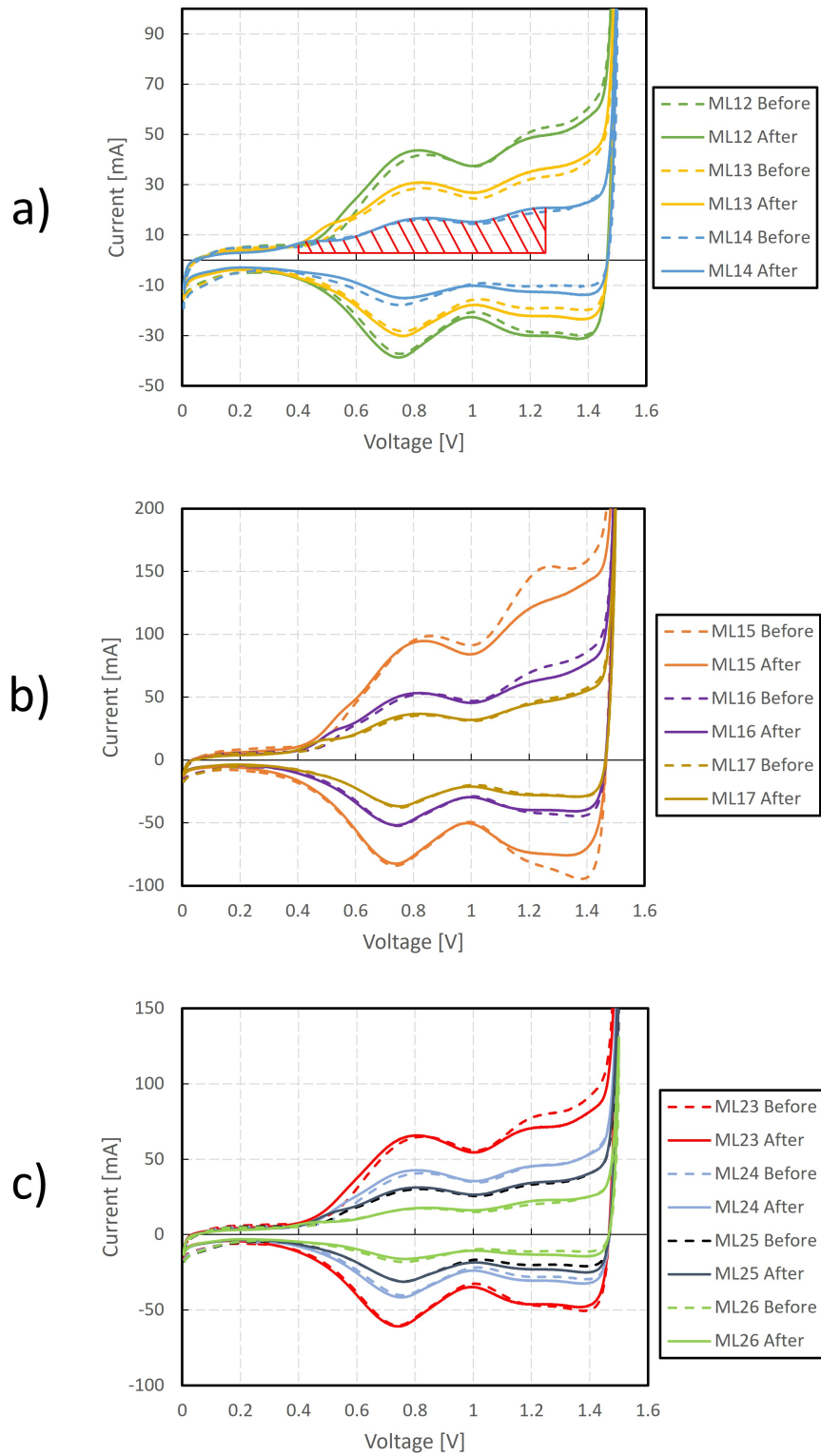


Figure 3.9: CV curves for each cell showing the stable 11th cycle from 0-1.5 V.
a) ML12-ML14, b) ML15-ML17, c) ML23-ML26

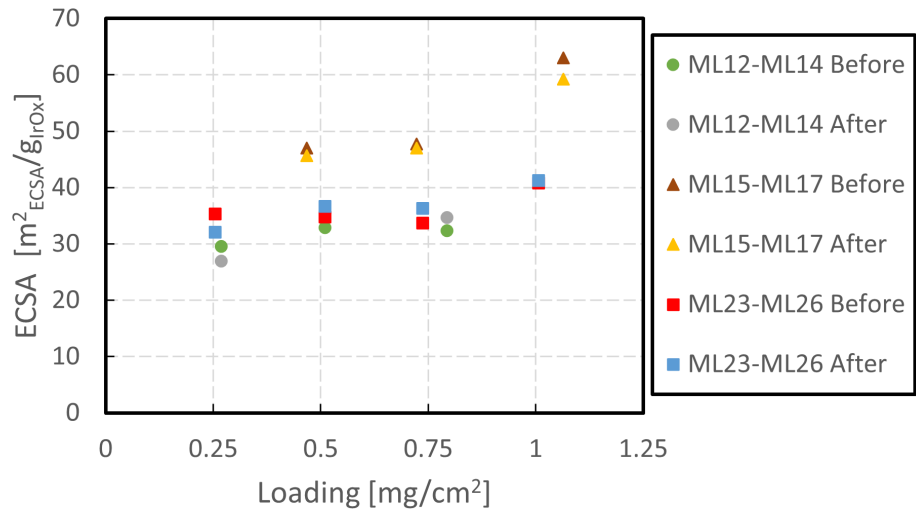


Figure 3.10: ECSA comparison between all cells separated by batch before and after polarization curves.

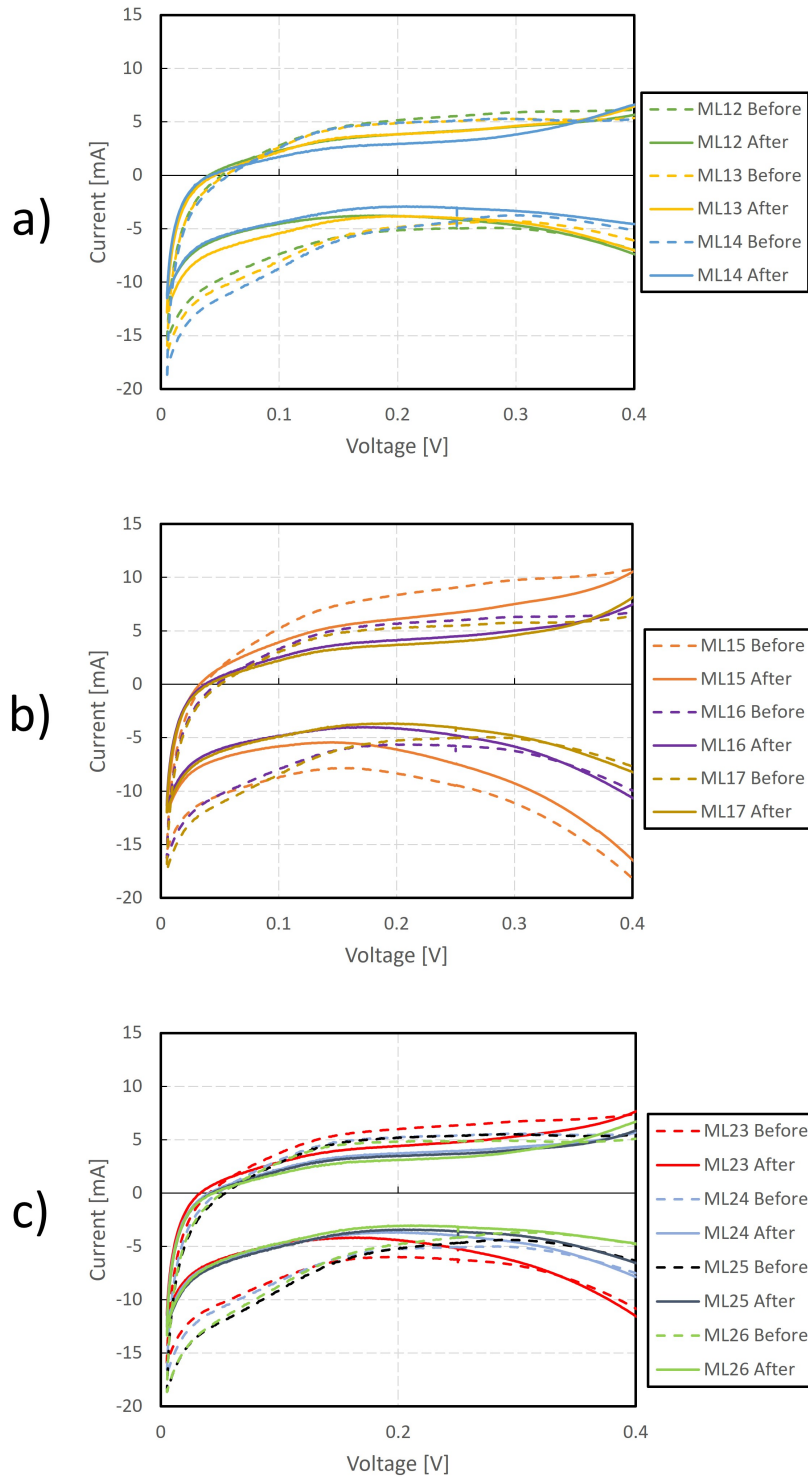


Figure 3.11: CV curves for each cell showing the stable 11th cycle from 0-0.4 V to show the electric double layer region. a) ML12-ML14, b) ML15-ML17, c) ML23-ML26

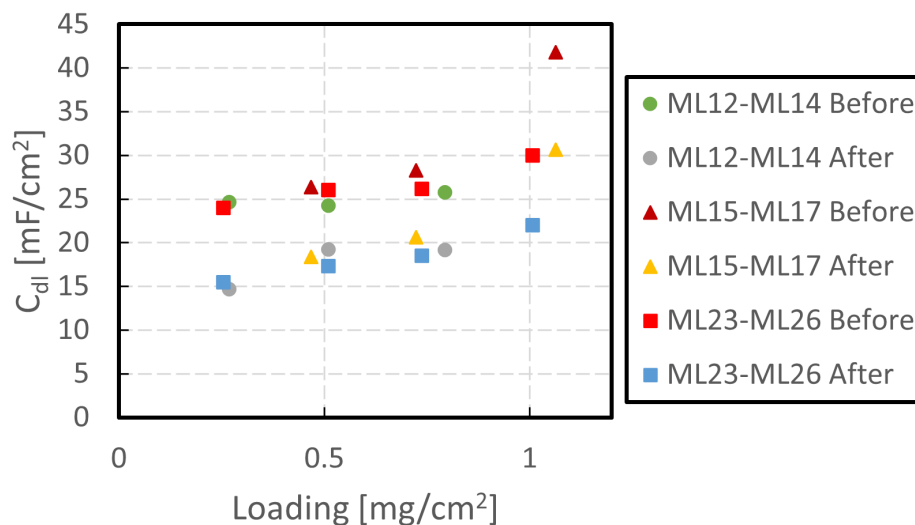


Figure 3.12: Double layer capacitance comparison between all cells separated by batch before and after polarization curves.

3.3.2 Polarization Curves

Figure 3.13 shows the polarization curves for batch 1 ML12-ML14 which shows a slight decrease in performance initially in the kinetic region below $0.5 \text{ A}/\text{cm}^2$ and then the curves converge at $4 \text{ A}/\text{cm}^2$. This means that the amount of iridium can be reduced by 4x without significantly impacting cell performance.

Figure 3.13 also shows the iR -free curves for batch 1 which shows the performance with the ohmic losses subtracted. The ohmic losses at $4 \text{ A}/\text{cm}^2$ are 265, 242 and 232 mV for ML12, ML13 and ML14, respectively showing that the losses are greater for the higher loading cases which was expected due to having a thicker catalyst layer and the fact that even the most conductive phase is likely to result in significant losses which can be observed in the HFR. It also shows that the kinetic losses are greater for the lower loading cells which was not expected since, based on Moore's model, the layer utilization was the same. This means that there is more layer utilized in the higher loadings than initially thought and some of that utilized area is lost due to the reduction in loading which could be due to a higher electrical conductivity or compression effects. However, the overall performance curves remain the same due to the ohmic losses being higher for the higher loading cells. This shows that the

ohmic and kinetic losses have an even trade off.

To ensure repeatability two more batches were tested. The pol. curves for batches 2 and 4 are shown in Figures 3.14 which shows the same trend seen previously and 3.15 which shows the low and high loading cells with lower and higher performance, respectively, than expected. The difference at 4 A/cm² between ML23 (1.007 mg/cm²) and ML26 (0.255 mg/cm²) is 44 mV. The iR-free curves loading trend for batches 2 and 4 match that of batch 1 as the iR-free performance decreases with decreased loading.

In order to analyze the differences between batches further, the three cells with the similar loading of 0.75 mg/cm² are compared and the maximum difference is obtained. Figure 3.16 shows the difference in pol. curves and iR-free pol. curves between the three batches for a loading of ≈ 0.75 mg/cm², respectively. The voltage difference at 4 A/cm² between cells ML12 and ML16 is 35.9 mV for regular pol. curves and 3.2 mV for the iR-free curves. The 1, 0.5 and 0.25 mg/cm² cells had regular pol. curve differences of 12.7, 34.3 and 2.5 while the iR-free differences were 0.5, 18.0 and 5.5, respectively. Those curves in full can be found in the Appendix Section C.0.2. Overall, this shows that there can be variation within batches on the order of 35.9 mV. This is primarily due to changes in the ohmic resistance of the cell which could be due to the differences in printing and possibly cell assembly. Ohmic resistance will be discussed further in section 3.3.4.

The 35.9 mV difference between batches is on the same order as the difference found in Figure 3.15 between loadings. Therefore we can consider that Ir loading has a negligible effect on performance.

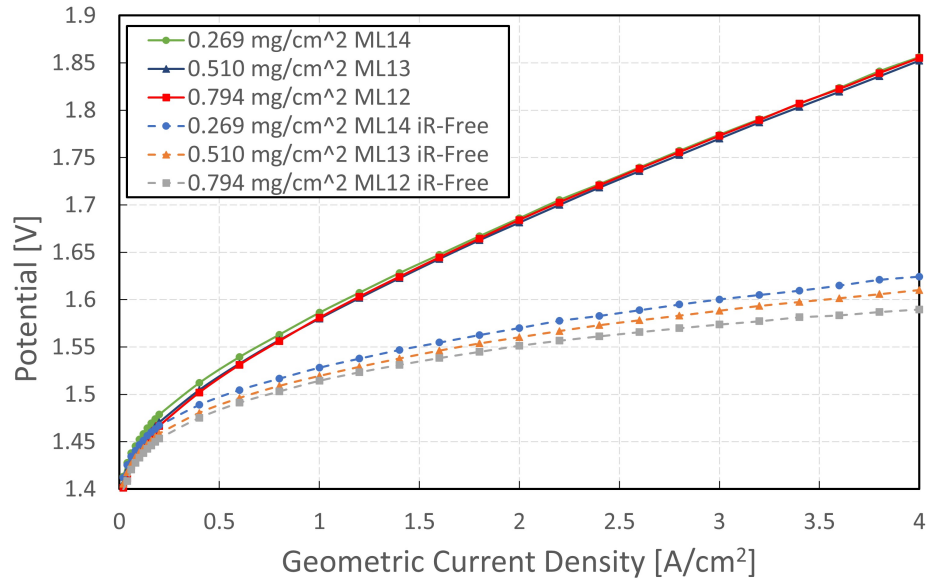


Figure 3.13: Polarization and iR-free curves of batch ML12-ML14.

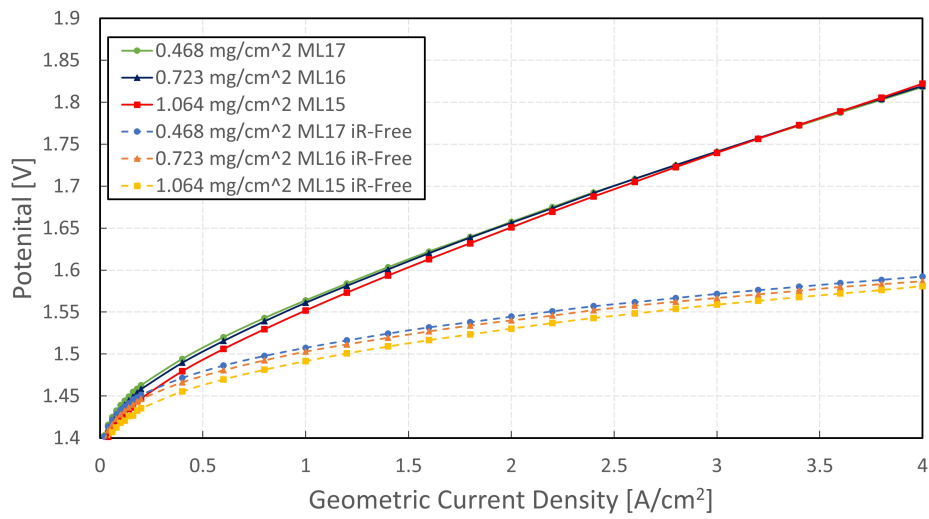


Figure 3.14: Polarization and iR-free curves of batch ML15-ML17.

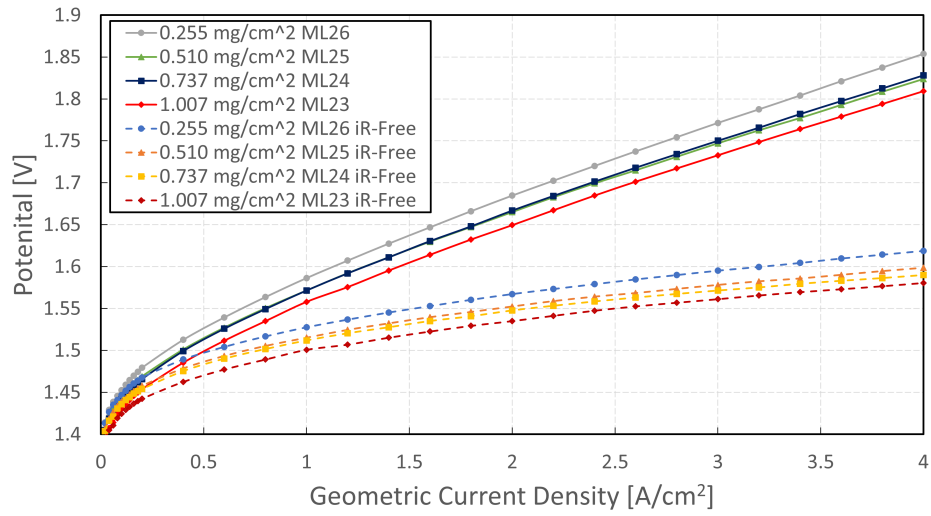


Figure 3.15: Polarization and iR-free curves of batch ML23-ML26.

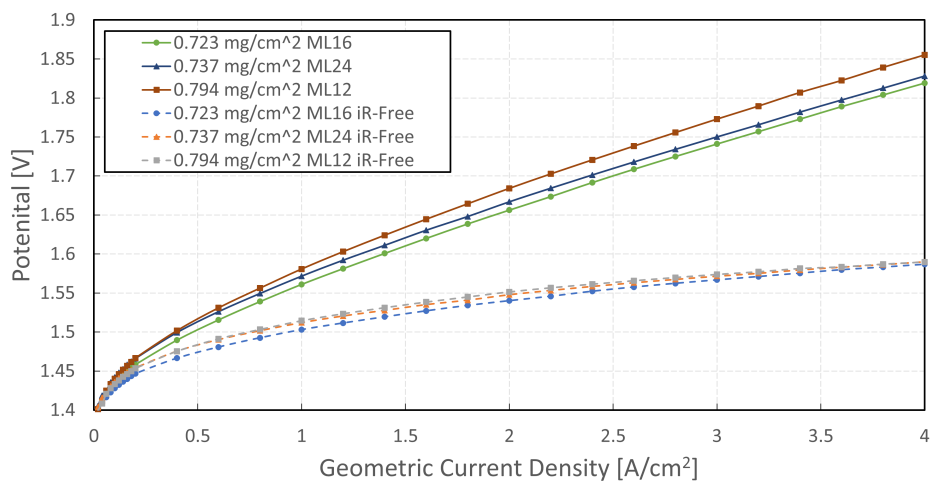


Figure 3.16: Polarization and iR-free curves of the $\approx 0.75 \text{ mg/cm}^2$ cells ML13, ML17 and ML25.

Taie et. al. [12] and Fujita et. al. [57] also studied IrO_x TKK at different loadings. Figure 3.17 shows the cell overpotential, obtained using equation 1.4 and subtracting the new potential from the standard potential of 1.23 V for OER, at 2 A/cm^2 for each study along with this work. iR -free overpotential was used for comparison since each study used a different Nafion membrane, cathode catalyst loading and Fujita's tests were done at $50 \text{ }^\circ\text{C}$ whereas this work and Taie's tests were at $80 \text{ }^\circ\text{C}$. The theoretical overpotential is 1.21 V and 1.18 V at 50 and $80 \text{ }^\circ\text{C}$, respectively. The figure shows that the results of this work are in line with literature as there is less than a 50 mV difference for similar loadings. In the future we would like to go to loadings less than 0.1 mg/cm^2 to reach a loading where significant loss in performance could be observed. Fujita found at 0.2 mg/cm^2 further loading reductions started to severely effect performance whereas Taie found a significant decrease below 0.011 mg/cm^2 .

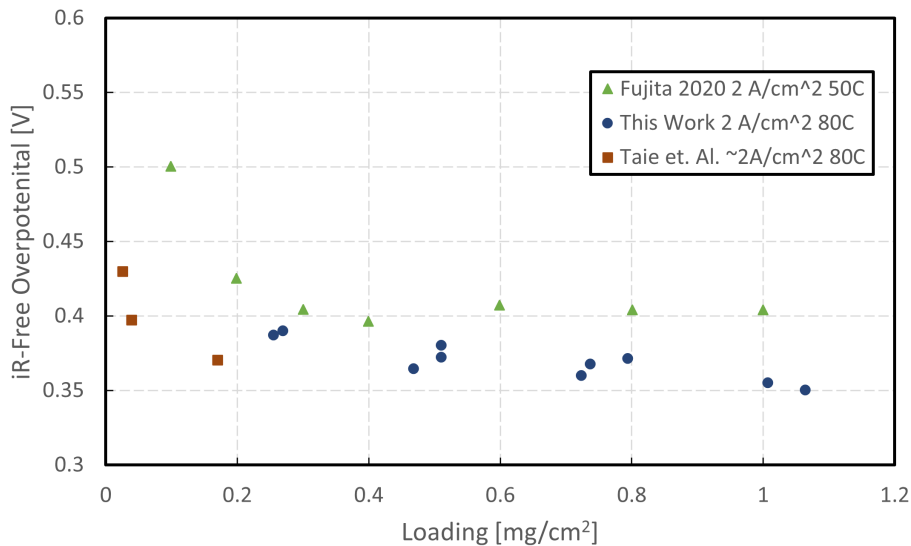


Figure 3.17: iR -free overpotentials at 2 A/cm^2 [12, 57].

3.3.3 Linear Scan Voltammetry

Figure 3.18 shows the BV plots for each batch which did not turn out as expected where the anode portion of the curve is offset by about 0.2 V. The loading also appears to effect where this point is as the Tafel curves shift to the right with decreasing loading. This is the same effect seen in the polarization curves since the low loading cells have more losses initially and then due to the lower ohmic resistance eventually perform the same as the higher loading cells. The kinetic parameters were extracted from the range of 4-80 mA/cm² using Tafel analysis.

Figure 3.19 shows the Tafel slope for each cell compared to Taie's study [12]. The Tafel slope for this work is similar across all loadings. Taie's data continues the trend from this work as they went to lower loadings and once they reached 0.039 mg/cm² the Tafel slope began to increase substantially.

Figure 3.20 shows the exchange current density for this work as a function of the catalyst loading compared to literature data. The values for this work decrease slightly with an increase in loading which is not expected since it is the same catalyst which should have the same inherent activity. This shows that the whole catalyst layer is not being utilized. However, when multiplied by the loading there is still less kinetic losses for the higher loading cells as seen in the iR-free curves previously.

It was found that, at both the low and high loadings, the exchange current density is much lower in this work than literature for other cells using IrO_x or IrO₂ [12, 28]. This could be due to error in choosing an appropriate section to extract the kinetic parameters due to the complexity of the OER compared to the standard Tafel assumptions.

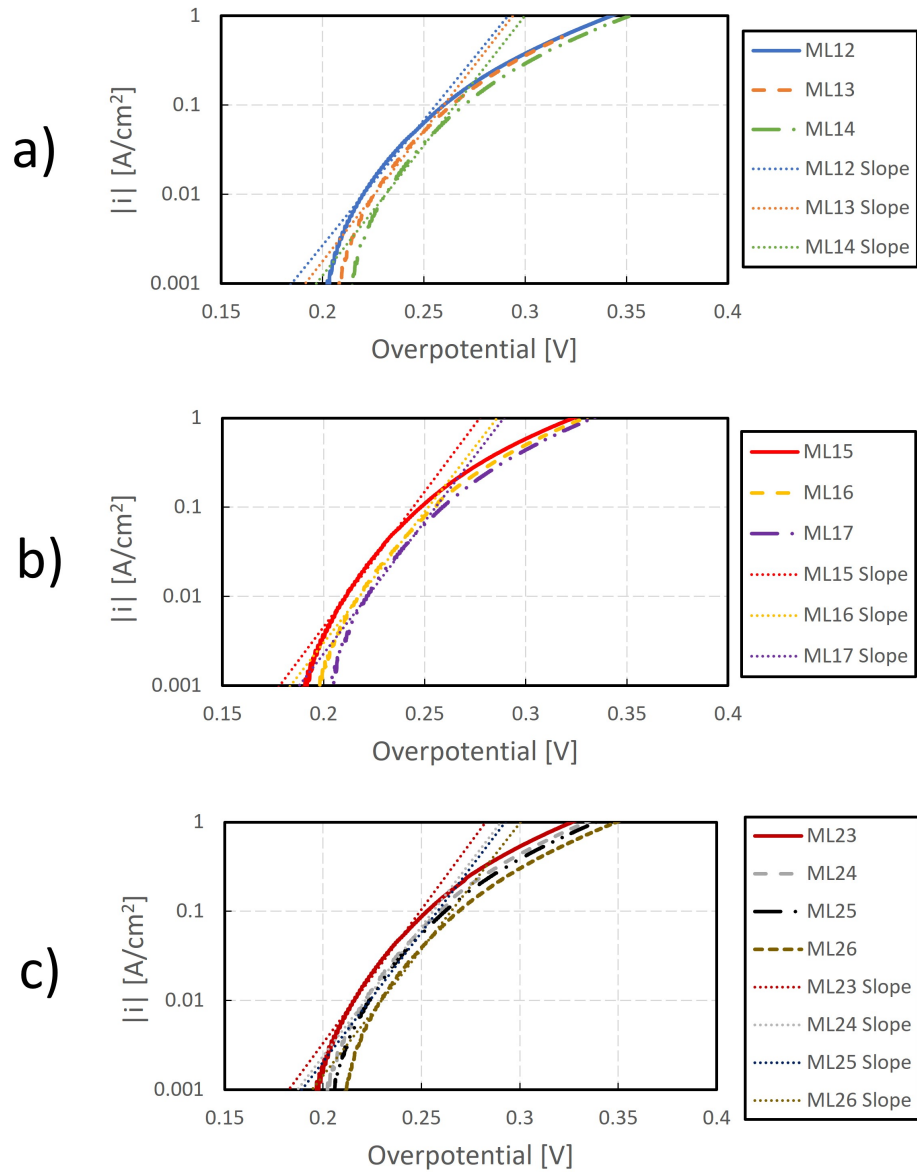


Figure 3.18: Butler-Volmer plots for a) ML12-ML14, b) ML15-ML17, c) ML23-ML26

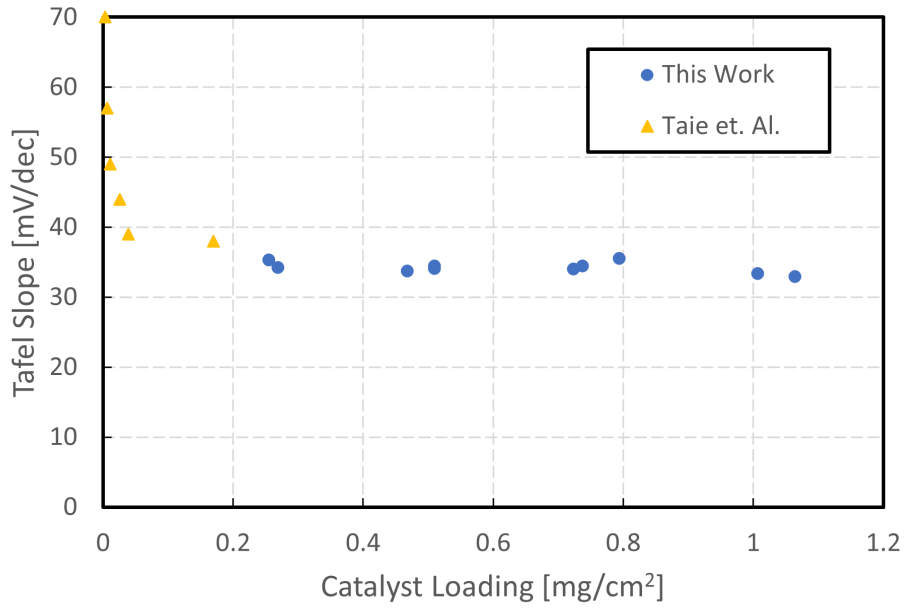


Figure 3.19: Tafel slope comparison between all cells in this work and Taie et. al. loading study [12].

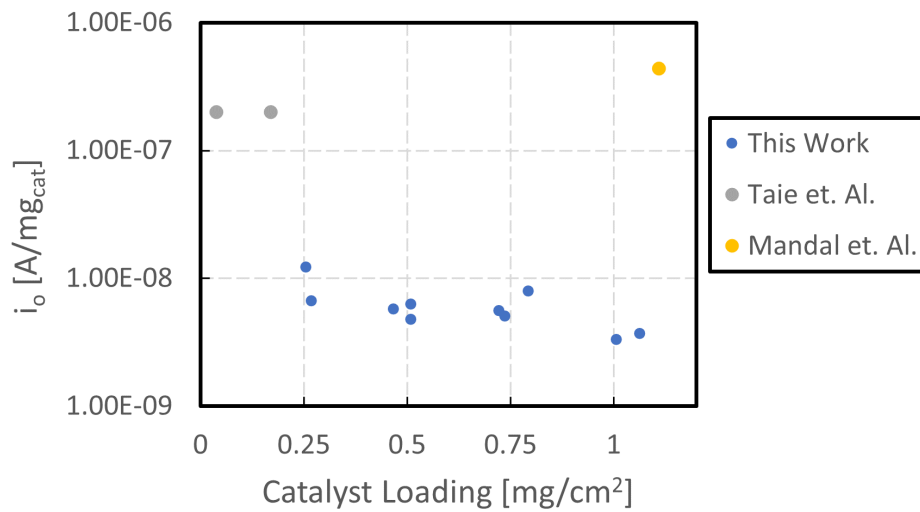


Figure 3.20: Comparison of exchange current density normalized by the mass of catalyst. Taie et. al. [12], Mandal et. al. [28].

3.3.4 Electrochemical Impedance Spectroscopy

Figure 3.21 and 3.22 shows the Nyquist plots and related frequency plots, respectively, for all cells at 0.1 A. The raw data for each cell as well as the fitted curve are plotted. The fitted curve was found using the equivalent circuit in Figure 2.10. Table 3.4 contains the fitting parameters for each cell at 0.1, 1 and 10 A and will be used alongside the plots to determine the effects of loading on the impedance of a cell.

The equivalent circuit consists of R_1 which represent the ohmic resistance defined by the most conductive phase in the HFR which is found from R_1 by multiplying by the catalyst area, Q_2 and R_2 which represent the cathode catalyst layer, and Q_3 and R_3 which represent the anode catalyst layer. The pseudo capacitance associated with Q_2 and Q_3 would then correspond to the double layer capacitance of the cathode and anode, respectively.

In Figure 3.21 two semicircles can be observed for each cell. The first semicircle is thought to represent the cathode while the second larger semicircle represents the anode. Figure 3.23 shows the pseudo capacitance for each semicircle, found using equation 2.13, of each cell along with the double layer capacitance from the CVs. Pseudo capacitance was found for the 0.1 A Nyquist plot to avoid transport effects. C_2 , corresponding to the first semicircle, is similar across all loadings for each batch. This was expected since the cathode for all cells should be similar with only small variations in Pt loading.

Figure 3.23 shows that both the pseudo capacitance C_3 and double layer capacitance increase with loading but C_3 is much larger in magnitude than the double layer capacitance from the CVs. This is likely due to two factors. First, the double layer capacitance found from CV in section 3.3.1 may not be accurate due to presence of faradaic current. Second, the conditions the CV and EIS experiments were run under are completely different. CV is run at 30 °C while EIS is run at 80 °C. CV has flowing hydrogen at the cathode while EIS has static hydrogen just produced by the running of the cell. Table 3.4 shows the value of C_3 for each cell at various applied currents which shows that the value of C_3 decreases as the current increases. This makes sense as

the higher current promotes more oxygen evolution which displaces area where the double layer forms due to gas bubbles.

The width of each semicircle along the x-axis corresponds to the charge transfer resistance. The second semicircle being larger than the first one indicates a larger charge transfer loss in the anode. This is expected, since the more sluggish oxygen evolution reaction occurs at the anode. Figure 3.25 shows the change in R_3 across all cells for each applied current. R_3 goes up slightly as loading decreases for batch 1 which is expected since there is less catalyst available to help the reaction proceed. Batch 2 and 4 go up and down but follow the same trend a bit more loosely. R_3 also decreases with an increase in current which again is expected since the overpotential is larger which creates a larger driving force for charge transfer.

Figure 3.21 shows a difference in the slope of the curve between the beginning of the curve and 0.03Ω on the y-axis. This slope creates a distinction between the first and second semicircles with the first semicircle disappearing into the second semicircle. Figure 3.24 shows simulated EIS curves which were made by holding all parameters constant except for the CPE, Q_3 . It was found that decreasing the value of Q_3 caused an increase in the slope and less distinction between the semicircles. Then comparing this result to the values of Q_3 in Table 3.4 there is a decrease of Q_3 with a decrease in loading which corresponds to the increase in slope seen in the Nyquist plots. The decrease in Q_3 also means a decrease in the capacitance of the layer which makes sense for a decrease in loading as there is less catalyst area for the double layer to form over.

Figure 3.26 shows the HFR for each cell used to calculate the iR -free curves. The general trend is that the HFR increases slightly with loading which is why the pol. curves converge at high current densities since the kinetic losses are offset by the ohmic losses. In Moore's model it was predicted that the performance of low loading cells did not just match that of higher loadings but surpassed them. It is possible that the HFR should be larger than what is seen here due to IrO_x 's low electrical conductivity. This could mean that the catalyst layer is more conductive than initially theorized. This

will be discussed further in Section 3.4.

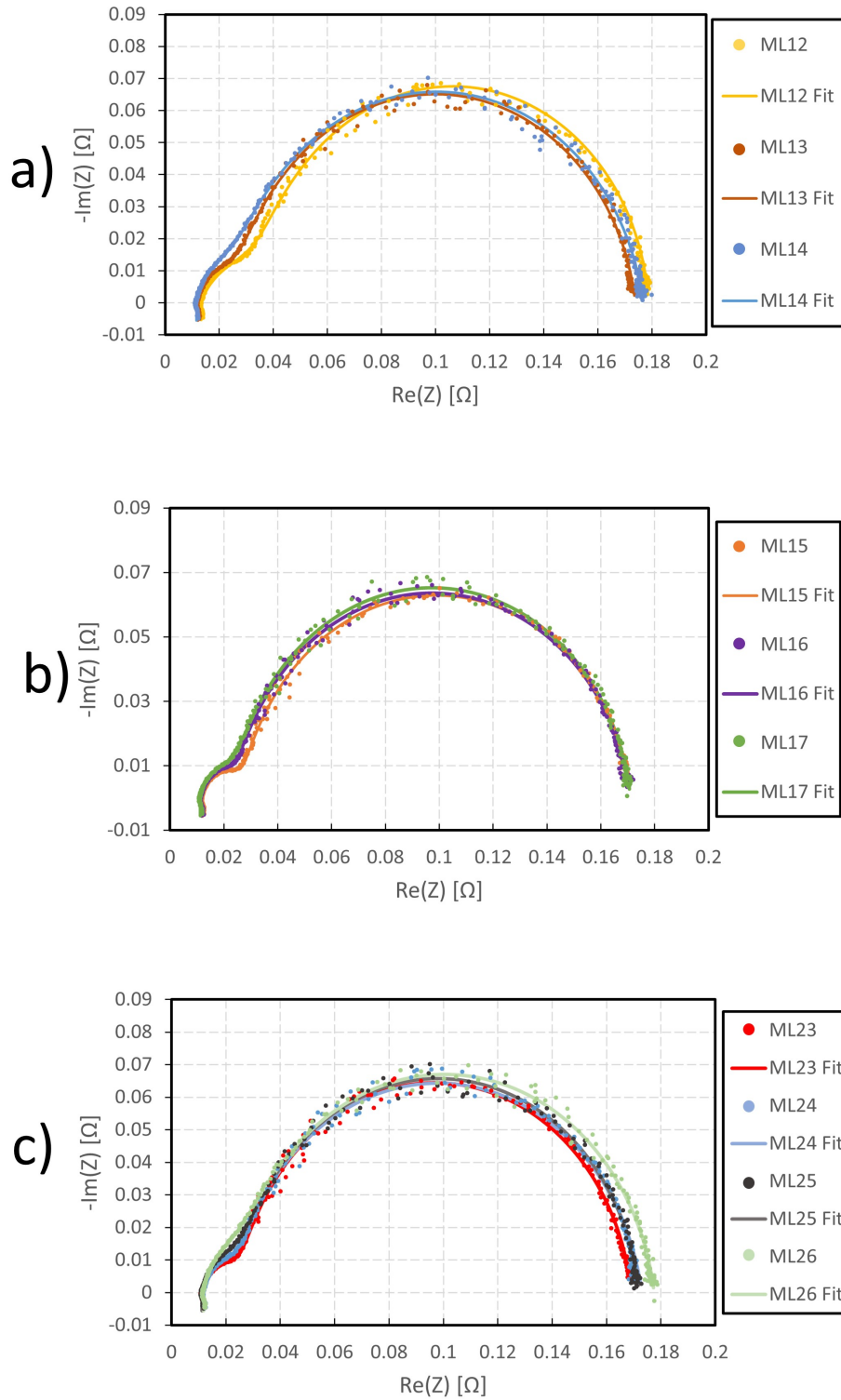


Figure 3.21: Nyquist plots for each batch of cells at 0.1 A from 100 kHz to 20 mHz. a) ML12-ML14, b) ML15-ML17, c) ML23-ML26

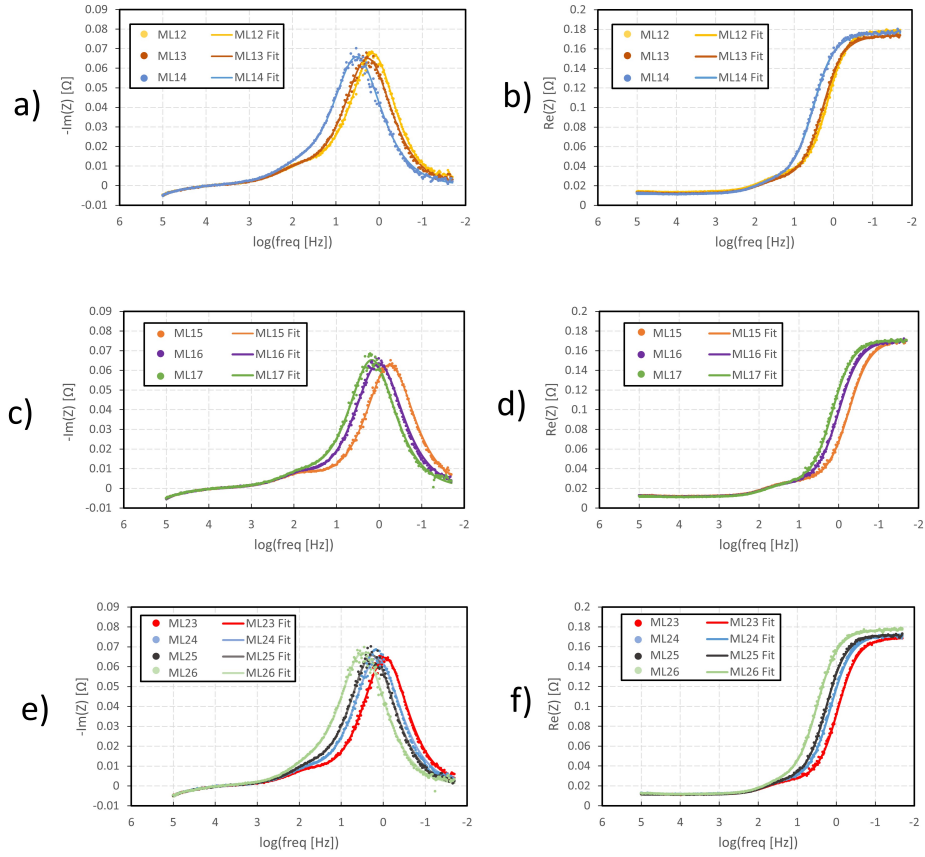


Figure 3.22: Frequency vs real and imaginary components of the impedance for each batch of cells at 0.1 A from 100 kHz to 20 mHz. $-\text{Im}(Z)$ vs $\log(\text{freq})$ a) ML12-ML14, c) ML15-ML17, e) ML23-ML26. $\text{Re}(Z)$ vs $\log(\text{freq})$ b) ML12-ML14, d) ML15-ML17, f) ML23-ML26

Table 3.4: Fitting parameter values for EIS performed at 0.1, 1 and 10 A along with the pseudo capacitance related to each respective CPE and the double layer capacitance from the previous CVs.

Cell	Current (A)	L1 (H)	R_1 (Ω)	Q_2 ($F \cdot s^{a-1}$)	a_2	R_2 (Ω)	Q_3 ($F \cdot s^{a-1}$)	a_3	R_3 (Ω)	Pseudo C_2 (mF/cm^2)	Pseudo C_3 (mF/cm^2)	C_{dl} (mF/cm^2)
ML12	0.1	8.64E-09	0.0133	0.561	0.756	0.0246	0.892	0.959	0.141	28.091	163.315	19.143
ML13	0.1	8.86E-09	0.0121	0.267	0.884	0.0153	0.720	0.921	0.146	25.942	118.587	19.259
ML14	0.1	8.82E-09	0.0116	0.253	0.886	0.0147	0.430	0.909	0.150	24.683	65.377	14.693
ML15	0.1	9.12E-09	0.0121	0.278	0.900	0.0148	2.193	0.910	0.145	30.266	391.505	30.648
ML16	0.1	9.00E-09	0.0117	0.183	0.970	0.0119	1.252	0.904	0.148	30.342	209.181	20.633
ML17	0.1	8.89E-09	0.0113	0.280	0.907	0.0132	0.871	0.923	0.147	31.628	146.519	18.398
ML23	0.1	8.86E-09	0.0114	0.330	0.896	0.0141	1.384	0.929	0.143	35.300	244.574	22.017
ML24	0.1	8.60E-09	0.0119	0.193	0.977	0.0116	0.934	0.903	0.149	33.260	151.244	18.507
ML25	0.1	8.94E-09	0.0113	0.315	0.900	0.0146	0.711	0.928	0.146	34.735	119.232	17.328
ML26	0.1	8.72E-09	0.0117	0.325	0.898	0.0129	0.449	0.902	0.153	34.893	66.989	15.491
ML12	1	6.96E-09	0.0133	0.397	0.820	0.0118	0.990	0.882	0.0151	24.543	112.659	19.143
ML13	1	6.72E-09	0.0120	0.323	0.870	0.0091	0.653	0.893	0.0170	27.045	75.950	19.259
ML14	1	7.20E-09	0.0116	0.717	1.000	0.0074	0.257	0.846	0.0187	143.420	19.510	14.693
ML15	1	7.68E-09	0.0120	0.270	0.905	0.0095	2.087	0.882	0.0155	28.846	263.911	30.648
ML16	1	7.52E-09	0.0116	0.303	0.892	0.0096	1.191	0.916	0.0151	29.920	164.752	20.633
ML17	1	7.33E-09	0.0112	0.319	0.898	0.0084	0.862	0.900	0.0159	32.414	106.960	18.398
ML23	1	7.17E-09	0.0114	0.395	0.863	0.0115	1.494	0.945	0.0133	33.422	238.264	22.017
ML24	1	7.00E-09	0.0116	1.124	0.929	0.0124	0.454	0.836	0.0128	161.957	33.143	18.507
ML25	1	7.38E-09	0.0113	0.392	0.888	0.0087	0.670	0.896	0.0164	38.200	79.591	17.328
ML26	1	7.20E-09	0.0109	1.929	0.132	0.0007	0.246	0.864	0.0262	5.18E-17	22.233	15.491
ML12	10	7.25E-09	0.0129	0.697	0.508	1.69E-10	2.440	0.649	0.0053	3.47E-08	46.295	19.143
ML13	10	6.74E-09	0.0015	2.199	0.664	0.0051	4.258	0.020	0.0110	45.459	4.12E-64	19.259
ML14	10	7.10E-09	0.0116	47.420	0.597	0.0019	0.312	0.882	0.0035	1833.107	25.040	14.693
ML15	10	7.55E-09	0.0121	55.370	0.645	0.0018	1.066	0.803	0.0038	3121.540	55.256	30.648
ML16	10	7.35E-09	0.0116	138.800	0.702	0.0010	0.738	0.823	0.0042	11975.572	42.763	20.633
ML17	10	7.46E-09	0.0112	30.940	0.549	0.0020	0.409	0.911	0.0031	630.080	42.519	18.398
ML23	10	7.10E-09	0.0113	197.300	1.000	0.0005	0.986	0.790	0.0046	39460.000	46.819	22.017
ML24	10	6.99E-09	0.0116	71.330	0.926	0.0007	0.698	0.819	0.0044	11263.642	38.999	18.507
ML25	10	7.34E-09	0.0112	352.000	0.831	0.0006	0.731	0.809	0.0045	50944.949	37.852	17.328
ML26	10	7.19E-09	0.0116	46.690	0.621	0.0015	0.353	0.878	0.0037	1857.192	28.147	15.491

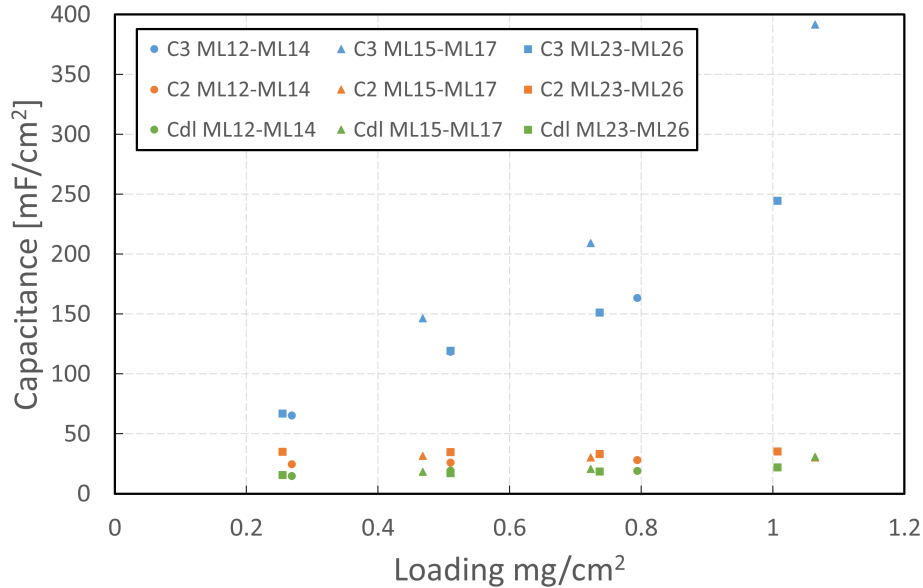


Figure 3.23: Pseudo capacitance for the first (C_2) and second (C_3) semicircles from the Nyquist plots at 0.1 A compared to the double layer capacitance from the CVs.

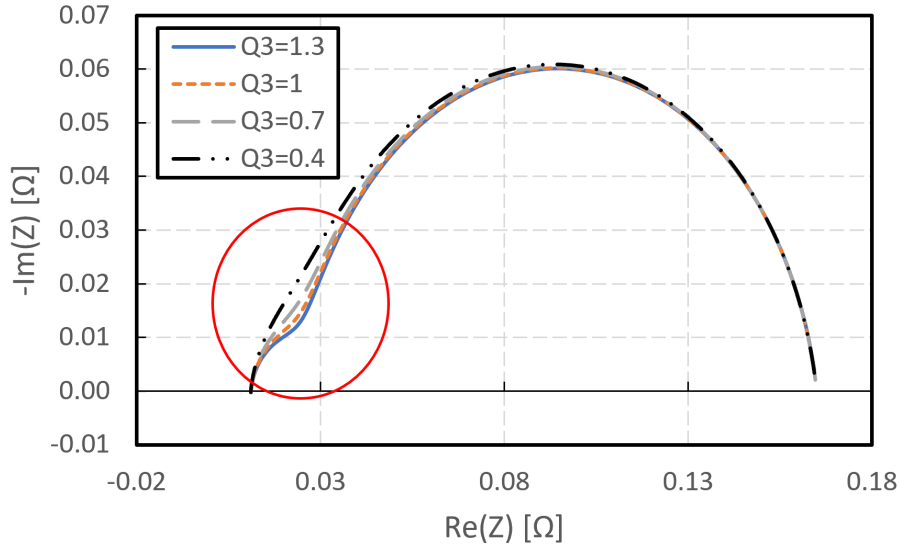


Figure 3.24: Nyquist plots from EIS simulations to show the effect of changing Q_3 . Q_3 is in units of $F \cdot s^{a-1}$. Parameters kept constant are $L=8E-9$ H, $R_1=0.011$ Ω , $Q_2=0.33$ $F \cdot s^{a-1}$, $a_2=0.9$, $R_2=0.014$ Ω , $a_3=0.9$, $R_3=0.14$ Ω .

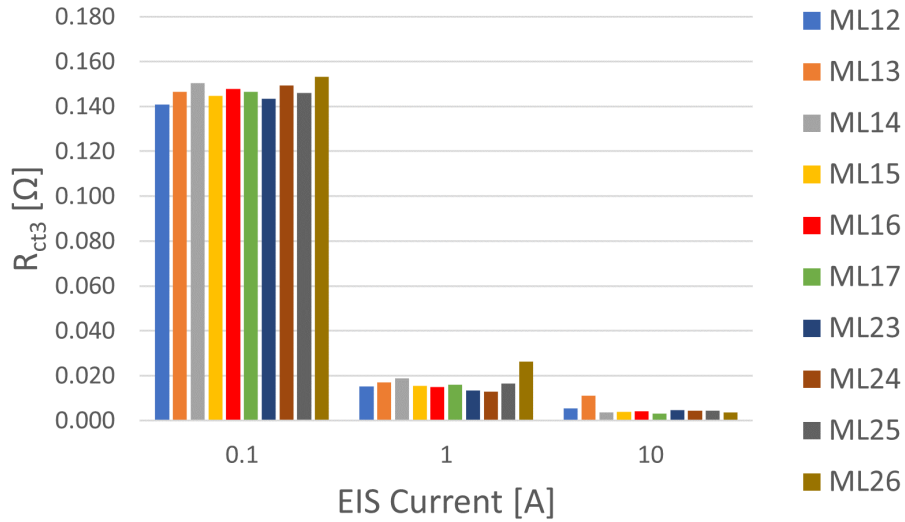


Figure 3.25: R_{ct3} for each cell when the EIS applied current is 0.1, 1 and 10 A.

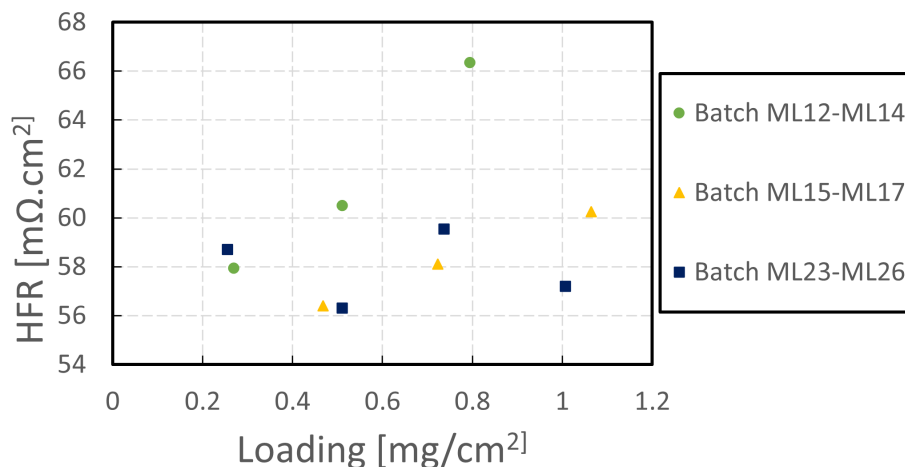


Figure 3.26: HFR comparison between all cells separated by batch.

3.3.5 In-Situ Compression Effects

After finding that the performance of low loading cells is similar to high loading cells at high current density it was questioned as to why the expected improvement in performance with reduced electrode thickness was not observed considering that it was hypothesized electronic conductivity was limiting. It was hypothesized that electrical conductivity was higher due to compression of the cell. Figure 3.27 shows the surface of cell ML15's catalyst layer after testing which has indentations from the PTL. The effect of compression was studied by testing the performance of the four cells seen in Table 3.5 at lower compression. The pinch was changed from the standard value of about $67 \mu\text{m}$ to about $-8 \mu\text{m}$ which means that there will be little contact between the CCM and PTL due to putting the cell together. Instead the contact will primarily come from the swelling of the Nafion membrane when the cell receives water.

Figure 3.28 shows the pol. curves for each cell. The low compression cells have significantly worse performance at 2 A/cm^2 with a 394 mV and 114 mV loss for the $\approx 0.25 \text{ mg/cm}^2$ and $\approx 1 \text{ mg/cm}^2$ cells, respectively. The HFR and ECSA reflect this as the HFR for cell ML10 is about three times higher than ML5, and the HFR for ML9 is just under twice as much as ML6 leading to much higher ohmic losses. The ECSA decreased by $8.062 \text{ m}^2/g_{cat}$ and $27.053 \text{ m}^2/g_{cat}$ for the $\approx 0.25 \text{ mg/cm}^2$ and $\approx 1 \text{ mg/cm}^2$ cells, respectively. This may

be due to less contact with the PTL which would restrict electron transport as well as having less fibers PTL fibers touching the surface which due to any cracks in the layers would lead to a lower ECSA.

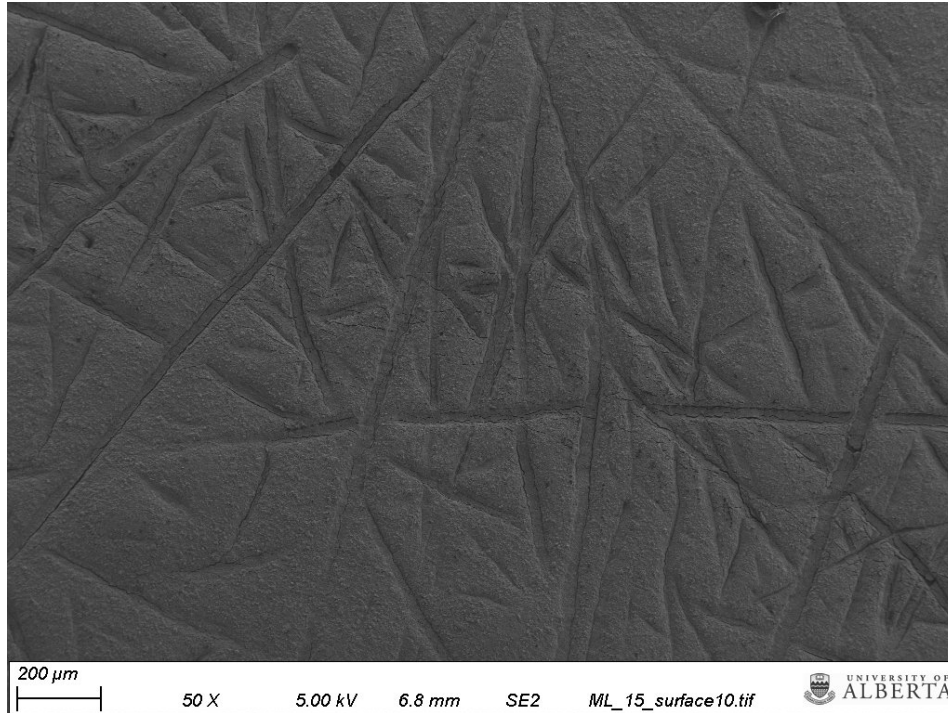


Figure 3.27: SEM image of cell ML15 after testing showing the indentations created by the PTL pushing into the CCM.

Table 3.5: Cell HFR and ECSA with pinch changed to test the effect of no compression. These cells were printed with 10 pL cartridges.

Cell	Loading (mg/cm ²)	Anode Gasket (μm)	Pinch (μm)	HFR (mΩ·cm ²)	ECSA (m ² /g _{cat})
ML5	0.255	150	67	61.5	25.758
ML6	0.99	150	67	64	52.758
ML9	0.99	230	-8	106.75	25.705
ML10	0.285	230	-8	176.7	17.696

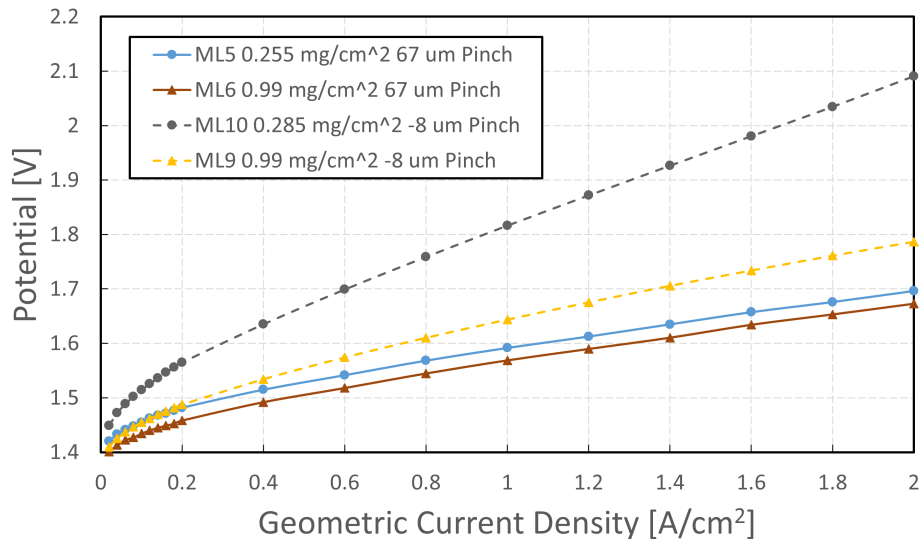


Figure 3.28: Cell polarization curves for pinch values of 67 and -8 μm .

3.4 Ex-Situ Compression Effects

For an $\approx 1 \text{ mg/cm}^2$ IrO_x TTK catalyst layer with 25wt.% Nafion, the through-plane electronic conductivity was previously found by Mandal et. al. to be $154 \mu\text{S/cm}$ at 30% relative humidity and decreased to $44 \mu\text{S/cm}$ at 100% relative humidity [29]. However, the effect of compression was not studied. To measure the effect of compression more closely, the through-plane conductivity was measured by a compression cell under various pressures, previously explained in Section 2.3.2 and calculated using equation 2.11.

Figure 3.29 shows the sheet resistivity as it changes with catalyst layer thickness. This graph should be representative of equation 2.11 but when linear fitting is done the fit does not go through (0,0). Instead it goes through about $1.3 \mu\text{m}$. So, to calculate the conductivity the linear fit was forced through zero. The reason for the deviation could be that the compressed thickness is not being accounted for, as the thickness in Figure 3.29 is the uncompressed thickness. Profilometry was conducted on each compressed catalyst layer but the compressed area thickness was not determined. Another possibility could be a change in electrical conductivity with loading or the gold block may be able to puncture or scrape the catalyst layer and make some direct contact with

the gold plate below also leading to an increase in the resultant conductivity.

Figure 3.30 shows the conductivity at various pressures found from the linear fits, where the conductivity increases linearly with pressure likely due to better contact between the gold block and the catalyst layer.

Comparing to the values found by Mandal, the 44-154 $\mu\text{S}/\text{cm}$ range falls above the conductivity found in this work [29]. The deviation from literature indicates that the compression of the cell as well as the loading are important to consider when determining catalyst layer through-plane electronic conductivity.

Given the discrepancy in conductivity with literature as well as an unexpected intercept in Figure 3.29, more testing is required to come to a conclusion regarding the conductivity of these layers.

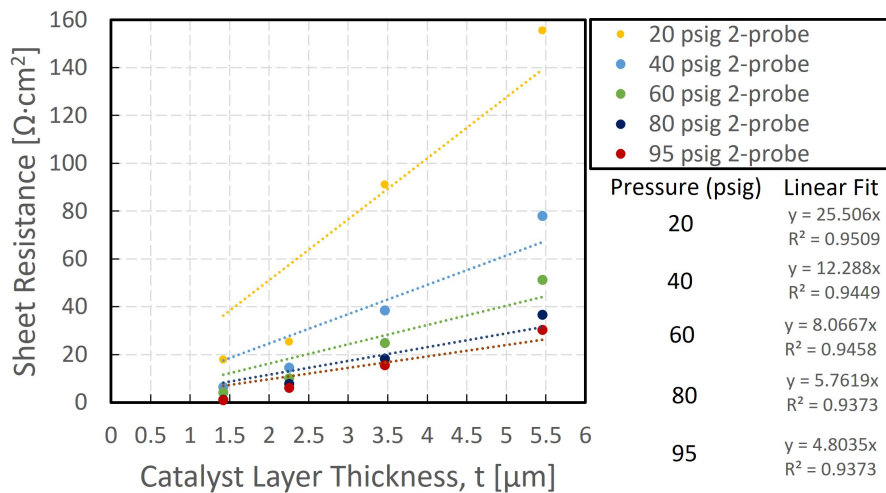


Figure 3.29: Sheet resistance as a function of the catalyst layer thickness.

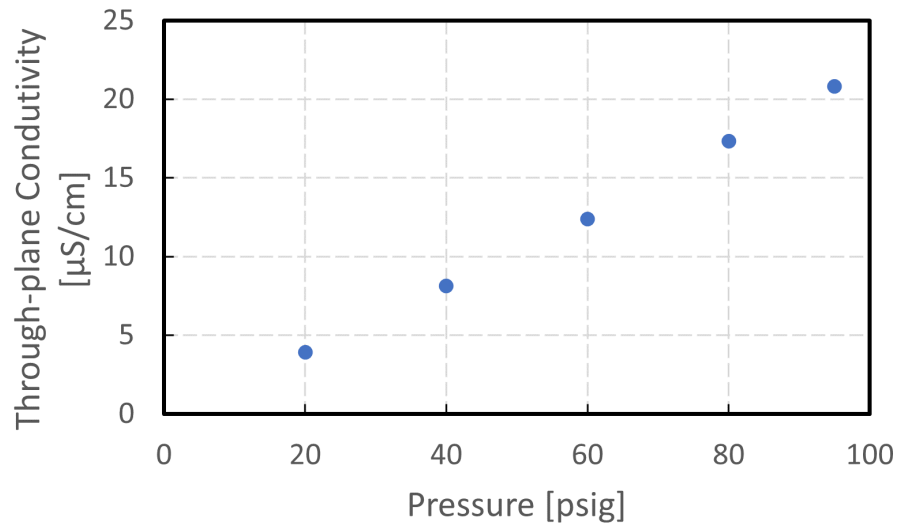


Figure 3.30: IrO_x TKK catalyst layer through-plane conductivity as a function of pressure.

Chapter 4

Ir-Ni Catalyst Upscaling and Assessment in a PEMWE

This chapter focuses on preparing Ir_8NiO_x through an alkaline aqueous reaction and upscaling to an MEA using inkjet printing. First the preparation of the ink is discussed followed by what happened when the catalyst was printed and subsequently tested and characterized in an MEA.

4.1 Catalyst Characterization

The catalyst synthesis was done twice separately to make two batches of catalyst particles following the procedure outlined in section 2.1. The yield for batch 1 and batch 2 was 426.1 and 369.9 mg, respectively due to slightly different temperature conditions during precipitation as well as the amount of re-dispersion achieved between each washing cycle. Inkjet printing requires about 117 mg of IrO_x per batch which means that a few batches of ink were made with each batch of catalyst powder.

TEM/EDX for batch 1 and 2 are shown in Figures 4.1 and 4.2, respectively. The samples could not be imaged at a higher magnification with good resolution due to interference from the hydrocarbons contained in the tert-butanol used to precipitate the catalyst. The hydrocarbons are decomposed by the electron beam into a layer that accumulates on the surface of the particle of interest obstructing the view and the effect increases with increased magnification [107, 108]. Due to the limited amount of particles measured the

agglomerate size measured here is not representative of each batch entirely. The TEM images show an agglomerate of the Ir_8NiO_x catalyst. An approximate size for the agglomerates found in each batch is given by the characteristic diameter of the smallest circle that can encapsulate the entire particle. The batch 1 agglomerate is about 814 nm and batch 2 contains two particles, 1760 nm and 1290 nm. Compared to the original synthesis by Moghaddam et. al. [67] the particle size found in this work is orders of magnitude larger as they found the particle size to be 1-2 nm. The difference in particle size indicates that it is unlikely that the catalyst that was made here is the same as the original paper. The discrepancy in size may be due to differences in procedure when precipitating and handling the catalyst after synthesis. Differences could also occur from the act of scaling up the size of the reaction.

The elemental composition obtained by EDX and shown in the previous figures is in Table 4.1. The atomic Ir:Ni ratio is not in the expected 8:1 at.% range [67]. Batch 1 and 2 have an Ir:Ni atomic ratio of 495:1 and 3.27:1 at.%, respectively. The reason for the discrepancy appears to be that in Moghaddam's work [67] the Ir-Ni ratio, obtained by ICP-MS, was found for the non-precipitated particles in a bulk solution which focuses on the bulk properties, whereas this work looked at the individual precipitated particle aggregates. This suggests that the bulk Ir-Ni ratio may be 8:1 at.% but each individual particle could have a higher or lower atomic ratio. This is seen in the extremely low Ni signal in batch 1's particle compared to batch 2 which actually had more Ni than expected. This may have an impact on the electrochemical performance of the catalyst in an MEA since not all the Ir particles contain Ni and therefore do not benefit from the enhanced bi-metallic properties. Another explanation could be that since the EDX is primarily a surface reading that the Ni is mostly below the surface.

Oxygen has the highest atomic percentage at 69.4% and 33.1% for batch 1 and 2, respectively. Rutile-type IrO_2 has an O:Ir ratio of 2:1 at.% Iridium while IrO_x , which is considered amorphous meaning it contains Ir(III) and Ir(IV), has an O:Ir ratio between 2:1 and 1.5:1 at.% [109, 110]. Using these two ratios as typical structures, it can be seen that the 7.01:1 and 1.27:1 at.%

are atypical. The difference in O:Ir ratio may be due to a number of factors. Firstly, the exact structure of the Ir_8NiO_x catalyst is not known so how the presence of Ni offsets the Ir is unknown and there could be extra hydroxide and water molecules attached to the catalyst. Secondly, as stated above there is tert-butanol present which contains some hydroxide groups contributing to the overall oxygen content. Finally, there are also traces of potassium which suggest that the KOH used in the reaction to form the catalyst has not been completely washed away. The potassium will likely also decrease cell performance due to possible migration of K^+ ions into the Nafion membrane which could hinder the motion of protons to the cathode.

In addition to the presence of K, there are also traces of Cl. This again is due to the catalyst precursors containing Cl and insufficient washing during centrifugation. Further washing could have been done but this would greatly reduce the catalyst yield which is already only enough to fabricate a few inks.

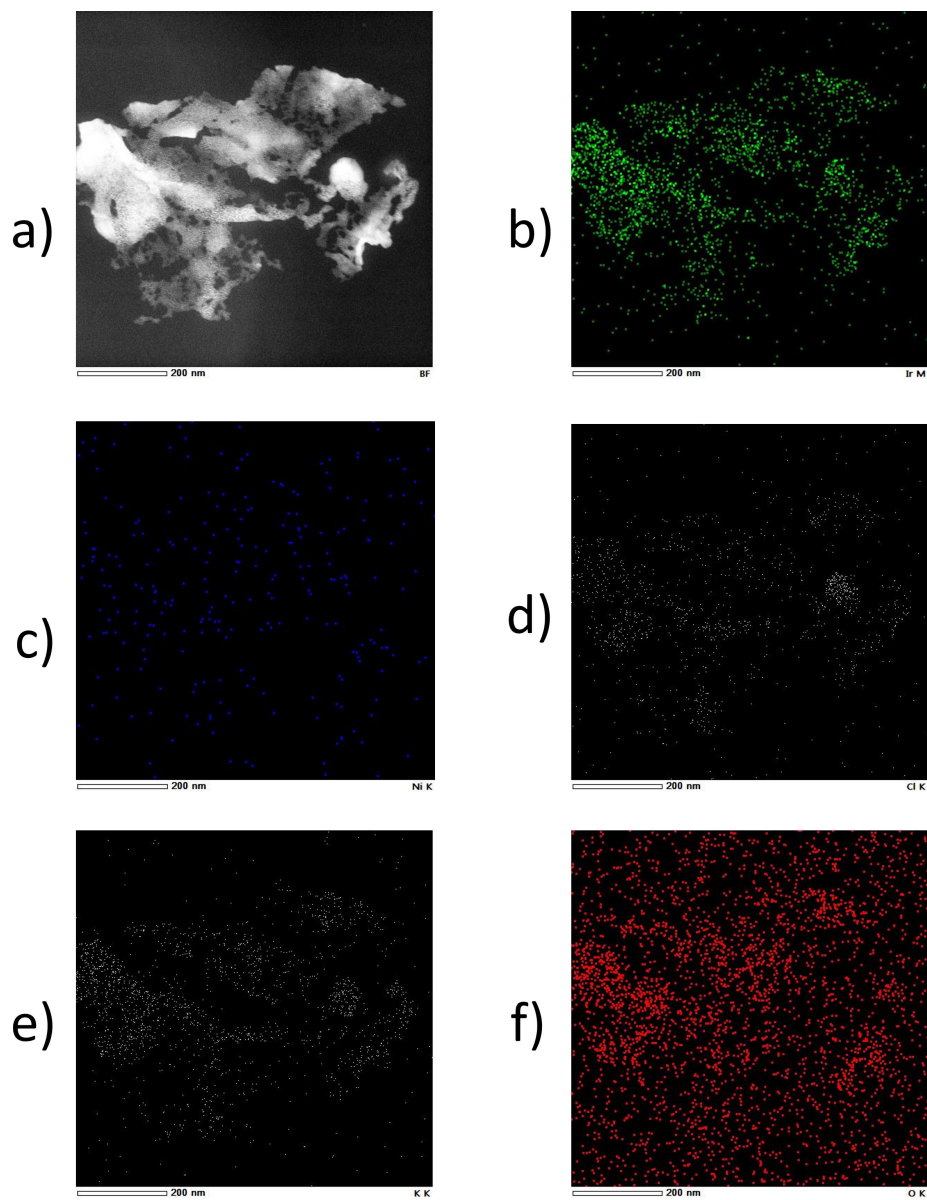


Figure 4.1: TEM/EDX results for Ir_8NiO_x batch 1 at a 200 nm scale. a) TEM image, b) Ir, c) Ni, d) Cl, e) K, f) O

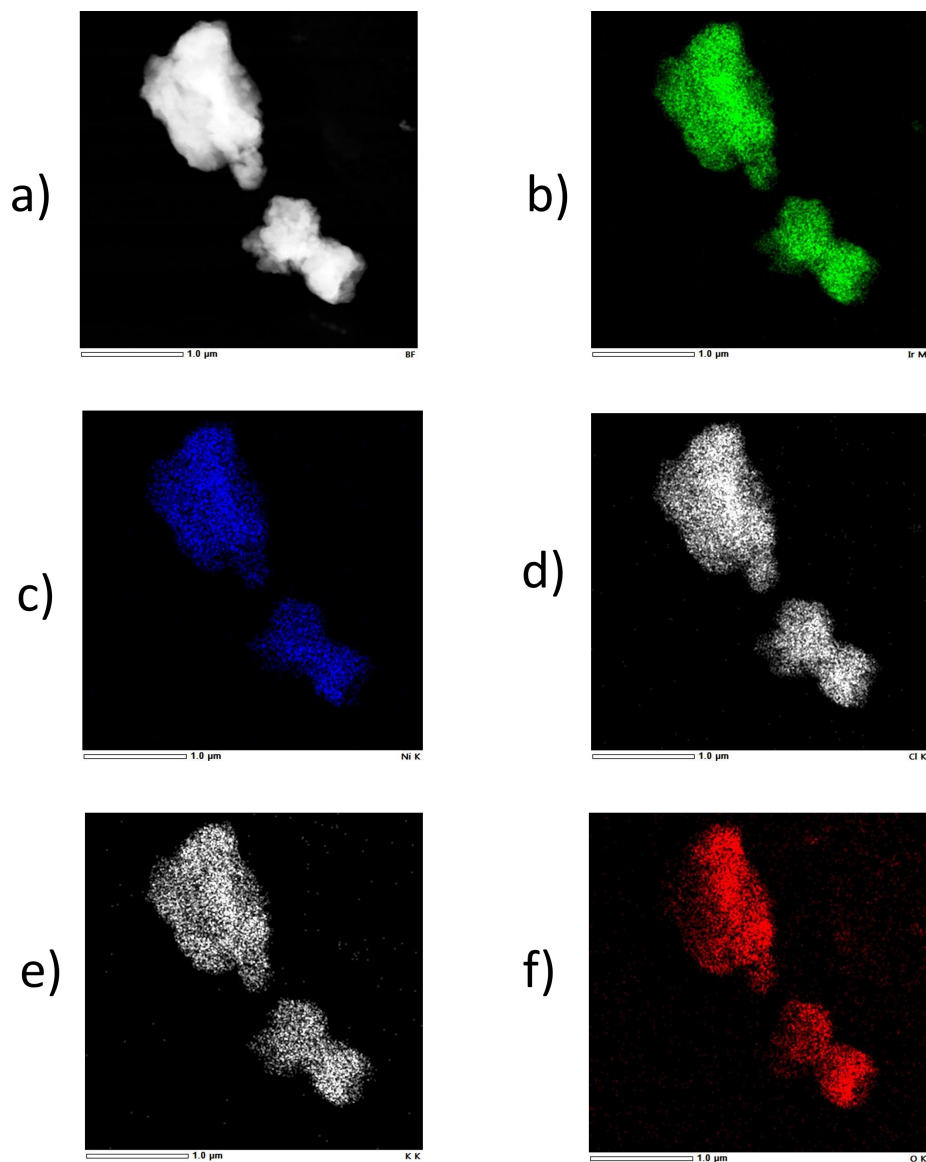


Figure 4.2: TEM/EDX results for Ir_8NiO_x batch 2 at a $1 \mu\text{m}$ scale. a) TEM image, b) Ir, c) Ni, d) Cl, e) K, f) O

Table 4.1: Elementary composition of Ir_8NiO_x catalyst found by EDX for batches 1 and 2.

Element	(keV)	Mass%		Sigma		Atom%	
		Batch 1	Batch 2	Batch 1	Batch 2	Batch 1	Batch 2
O K (Ref.)	0.525	29.27	7.35	0.89	0.1	69.4	33.1
Cl K*	2.621	7.33	11.36	0.47	0.13	7.85	23.08
K K*	3.312	13.23	5.32	0.64	0.09	12.84	9.81
Ni K	7.471	0.03	6.5	0.13	0.13	0.02	7.97
Ir M	1.977	50.14	69.47	2.18	0.56	9.9	26.04
Total		100	100			100	100

An idea of the precipitated aggregate particle size was found, but to get a look at the initial particle size of the catalyst in solution, DLS was done on a sample of the catalyst dispersed in water (magnetically stirred at 700 rpm for 10 min, bath sonicated for 30 min and degassed for 15 min before DLS tests). The particle size distributions obtained by DLS are shown in Figures 4.3 and 4.4 for batch 1 and batch 2, respectively. The resulting average hydrodynamic diameter for batch 1 was 340.6 ± 19.4 nm with a polydispersity of 26.3%. Runs 1 to 10 occurred one after another and over time trended downward from 362.9 to 312.6 nm. The decrease in particle size over the ten runs could be due to good stability or to larger particles settling over that time period. Batch 2 had an average hydrodynamic diameter of 322.1 ± 41.1 nm with a polydispersity of 25.0%. For batch 2 the hydrodynamic diameter trended upwards from run 1 to run 6 (292.8 to 400.8 nm) and then fell back down to just below the run 1 value by run 10 (280.6 nm). The increase and subsequent decrease in particle size for batch 2 could indicate that the colloid is unstable as particles agglomerate up to a larger size and then settle out, leaving smaller particles to be detected. Although the average particle size is similar between batches, the curves for each run overlap less in batch 2 which could also be a sign of increased particle agglomeration. Batch 2 will be looked at in more depth in section 4.6 at the end of the chapter.

The particle size found using DLS, ≈ 300 -400 nm, show much smaller particles sizes than that found using TEM, ≈ 800 -1800 nm. This could be due to two factors. First, only three particles were measured using TEM whereas DLS covers a much larger area, so the DLS is likely to be more accurate at assessing the overall average size of the catalyst. In addition, since DLS is performed with the catalyst suspended in solution, it is more representative of the state the particles will be in when in an ink. Secondly, before DLS was performed, the catalyst solution was prepared by magnetically stirring at 700 rpm for 10 min, bath sonicating for 30 min, and degassing for 15 min. The stirring and sonication can break up agglomerates which can result in a lower measured particle size as seen here.

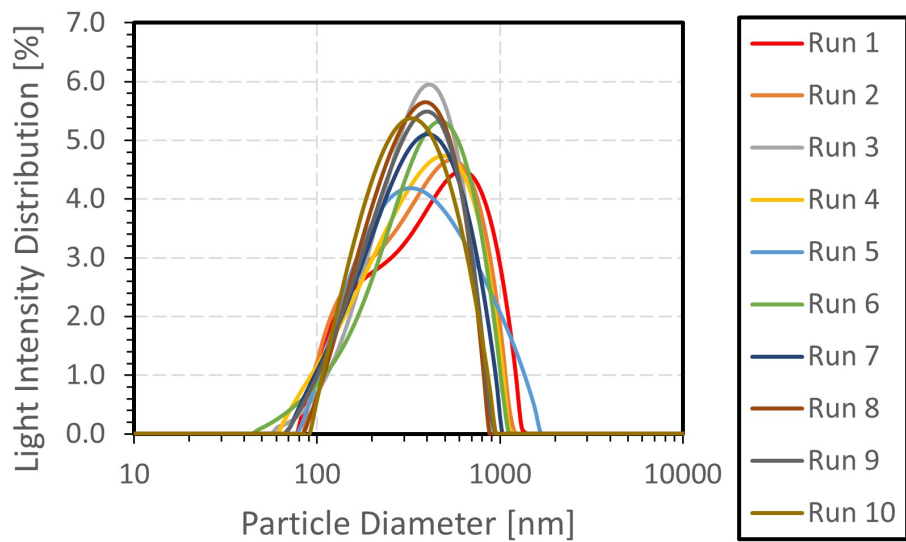


Figure 4.3: DLS light intensity distribution for Ir_8NiO_x from batch 1 in water.

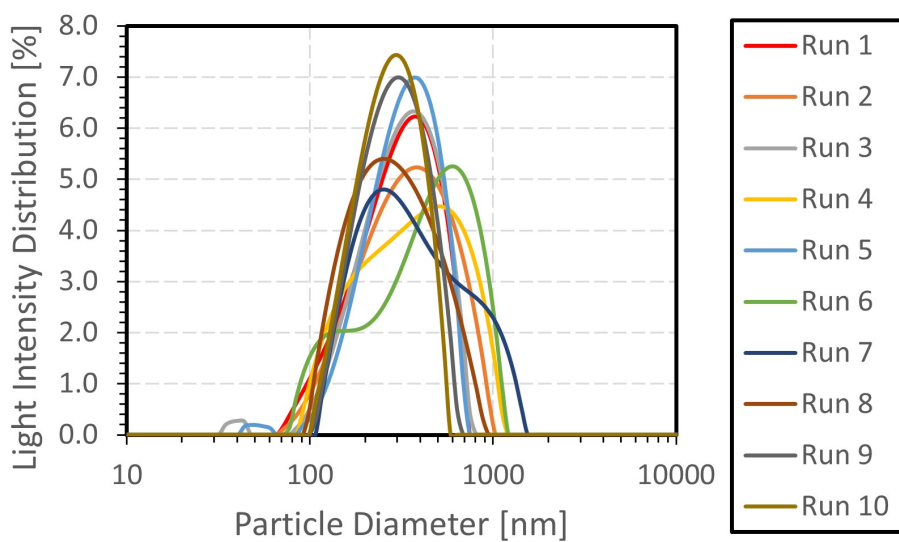


Figure 4.4: DLS light intensity distribution for Ir_8NiO_x from batch 2 in water.

4.2 Ink Characterization

Using the first batch of Ir_8NiO_x catalyst powder, a catalyst ink was developed using the recipe given in section 2.2.1 following the process outlined by Manas et. al. [28]. The composition was altered from Mandal's work as the IPA was replaced by DI water and the ratio of PG to solvent was changed to about 2.33. The change of solvent from IPA to water is due to the Ir_8NiO_x dispersing better in water. The ratio of PG to water was optimized based on data from Khattab et. al. [111]. This Ir_8NiO_x ink was found to have a density of 1.003 mg/cm^3 , viscosity of $6.85 \text{ mPa}\cdot\text{s}$, theoretical surface tension of 47.36 mN/m , and a Z value of 4.33 using the methodology in sections 2.2.1 and 2.2.2. A Z value of 4.33 is in the range of usability of the Samba cartridge. Since the surface tension was not experimentally measured, it was interpolated from Khattab's work [111].

The particle size distribution graph found by DLS is shown in Figure 4.5. The average hydrodynamic diameter and polydispersity are $385.5 \pm 35.44 \text{ nm}$ and $27.3\% \pm 3.7\%$, respectively. There was no distinct trend over time during the runs as the particle diameter began at 411.7 nm , peaked at run 6 at 448.3 nm , was the lowest at 334.7 nm in run 8 and finally returning to close to the start at 409.5 nm in run 10. Although the hydrodynamic diameter isn't below the ideal 200 nm for the Samba cartridge, the majority of the particles are below 1000 nm which indicates that the ink might be viable for printing without significant clogging. This recipe was used to print the four CCMs shown in Table 4.2.

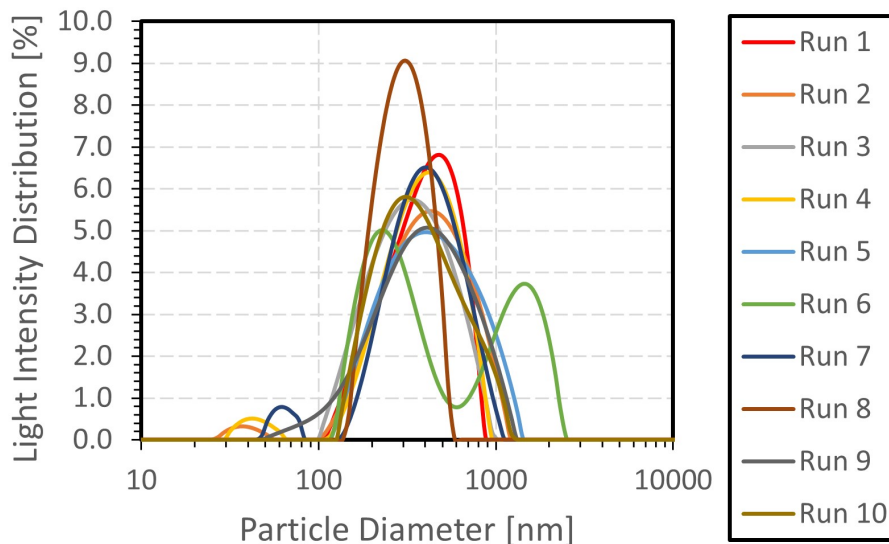


Figure 4.5: DLS light sensitivity distribution for Ir_8NiO_x ink with 2.33 PG:water mass ratio.

Table 4.2: Ir_8NiO_x CCMs printed for electrochemical and ex situ testing using the Samba cartridges.

Cell	Anode Ir_8NiO_x Loading (mg/cm^2)	No. Ir_8NiO_x Layers	Cathode Pt Loading (mg/cm^2)	No. Pt/C Layers)
E1-E2	0.99	31	0.09807	9
E5-E6	1.005	20	0.1046	10

4.3 Initial Ex Situ Characterization

Figures 4.6 and 4.7 show optical microscopy at 20x and 80x magnification, respectively of Ir_8NiO_x and IrO_x TKK catalyst layer surfaces. The primary difference in these images is the colour. One reason is that the Ir_8NiO_x when dried on the CCM became a green-brown colour. A brighter image can be produced if the layer is thinner allowing more light to penetrate it. In this case the Ir_8NiO_x is thinner than the IrO_x TKK which can be observed more clearly in Figure 4.8. Another possibility is that the exposure is much higher for the Ir_8NiO_x case, causing it to be brighter. The IrO_x TKK images are black with only some texture being revealed as these are primarily very uniform layers. The Ir_8NiO_x is less uniform as it has dark spots which may represent areas

where the catalyst has agglomerated during the drying process.

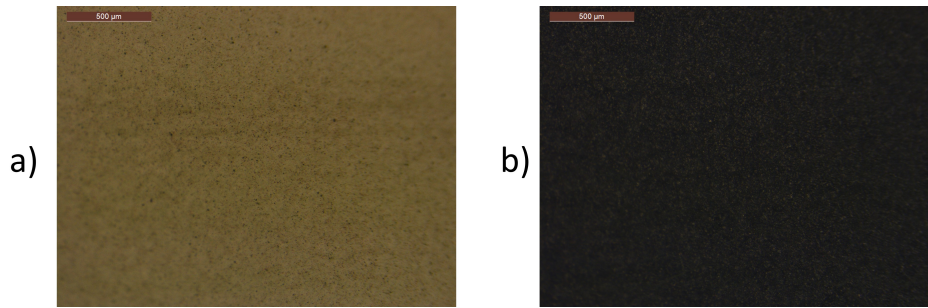


Figure 4.6: Optical microscope images at 20x magnification of a) E1, 0.99 mg/cm² Ir₈NiO_x and b) ML23, 1.007 mg/cm² IrO_x TKK

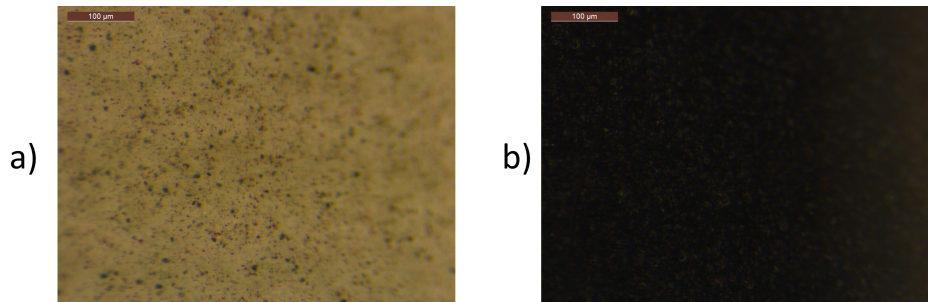


Figure 4.7: Optical microscope images at 80x magnification of a) E1, 0.99 mg/cm² Ir₈NiO_x and b) ML23, 1.007 mg/cm² IrO_x TKK

Figure 4.8 shows three cross sections of both an Ir₈NiO_x (E2) and IrO_x TKK layer (ML19). The Ir₈NiO_x layer has an average thickness of 3.46 ± 0.37 μm compared to the IrO_x thickness of 5.46 ± 0.80 μm.

Using equations 2.7-2.10 the porosity was calculated to be 27.8% and 54.1% for the Ir₈NiO_x and IrO_x TKK layer, respectively. For better performance of an electrolyzer cell, a higher porosity is desired to improve the transport of fluids throughout the catalyst layer [30]. Based on the lower porosity of the Ir₈NiO_x it is possible that large transport losses could reduce the previously shown improvement caused by combining Ir and Ni [67].

For the Ir₈NiO_x samples EDX was performed on the catalyst layer surface to look at the elemental composition. Table 4.3 shows the elemental composition, found using a ZAF corrective algorithm, for the surface in Figure 4.9. The spectra is given in the Appendix. The Fluorine, Sulphur and Carbon can

be attributed to the Nafion in the catalyst layer as the electron beam does not penetrate more than about 2 μm in depth [112]. The large relative errors of C and F (>10%) are likely due to their low atomic number which EDX is known to have difficulty detecting accurately [112]. The Ir_8NiO_x :Nafion mass ratio is 3:1 but if the mass percentage of all the components exclusive to Nafion (F, S, C) in Table 4.3 are added up, the Ir_8NiO_x :Nafion ratio is about 1:4. This is the opposite of what is expected. This could be due to a Nafion layer forming at the surface which would cause the Nafion signal to be larger. Otherwise it is unknown why the components of Nafion have such a large mass percentage.

The composition in Table 4.3 provides an Ir:Ni ratio of 16.8:1 which is not consistent with the results from the TEM imaging of Batch 1 of catalyst where the Ir:Ni ratio was 495:1. The difference between the TEM/EDX and SEM/EDX may be due to only measuring one particle from Batch 1 using TEM/EDX, so the EDX results using SEM/EDX may be more informative of the catalyst layer composition. The Ir:Ni ratio in the CCM is 16.8:1 instead of the expected 8:1 in the article [67]. The >10% relative error in the Ni measurement may suggest that there is too little Ni to accurately detect. In addition there is still evidence of contamination of the catalyst layer with K and Cl. Both the high Ir:Ni ratio and the contamination are factors that could detract from the overall cell performance.

Even though the ratio of Ir to Ni is much higher than is expected, it is still an important step to test lab synthesized catalysts by different methods which could still provide improved performance in an MEA to explore the performance and state of the catalyst layer after testing. This will again show why using an MEA is important for stepping towards commercialization and confirm what parameters are important to optimize for an MEA compared to an RDE. This difference will help catalyst synthesizers to try and fabricate catalysts with properties more suitable for the MEA environment rather than just RDE.

a)



b)

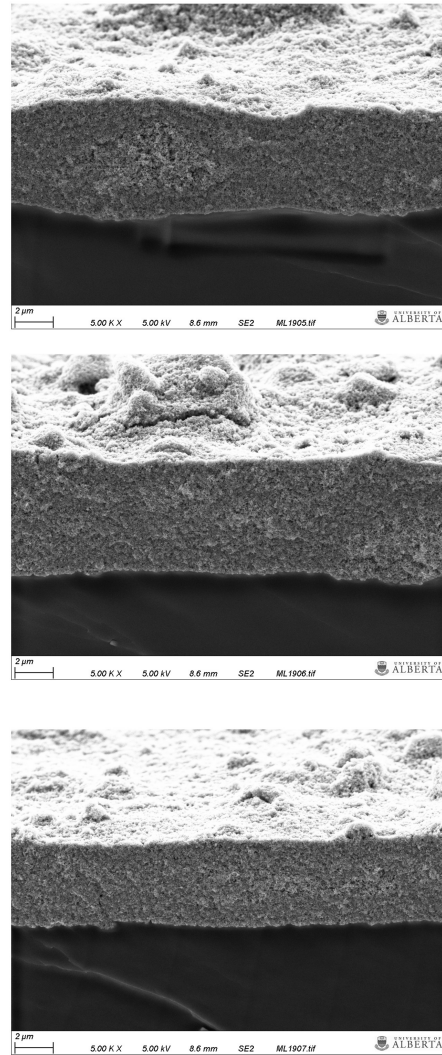


Figure 4.8: SEM images at 5000x magnification before testing of a) E2, Ir_8NiO_x 0.99 mg/cm^2 , b) ML19, IrO_x TTK 0.993 mg/cm^2 where the vertical direction displays the 3 cross sections used to estimate the thickness of each catalyst layer.

Table 4.3: EDX elemental composition of Ir_8NiO_x before testing (CCM E2).

Element	Line s.	Mass Norm. (%)	Atom (%)	rel. error (%) (1 sigma)
Hydrogen		0.00	0.00	10.00
Carbon	K-Serie	19.14	31.46	14.30
Oxygen	K-Serie	11.85	14.61	14.08
Fluorine	K-Serie	46.10	47.90	11.75
Sulfur	K-Serie	1.69	1.04	5.39
Chlorine	K-Serie	4.64	2.58	4.03
Potassium	K-Serie	1.58	0.80	5.17
Nickel	K-Serie	0.26	0.09	18.16
Iridium	M-Serie	14.74	1.51	4.14
Total		100	100	

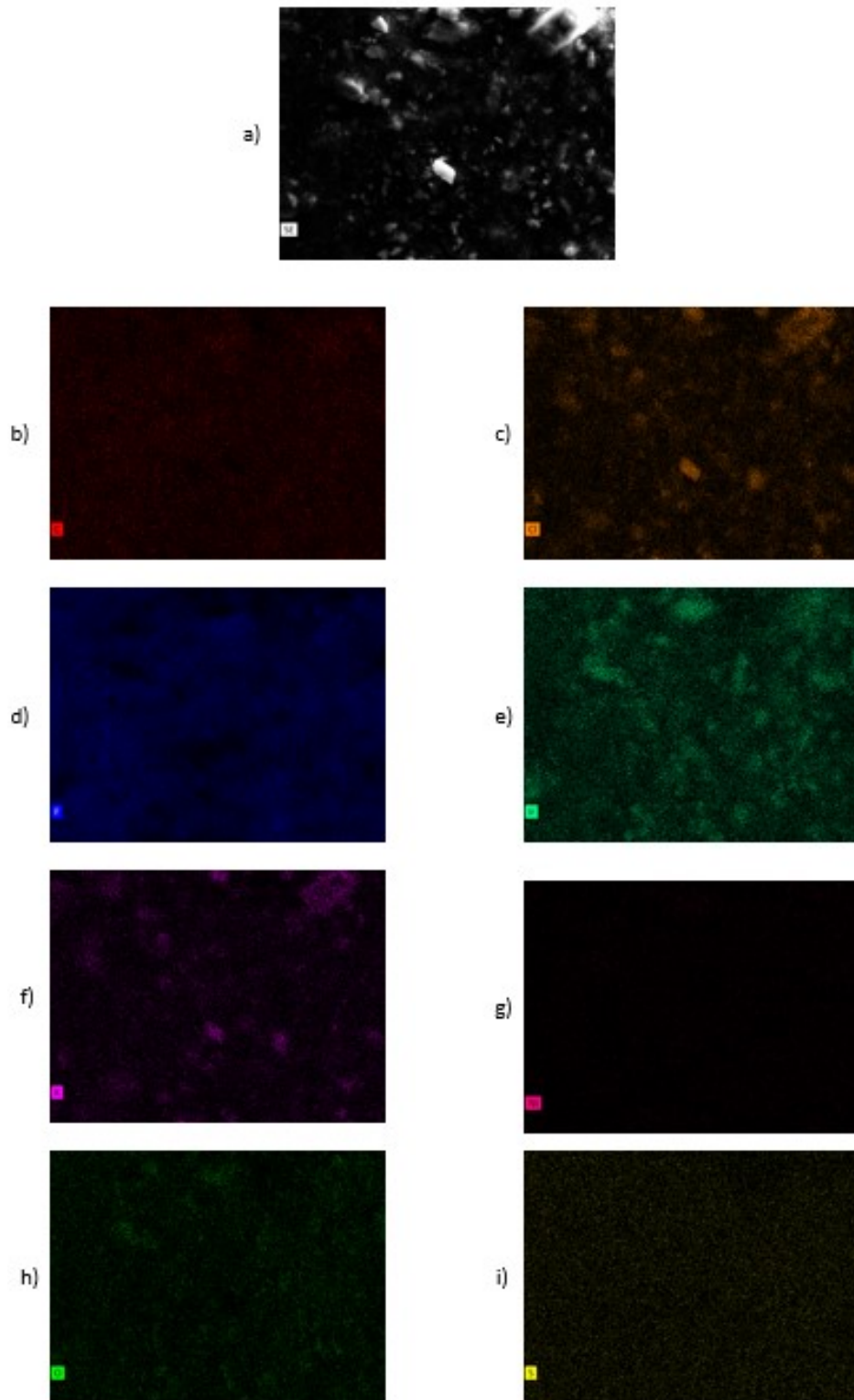


Figure 4.9: EDX of Ir_8NiO_x CCM E2 at 2000x magnification. a) SEM image, b) C, c) Cl, d) F, e) Ir, f) K, g) Ni, h) O, i) S.

4.4 Electrochemical Characterization

4.4.1 Conditioning

As described in the methodology section, the first Ir_8NiO_x CCM tested, E1, was conditioned using the same protocol as the IrO_x TKK samples; however, the protocol resulted in very large cell voltage (>2 V) that it was hypothesized to damage the electrode. Therefore, for subsequent Ir_8NiO_x CCMs the maximum current density of the conditioning procedure was decreased from 2 to 0.8 A/cm^2 to try and preserve some performance and stability. Figure 4.10 shows the cell voltage over time during conditioning with each step being an increase in the current density. The difference between the IrO_x and Ir_8NiO_x cells is about 100 mV at low current densities but quickly rises to 200-800 mV by 0.8 - 1 and 2 A/cm^2 , respectively. The initial stability of the cell can be seen by comparing any increase in voltage during a given current step. The IrO_x cells do not have a significant increase over time for all current densities showing they are stable, whereas the Ir_8NiO_x cells are only stable up to 0.2 A/cm^2 . At 0.8 - 1 A/cm^2 the Ir_8NiO_x cells have an initial peak and then the voltage stabilizes but when run at 2 A/cm^2 the voltage decreases to 2.042 V after 7 mins 17 seconds and then begins to increase to a final voltage of 2.157 V . Within the last 13 minutes of the test the cell degrades by more than 100 mV (7.69 mV/min). As stated above this is why the conditioning protocol was changed for the Ir_8NiO_x cells as this suggests that the layer is damaged at high voltages as will be seen in later sections.

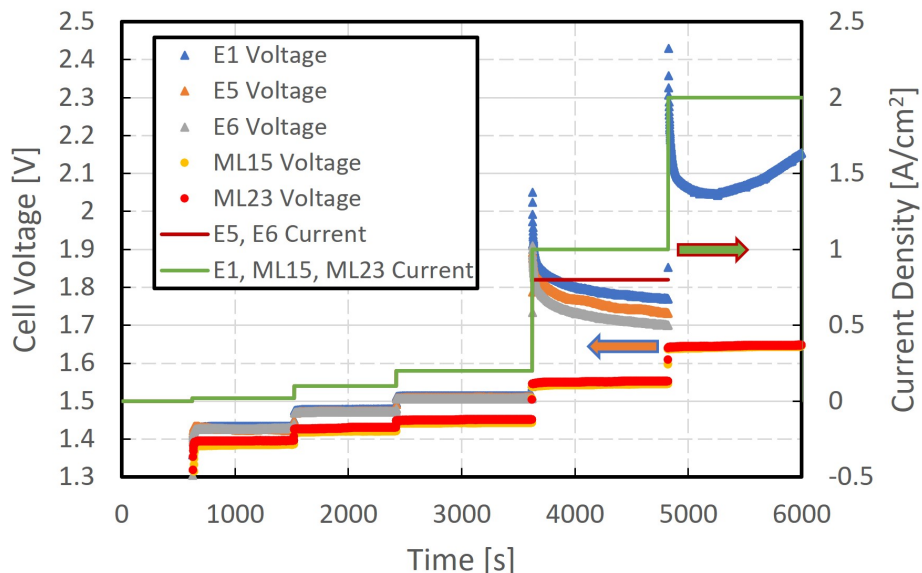


Figure 4.10: Conditioning curves over time for each of the three tested Ir_8NiO_x cells and the two tested IrO_x cells. All cells have the same current steps up until the 4th current step at 0.2 A which changes to 1 A for E1, ML15 and ML23 and 0.8 A for E5 and E6.

4.4.2 Cyclic Voltammetry

To determine how well the catalyst is being utilized and how this utilization changes due to running the cell, cyclic voltammetry was run before and after the pol. curves and it is shown in Figure 4.11. The ECSA and double layer capacitance (C_{dl}) for each cell was found using equation 2.12 and 1.12, respectively, and is shown in Table 4.4 along with the thickness and porosity.

Figure 4.11 shows there is negligible Pt H_{UPD} . There are two peaks that correspond to Ir(III) to Ir(IV) and Ir(IV) to Ir(V) oxidations of the catalyst at about 0.8 and 1.2 V, respectively. Typically metallic Ir only has one peak and contains some Pt H_{UPD} whereas IrO_x has 2 peaks and negligible Pt H_{UPD} [106]. This suggests that the Ir_8NiO_x catalyst is closer to being an amorphous oxide rather than a metallic IrNi.

An alternative explanation for the two peaks could be that the first peak would remain for Ir(III) to Ir(IV) oxidation but the second peak could be Ni(II) to Ni(III). Lee et. al. [85] found that Ni(II) to Ni(III) happens between 1.2 and 1.3 V but only for the case in alkaline media. Since this work is in

acidic media and the catalyst layer contains a small amount of Ni it is much more likely that the second peak is dominated by the Ir(IV) to Ir(V) oxidation.

Table 4.4 shows that all of the Ir_8NiO_x cells decreased their ECSA after acquiring the pol. curves, which could indicate degradation or restructuring of the catalyst later. This can also be seen in IrO_x cell ML15. It is common to have some loss over the course of testing. Cell ML23 is similar before and after suggesting that its structure is mostly stable.

The Ir_8NiO_x cells have 6-23x lower ECSA than the IrO_x cells. There are 3 reasons for this trend. The first is that the catalyst sites are not as accessible which could be due to the Ir_8NiO_x cells having a porosity 1.9x less than the IrO_x cells. Lower porosity increases the packing of the catalyst particles which leaves less space for reactions to occur. Secondly, the Ir_8NiO_x catalyst may have lower surface area than the commercial IrO_x . This would need to be verified by BET measurements which were not performed in this work. Lastly, lower Ir_8NiO_x ECSA could also be due to non-uniformity of the catalyst layer as seen in Figure 4.7 and catalyst layer degradation in the form of detachment from the membrane which could have occurred during conditioning or pol. curves.

The double layer capacitance of Ir_8NiO_x cells is also 30-78 mF (1.32-2.05x) lower than that of IrO_x . This provides a similar result to that of the ECSA that there is less capacitive charging meaning there is less area for reactions to occur. It has also been found that the double layer capacitance is a good indicator of the proportional difference in ECSA for a given layer [106].

In order to increase the number of active sites, one could decrease particle size [113], increase particle or catalyst layer roughness [114], or increase catalyst layer porosity [30] which are illustrated in Figure 4.12. Particle size can be decreased by changing the ink composition which can determine particle aggregation due to the effects of different solvents and additives [113]. Using dispersion or grinding techniques such as bath and probe sonication, ball milling, and stirring time can also effect the particle size (See section 4.6). The roughness of the particle or catalyst layer is also influenced by the ink composition as well as deposition method [114]. Increased porosity can be

achieved by either adding a support or carbon can be used as a pore former as described by Mandal et. al. [30]. In his work the carbon was added to the catalyst ink, which will corrode to CO_2 during cell operation, resulting in increased porosity of the final Ir (Umicore) catalyst layer by 19% and the ECSA by 31.6%. Using a support could also help reduce particle size and improve the porosity of the layer by providing larger particles which will force larger gaps to appear between particles. Supports currently being tested in PEMWE are ATO, ITO, and FTO as they are able to resist oxidation while providing electrical conductivity and stability [109].

Improving the porosity will also increase the thickness of the layer causing the charge transport resistance of the layer to increase, adding to cell losses. This was shown by Mandal [106] when comparing the use of pore former with Ir from Umicore having high electrical conductivity and IrO_x TKK with low electrical conductivity. As stated above when the porosity of the layers increased the performance of the Ir (Umicore) cells increased whereas for the IrO_x TKK cells had an increase in the kinetic region at low current densities and a decreased performance at higher current densities due to the increased electron transport losses.

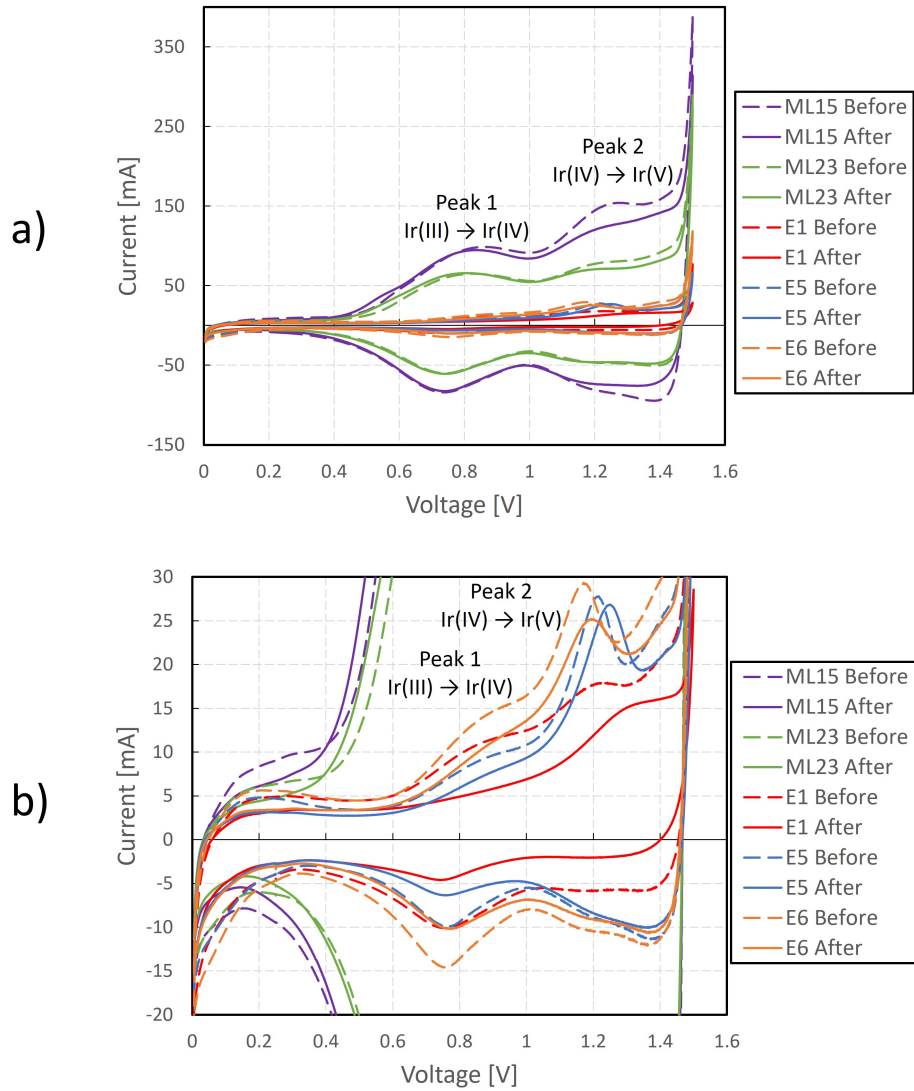


Figure 4.11: CVs of the three Ir_8NiO_x cells (E1, E5, E6) and two IrO_x cells (ML15, ML23) before and after doing the polarization curves. a) Entire graph, b) Zoomed in on the Ir_8NiO_x curves for a better view.

Table 4.4: Calculated ECSA before and after pol. curves for the tested Ir_8NiO_x and IrO_x cells to compare ECSA and double layer capacitance with thickness and porosity.

*For E5-E6 the values were assumed to be similar to that of E1.

Cell	Anode Loading (mg/cm^2)	Layer Thickness (μm)	Porosity (%)	ECSA Before ($\text{m}^2/\text{g}_{\text{cat}}$)	C_{dl} Before (mF/cm^2)	ECSA After ($\text{m}^2/\text{g}_{\text{cat}}$)	C_{dl} After (mF/cm^2)
E1	0.99	3.46	27.8	5.28	23.62	2.58	14.98
E5	1.005	$\approx 3.46^*$	$\approx 27.8^*$	6.00	23.95	5.28	15.53
E6	1.005	$\approx 3.46^*$	$\approx 27.8^*$	8.22	28.03	7.10	16.70
ML15	1.064	5.51	50.7	63.01	41.77	59.26	30.64
ML23	1.007	5.20	50.7	40.83	29.97	41.27	22.02

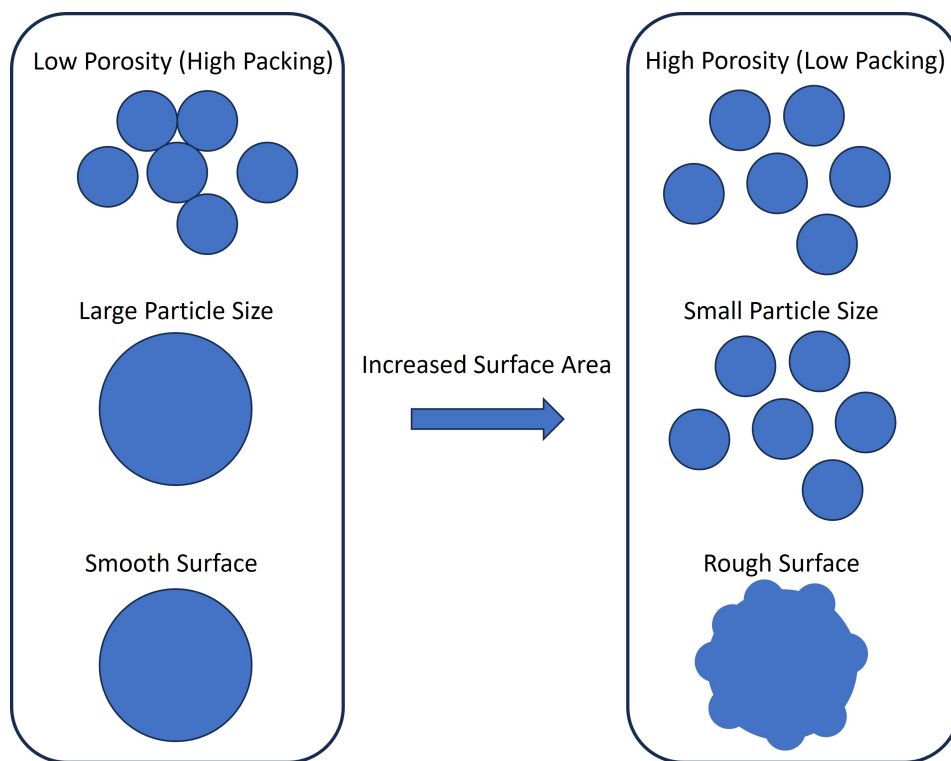


Figure 4.12: Methods of increasing the surface area of the catalyst particles/agglomerates and the catalyst layer.

4.4.3 Polarization Curves

Figures 4.13 and 4.14 show the initial pol. curves along with the iR -free curves for E1 and, E6 and E5, respectively. iR -free curves are found when the ohmic losses are removed. The pol. curves of the two IrO_x cells, ML15 and ML23 are given for comparison. Since some of the Ir_8NiO_x cell pol. curves changed considerably between runs, each consecutive test is shown.

Figure 4.13 shows a much worse performance for Ir_8NiO_x than the state-of-the-art catalyst as the cell voltage is higher at all current densities even without the ohmic component. This is especially true at high current density where the difference is about 900 mV at 4 A/cm^2 . All of the runs for E1 have hysteresis with Run 1 having the largest increase in voltage on the backwards sweep. Runs 2 and 3 for E1 reach 2 V before 1 A/cm^2 indicating significant degradation from the initial run. This confirms that going to high current densities is not feasible with this catalyst in its current state as it appears

to have significant mass transport losses which begin around 1.5 A/cm^2 and increase after 3 A/cm^2 . The hysteresis shows large kinetic losses accumulating after the first run. Kinetic losses could be due to the catalyst dissolving off the surface or from a build up of oxygen bubbles which eliminate access to active sites.

In addition to conditioning E5 and E6 differently, for the pol. curves the current density was varied up to a maximum of 2 A/cm^2 . E5 has three pol. curves going from 0-1.2, 0-1.6 and 0-2 A/cm^2 whereas E6 started with three pol. curves from 0-1.2 A/cm^2 and finished with a 0-2 A/cm^2 curve. Figure 4.14 shows that when the potential and current are kept low (below 2 A/cm^2) hysteresis is reduced. It is speculated that the reason for the hysteresis being reduced is that bubbles forming at the surface are not being removed fast enough at high current densities causing increased losses on backwards sweeps and subsequent runs that go above 2 A/cm^2 as seen with cell E1 previously. The low porosity of the catalyst layer could be the cause of the hysteresis effect if bubbles are trapped in the only available pores or if bubbles created within the layer can't escape and then force their way out causing damage to the layer.

Cell E6 showed repeatability at low current densities below 1.2 A/cm^2 . Above 1.2 A/cm^2 E5 Run 2 and Run 3 are higher than E6 Run 4 with a 100 mV gap at 2 A/cm^2 . The deviation is likely due to the higher current density run in E5 Run 2 (0-1.6 A/cm^2) compared to E6 Run 3 (0-1.2 A/cm^2).

The Ir_8NiO_x cells also suffer from losses in the ohmic region which is shown by the increased slope compared to the IrO_x cells.

Overall these results make sense given the low ECSA and large slope of each Ir_8NiO_x cell. Since the ECSA for the Ir_8NiO_x catalyst layers is low there is less catalyst utilization and a higher voltage will be required to achieve the same current as the IrO_x which has a higher ECSA.

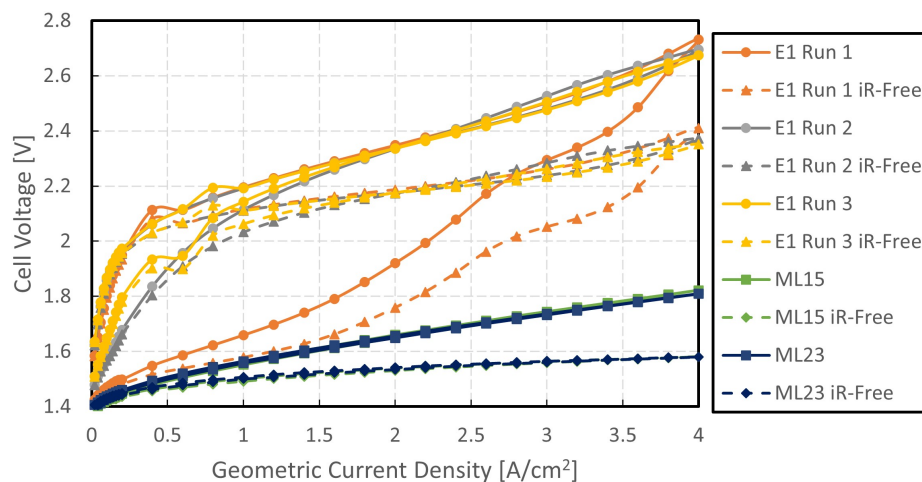


Figure 4.13: E1 0.99 mg/cm² polarization curves compared to IrO_x cells ML15 and ML23.

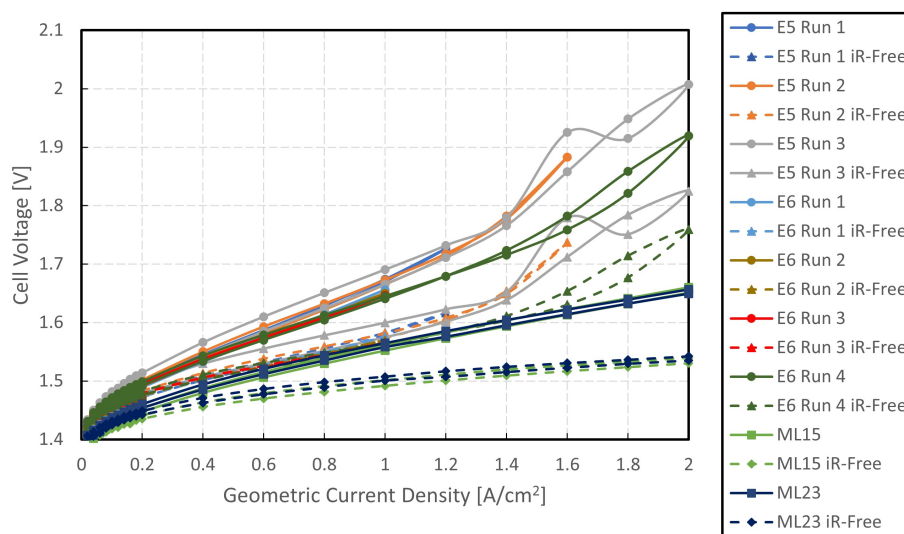


Figure 4.14: E5 and E6 1.005 mg/cm² polarization curves compared to IrO_x cells ML15 and ML23.

If the pol. curves are normalized by ECSA instead of geometric area, as shown in Figure 4.15, it was found that the performance per active site is greater for the Ir_8NiO_x cells when current density is less than 2 A/cm_{geo}^2 which reflects the trend from the initial paper [67]. Normalizing by the ECSA provides a better representation of the activity of the catalyst. The improved intrinsic activity of Ir_8NiO_x suggests that the catalyst is still performing well on an individual active site level but fails to be accessible on the larger scale. This improvement does break down for cell E1 when looking at Runs 2 and 3 as they deteriorate to be worse than the IrO_x cells which again shows that the Ir_8NiO_x catalyst layer is not stable at high current densities.

In section 4.4.2 the CVs suggest that the Ir_8NiO_x catalyst could be in an amorphous form compared to the more crystalline rutile form of IrO_2 . It has been found that amorphous structures are more active towards OER but are less stable [115]. The possible amorphous structure of the Ir_8NiO_x catalyst could also be a contributing factor to the instability at high current densities.

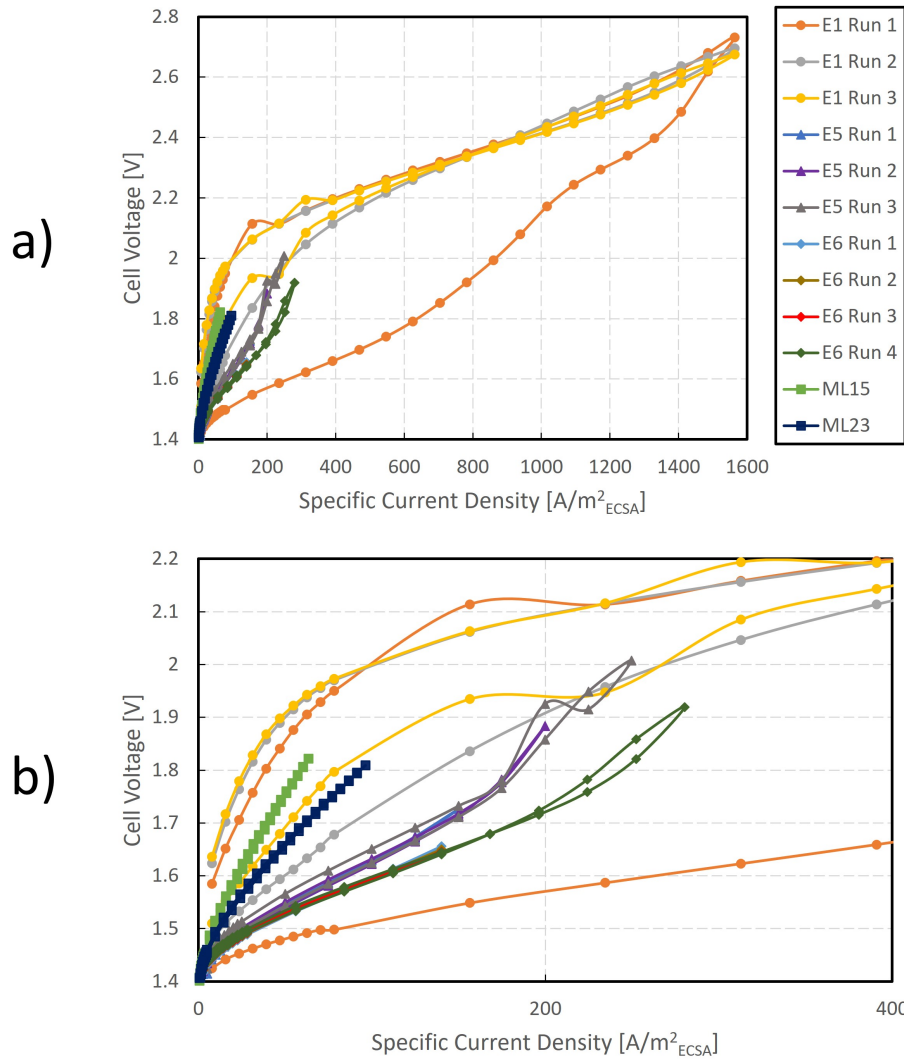


Figure 4.15: a) Pol. curves of the Ir₈NiO_x and IrO_x cells where the current is normalized by the ECSA. b) Zoomed in area for clarity at low specific current densities. Legend is the same for both a) and b).

4.4.4 Kinetic Parameters

The kinetic parameters for each cell were extracted from Butler-Volmer (B-V) plots, seen in Figure 4.16, using linear scan voltammetry data between 4-80 mA/cm² as this region was the closest to linear and similar to regions analyzed in other works using IrO_x TKK [12, 106].

Figure 4.16 does not show the typical B-V plot. An ideal B-V plot is centered around an overpotential of 0 V. The curves found in Figure 4.16 are unexpected and deserve further analysis. Perhaps modelling of the B-V equation could determine what parameters can cause of shift in the overpotential away from 0 V.

Although the graph is not ideal, the kinetic parameters of Tafel slope, current exchange density (i_0) and transfer coefficient (α) were found for each cell using Tafel analysis of the B-V curve using equation 1.10 and are given in Table 4.5.

The Tafel slope for E5 and E6 are very similar whereas E1 is about 20 mV/dec higher. Again this is likely due to the catalyst layer deterioration from the high current density pol. curves. Comparing E5 and E6 to the IrO_x cells, the Tafel slopes are only 5-7 mV/dec higher which is not a huge difference compared to ohmic and mass transport losses seen in the latter stages of the pol. curves. In addition the Ir₈NiO_x cells have larger current exchange densities by up to 2 orders of magnitude. This also demonstrates that the kinetics for the Ir₈NiO_x cells could be performing better. In literature, hydrous IrO_x has been found to have a Tafel slope of 35-50 mV/dec [12, 37, 89] and is related to the amorphous nature of the catalyst structure [116]. Mandal et. al. found that IrO₂ has a Tafel slope around 44-49 mV/dec and exchange current density on the order of 10⁻⁷ [28] but the Tafel slope has also been reported to be around 60 mV/dec for IrO₂ [116]. The values for hydrous IrO_x are similar to the ones obtained in this work. For various IrNi catalysts the Tafel slope has also been found to range from 34-150 mV/dec. The Tafel slopes of the Ir₈NiO_x cells in this work are at the lower end of this range which shows the potential for good kinetics. However, the Tafel slope is difficult to

measure as the linear region is not always obvious. Although there was an attempt to use a similar current range to previous studies of 4-80 mA/cm² [12, 28], the range that is used to find this linear region may be responsible for differences in the Tafel slope and current exchange density.

The transfer coefficient for a 1 electron transfer reaction is between 0-1 but in Table 4.5 the values of α are above 1. This is due to the OER being a 4 electron transfer reaction.

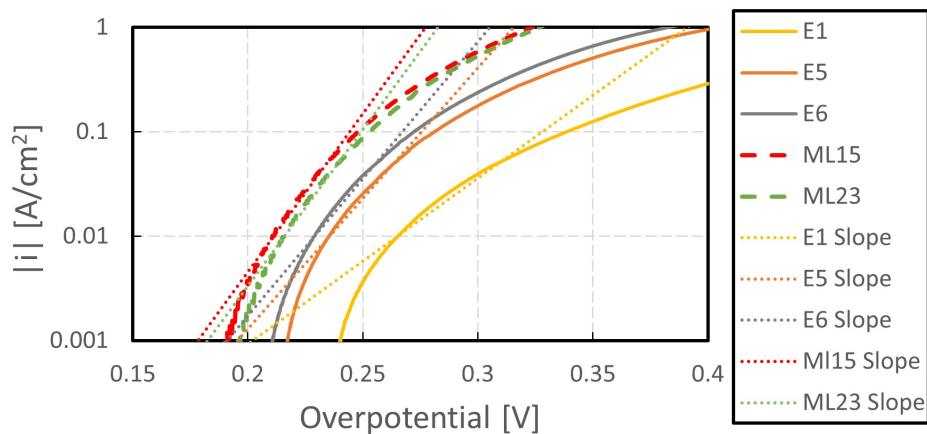


Figure 4.16: Butler-Volmer plots for E1, E5, E6, ML15 and ML23.

Table 4.5: Kinetic parameters obtained from Tafel plots for E1, E5, E6, ML15 and ML23.

Cell	i_0 (A/cm ² _{geo})	Tafel Slope (mV/dec)	α
E1	6.168E-07	62.975	1.112
E5	1.290E-08	40.003	1.751
E6	9.687E-09	38.098	1.839
ML15	3.922E-09	32.990	2.123
ML23	3.352E-09	33.357	2.100

4.4.5 Electrochemical Impedance Spectroscopy (EIS)

Figure 4.17 shows the Nyquist plot at 0.1 A of Ir_8NiO_x cells E1, E5 and E6 alongside that of IrO_x cells ML15 and ML23. The data was fit using the equivalent circuit in Figure 2.10 and the fitting parameters for the 0.1 A tests are given in Table 4.6.

Figure 4.17 shows the expected two semicircles found at low applied current which theoretically corresponds to the cathode at the first partial semicircle at low real resistance values and the anode at the second semicircle [36]. An equivalent circuit can be formed using the assumption that the cathode and anode should appear in the Nyquist plot at low current. The data is fit using the equivalent circuit shown in Figure 2.10. The Kramers-Kronig transformation can be used to determine if the data is valid which is that the system is causal, stable, linear, and time invariant [117]. It has been found that if the data fits the equivalent circuit well then it is also likely that a system follows these assumptions and is therefore valid to analyze [117]. All the curves in Figure 4.17 fit well to the equivalent circuit so the data was assumed to be valid.

Figure 4.17 shows that the Ir_8NiO_x cells have a less defined first semicircle compared to the two defined semicircles in the IrO_x curves. EIS modelling in Figure 3.24 suggests that this could be due to low capacitance in the Ir_8NiO_x catalyst layer which can also be seen by the value of C3 in Table 4.6 being at least 3x lower for Ir_8NiO_x . In addition, the double layer capacitance of the Ir_8NiO_x catalyst layers found in section 4.4.2 are half the value of the IrO_x catalyst layers further proving this point.

As stated above, typically it is proposed that the large semicircle represents the anode side while the smaller semicircle represents the cathode side. If the first semicircle is assumed to be the cathode then since both the Ir_8NiO_x and IrO_x used the same cathode, the first semicircle should remain the same. At first glance this can not be determined due to the larger semicircle for Ir_8NiO_x dominating. Using the fitted curves, Table 4.6 shows that the fitted capacitance, C2, of the Ir_8NiO_x cells is about half that of IrO_x and the charge

transfer resistance is 8-77 m Ω higher for the Ir₈NiO_x cells. This indicates that the first semicircle does not necessarily represent the cathode but possibly another process occurring at the anode. This could be a side reaction or a different part of the reaction mechanism as this may be different due to the changes in catalyst composition [118]. It has been seen that for IrO₂ that there is no first semicircle but for IrO_x it is possible to see which may again suggest that the catalyst structure is responsible for changes in the high frequency range of the Nyquist plot [106].

Another possibility for the first semicircle could be related to the double layer capacitance of the anode. Table 4.6 shows the pseudo capacitance corresponding to each CPE as well as the double layer capacitance found in the CVs previously. The values are similar when comparing the first semicircles capacitance, C2, but are very different when comparing the anode capacitance, C3, which, besides E1, is 3.5-5.5x larger for the Ir₈NiO_x cells and 11.1-12.8x larger for IrO_x. This suggests that the double layer capacitance of the anode layer is better represented by the first semicircle than the second. This could help explain the different values for the first semicircle between the catalysts. The first semicircle may be representative of the catalyst double layer charging and discharging at high frequencies and then as the frequency lowers the reaction kinetics dominate leading to the larger semicircle. Finally, as described in the previous chapter, the difference between the capacitance found from the Nyquist plots and the CVs could simply be due to different operating conditions.

The charge transfer resistance, R3, for the Ir₈NiO_x cells when compared to that of the IrO_x, is greater for E1 but is less for E5 and similar for E6. Cell E1 could have a larger charge transfer resistance due to the high current it was exposed to during conditioning and pol. curves which may have deteriorated the catalyst layer and washed Ni away leading to the difference seen between E1 and E5-E6. The reaction rate constant can be a cause for the increase of charge transfer resistance [118]. The reaction rate for E1 again may have decreased due to deterioration of the catalyst layer. E5 and E6 however are quite similar if not better than the IrO_x cells which upholds the conclusion

made in Figure 4.15, that the activity of the Ir_8NiO_x catalyst is similar or higher than the IrO_x TKK but does not have the stability to maintain it.

Figure 4.18 shows the Nyquist plots for currents of 0.1, 1 and 10 A. The charge transfer resistance (semicircle diameter) decreases with increasing current when going from 0.1-10 A for cell E3 and 0.1-1 A for E5-E6 which is to be expected as the rate of reaction increases with the increased applied current. When going to 10 A, E5 and E6 see a larger curve with an initial 45 degree line followed by a loop that curves backwards at low frequencies. The 45 degree line indicates mass transport losses occurring while the loop is difficult to attribute to a process. In fuel cells these loops have been seen and are thought to be due to side reactions or intermediate steps but it is unknown if this is the same in the case of electrolyzers [118].

The HFR is equal to R_1 in the equivalent circuit multiplied by the area of the catalyst layer with the associated HFR in Table 4.7. For each Ir_8NiO_x cell the HFR decreases, with E1 decreasing the most by $35.45 \text{ m}\Omega\cdot\text{cm}^2$ then E5 by about $10 \text{ m}\Omega\cdot\text{cm}^2$, and E6 stays about the same with an increase in applied current. E1, E5, and E6 converged to $79\text{-}82 \text{ m}\Omega\cdot\text{cm}^2$ at 1 A of applied current. IrO_x cells remained about the same regardless of the applied current. The HFR is $\approx 24\text{-}60 \text{ m}\Omega\cdot\text{cm}^2$ larger for Ir_8NiO_x cells compared to IrO_x at 0.1 A and about $18\text{-}25 \text{ m}\Omega\cdot\text{cm}^2$ larger at 1 A. HFR at 10 A was not measured due to an inability to fit the curves to the equivalent circuit.

The total performance, kinetic parameters and HFR have been found. Using these values the total performance pol. curves can be broken down into its components of kinetic, ohmic, and mass transport and other losses. Figure 4.19 shows the pol. curves for E1, E5, and E6 compared to ML15 and ML23 as well as the overpotential associated with each type of voltage loss. Kinetic curves were plotted using the Tafel equation (Equation 1.10). Ohmic losses were added to the kinetic curve by simply multiplying the value of R_1 at 0.1 A by the current and mass transport + other losses were calculated by subtracting the ohmic and kinetic losses from the total measured pol. curve. The kinetic losses are similar for both catalysts whereas the ohmic losses and especially the mass transport + other losses are more severe at $2 \text{ A}/\text{cm}^2$ and

are more pronounced as the current density increases for E1. Since the cell assembly is identical besides the catalyst layers, the Ir_8NiO_x catalyst layers should be the cause of the increased ohmic resistance. Since the HFR measures the most conductive phase in the catalyst layer it is possible that the protonic conductivity of the Ir_8NiO_x catalyst layers is causing the increased ohmic losses if it is assumed that the electronic conductivity is poor [29]. Mass transport losses are likely due to the low porosity of the Ir_8NiO_x catalyst layers. Both improvements in structure and testing different amounts of Nafion added to the Ir_8NiO_x ink are required to improve the cell performance.

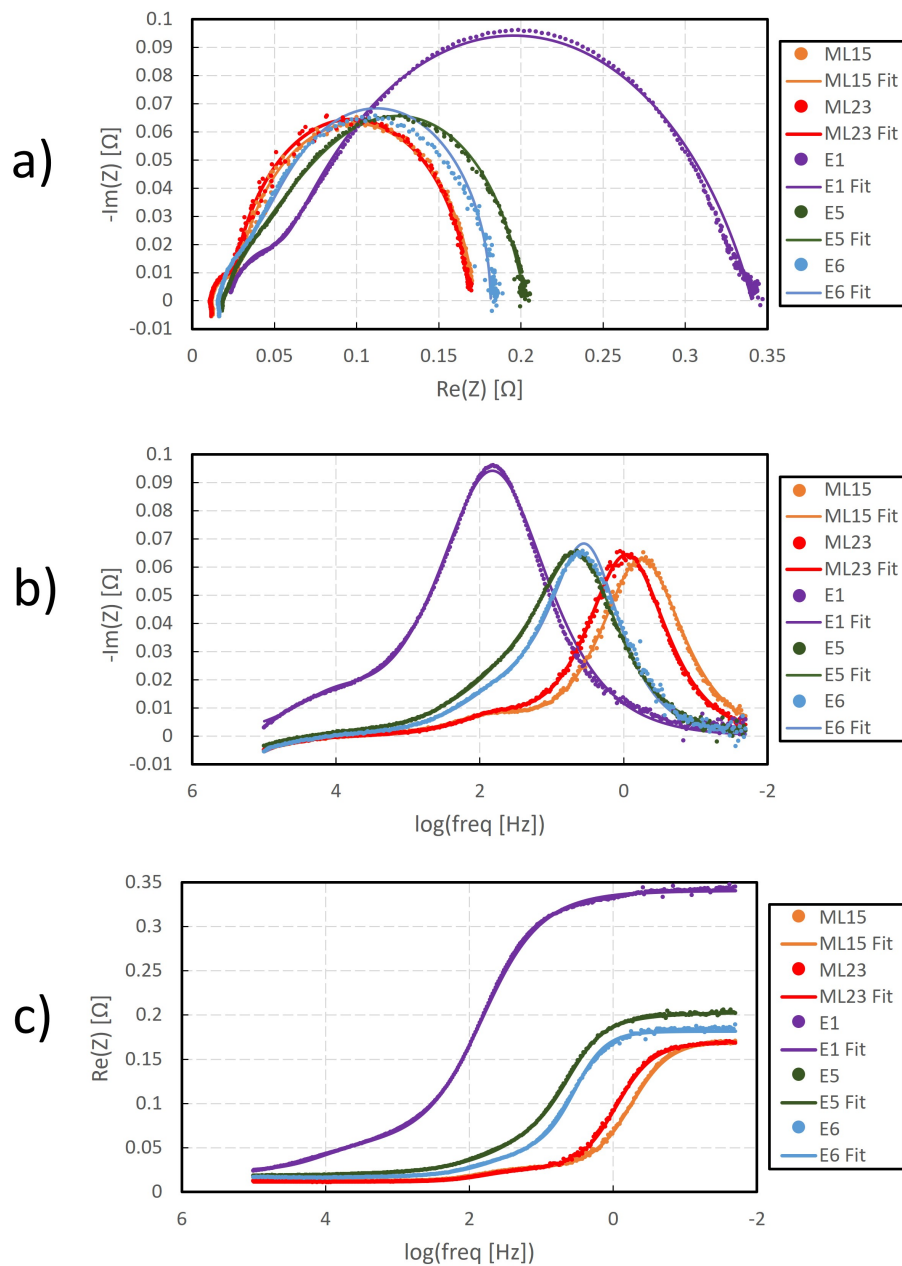


Figure 4.17: Plots from EIS tests for Ir_8NiO_x (E1, E5, E6) and IrO_x TKK (ML15, ML23) at 0.1 A. a) Nyquist Plot, b) $-\text{Im}(Z)$ vs $\log(\text{freq})$, c) $\text{Re}(Z)$ vs $\log(\text{freq})$. b) and c) are used to show relation to frequency so all data is present.

Table 4.6: Fitting parameter values for EIS performed at 0.1 A along with the pseudo capacitance related to each respective CPE and the double layer capacitance from the previous CVs.

Cell	Loading (mg/cm ²)	L1 (H)	R1 (Ω)	Q2 (F.s ^{a-1})	a2	R2 (Ω)	Q3 (F.s ^{a-1})	a3	R3 (Ω)	Pseudo C2 (mF/cm ²)	Pseudo C3 (mF/cm ²)	Cdl (mF/cm ²)
E1	0.99	0	0.023	0.003	0.845	0.029	0.041	0.734	0.289	0.096	1.657	14.983
E5	1.005	6.49E-09	0.018	0.675	0.613	0.091	0.447	0.984	0.094	23.261	84.981	15.528
E6	1.005	9.12E-09	0.016	0.255	0.829	0.022	0.393	0.910	0.146	17.503	59.152	16.788
ML15	1.064	9.12E-09	0.012	0.278	0.900	0.015	2.193	0.910	0.145	30.266	391.505	30.648
ML23	1.007	8.86E-09	0.011	0.330	0.896	0.014	1.384	0.929	0.143	35.300	244.574	22.017

Table 4.7: HFR of Ir₈NiO_x and the IrO_x cells.

Cell	HFR (m Ω ·cm ²)		
	at 0.1 A	at 1 A	at 10 A
E1	116.70	82.25	-
E5	91.25	82.10	-
E6	80.85	79.10	-
ML15	60.25	60.15	60.65
ML23	57.20	56.75	56.45

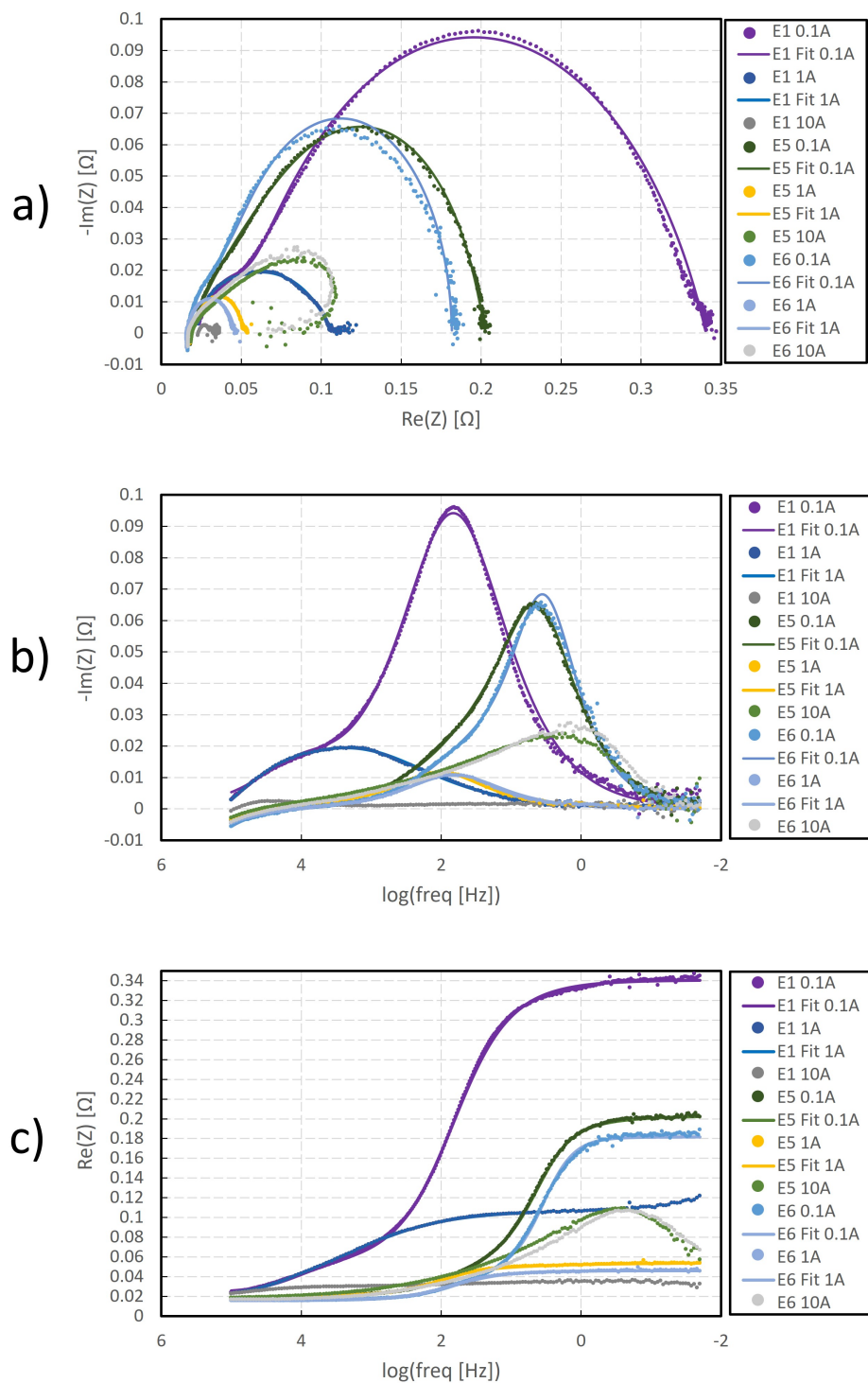


Figure 4.18: EIS curves for Ir_8NiO_x (E1, E5, E6) at 0.1, 1 and 10 A. a) Nyquist Plot, b) $-\text{Im}(Z)$ vs $\log(\text{freq})$, c) $\text{Re}(Z)$ vs $\log(\text{freq})$. b) and c) are used to show relation to frequency so all data is present.

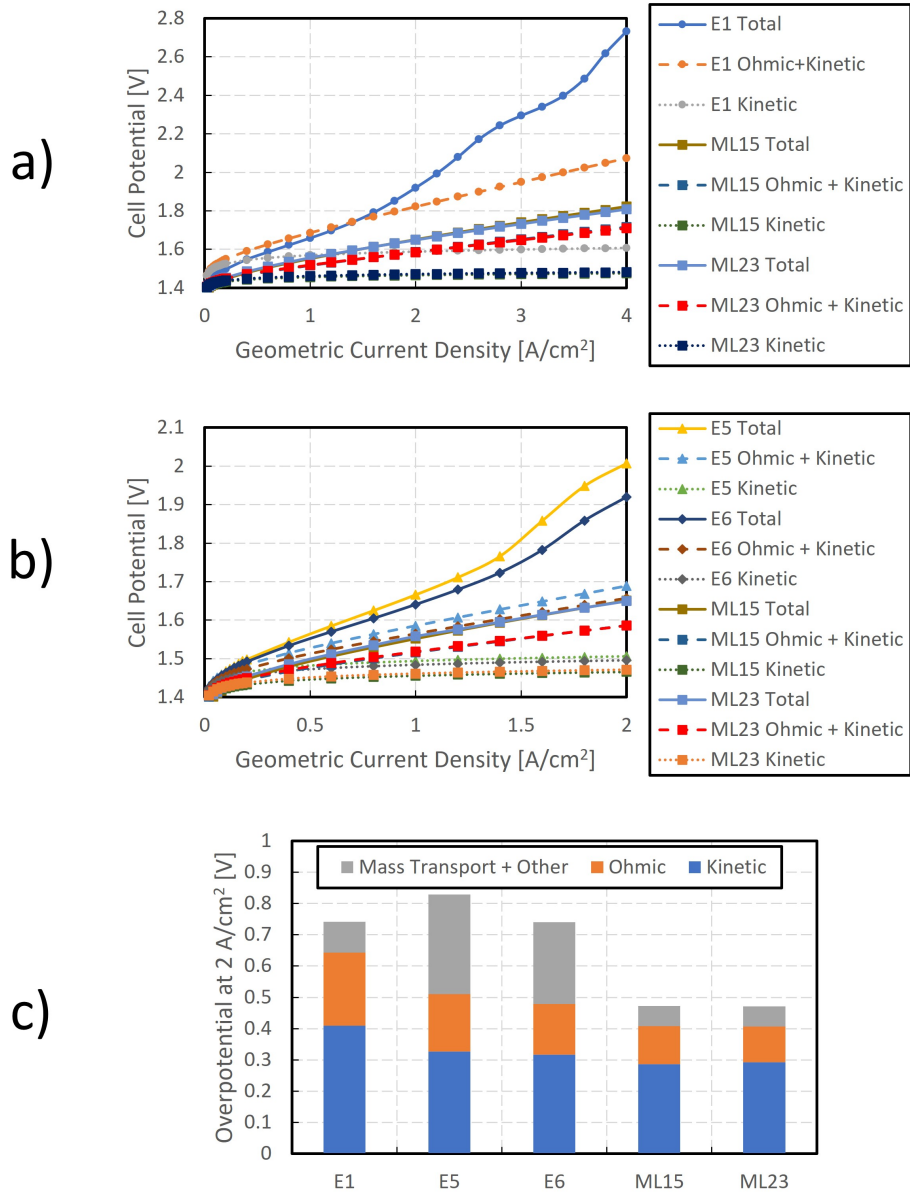


Figure 4.19: Pol. curves showing the breakdown of losses a) E1 vs ML15 and ML23, b) E5 and E6 vs ML15 and ML23. c) Overpotential of each cause of voltage loss compared across E1, E5, E6, ML15 and ML23 which stack to form the total overpotential experienced at 2 A/cm².

4.5 Final Ex Situ Characterization

Figure 4.20 shows catalyst layer surface SEM images of the tested Ir_8NiO_x and IrO_x (ML15) cells. They display the impressions made by the PTL fibers into the CCMs as well as areas where the catalyst has been completely removed from the PEM in the case of the Ir_8NiO_x catalyst.

Figure 4.21 shows the interface of each catalyst layer. It shows clearly that the layer has detached from the PEM except for where a PTL fiber was. In comparison, the IrO_x layer is still intact as shown in Figure 4.20 d) and 4.21 b).

These images provide an explanation for the severe lack of stability of the catalyst layer under operation which led to a decrease in overall performance, especially at high current density. The loss of catalyst layer could also be one of the factors for the decreased ECSA observed for the Ir_8NiO_x cells. Since ECSA is found by normalizing by the mass of catalyst on the surface, the loss of catalyst was not accounted for which means that the values for ECSA in section 4.4.2 are lower than in reality.

In Figure 4.22, EDX is used to observe that the places where the PTL laid on the CCM are precisely where the catalyst layer remains. Almost everywhere else the catalyst layer has been lost. This could be due to a couple reasons listed below:

- Bubble formation inside the catalyst layer causing the layer to be pushed off.
- The catalyst layer washing away due to dissolution or corrosion.

It has been previously determined that there is likely significant mass transport losses associated with going to high current densities and voltages where large hysteresis shows that something is not allowing the reaction to proceed efficiently. This could be due to bubbles building up at high current and not being able to leave the catalyst layer. If enough pressure was built up it is possible that the bubbles broke through the layer damaging it and the overall structural integrity. If the loss of the catalyst layer was induced by bubbles

forming under the surface then making the structure more porous could aid in layer stability as there would be a pathway for the bubbles to escape without damaging the layer.

Due to the addition of Ni and the amorphous nature of the IrO_x , the catalyst may dissolve at lower potentials than just pure IrO_x . If the catalyst itself dissolves at voltages around 2 V, which are experienced at 2 A/cm², then this catalyst may not be suitable for PEMWE.

Since the catalyst disperses well in water it was hypothesized that the act of simply interacting with water could cause the catalyst to disperse back into the water used for the reaction. To try and test this a sample of the E2 CCM, which was not used in an MEA, was placed in a petri dish filled with water and left to soak for 6 hours. It was observed under an optical microscope before and after treatment and there were no noticeable changes made. It was then put under more strenuous conditions by being placed in a water filled vial and bath sonicated for 3 hours and this also did not show any change based on the optical microscope observations. These tests seem to strengthen the idea that either dissolution or bubble formation are responsible for the loss of catalyst layer.

After considering the modes of degradation, the most likely is the delamination of the layer due to oxygen bubbles trapped under the surface. This is due to the primary area of catalyst loss occurring away from the PTL fibers. If corrosion/dissolution was the cause it would occur near the PTL fibers where the reaction is the most concentrated.

In addition to the proposed reasons above for the decrease in performance and loss of catalyst layer, Ni^{2+} , K^+ , or Cl^+ could have migrated into the Nafion membrane and blocked sites which are used to transport H^+ . EDX was performed before (E2) and after (E1) testing on the full membrane and catalyst layer interface but due to the sensitivity of the device there was no evidence of significant amounts of these ions present in the Nafion membrane.

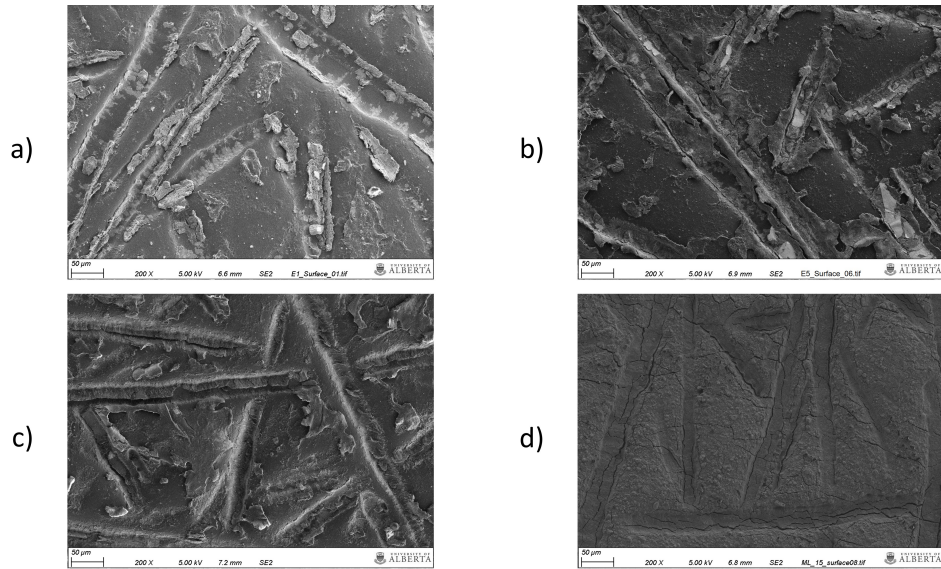


Figure 4.20: SEM at 200x magnification of the surface of tested Ir_8NiO_x and IrO_x (ML15) CCMs, a) E1, b) E5, c) E6, d) ML15

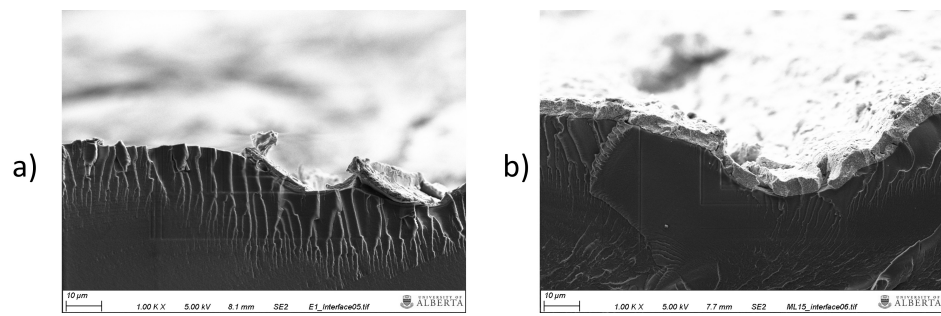


Figure 4.21: SEM at 1000x magnification of the interface of tested Ir_8NiO_x and IrO_x CCMs, a) E1, b) ML15

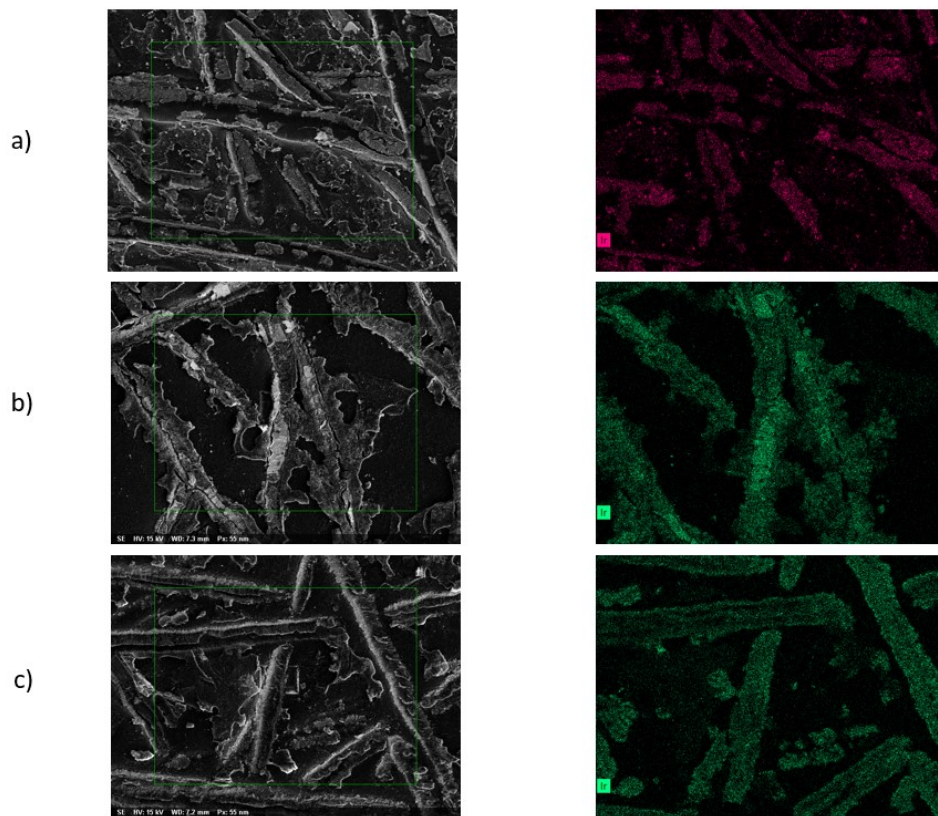


Figure 4.22: SEM (left) and EDX (right) showing the catalyst layer surface and Iridium signal of the remaining tested Ir_8NiO_x catalyst layer, a) E1, b) E5, c) E6.

4.6 Repeatability

Using the second batch of Ir_8NiO_x catalyst particles, first mentioned in section 4.1, new inks were made for repeatability. However, these inks made with the second batch of catalyst particles could not be printed. The main issue was that the particle size was larger than when the previous batch was used. To be clear this is a comparison between the inks made with batch 1 vs batch 2 not when they were simply dispersed in water as was shown in Figures 4.3 and 4.4. When dispersed in water the particle size was similar but as will be shown in this section this is not the case when a ink containing water, PG and Nafion is made.

Many attempts were made to create a suitable ink by decreasing the particle size over the course of 3 weeks. A summary of all the treatments used are listed below in the order that they were attempted, Figure 4.23, displays how the hydrodynamic diameter changed throughout the testing.

The initial particle size of 3254 nm was undesirable. Probe sonication of increasing amplitude only reduced the size to about 2592 nm. Following Test 6, the sample was magnetically stirred for 1 week at 350 rpm before continuing the attempt to decrease particle size. Following this it was found that simply leaving the ink on the magnetic stir plate at 350 rpm significantly reduced the particle size to 458.3 nm (See Test 8). The focus from this point on was trying to determine if further stirring at higher rpm or length of time would be beneficial. Although some improvement was made as the lowest particle size achieved was 412.9 nm, the ink remained unstable as the particle size increased over the course of a few hours to 872.2 nm (Tests 12-15) which is not suitable for printing.

Although probe sonication may be beneficial for breaking up large agglomerates, it was long term stirring that resulted in the more prominent decrease in particle size. Ink stability still requires improvement if new inks are to be printed successfully.

After the many attempts to formulate an ink using the second batch of Ir_8NiO_x catalyst, it was decided that the project could not go further at this

time due to time constraints, not being able to produce the same catalyst as desired which was likely due to differences in reaction scale and precipitation technique, ink fabrication, and the catalyst layer being unstable.

Treatments used in an attempt to decrease particle size:

1. Nov. 24, 2022: 30 min bath sonication and 65 min degas.
2. Nov. 30, 2022: Attempted printing ink and it didn't work as can be seen from the particle size (>3000 nm). So, the ink was bath sonicated again for 30 min and degassed for 60 min.
3. Dec. 5, 2022: 15 min probe sonication at 40 amplitude for 2 min on 1 min off in an ice bath to maintain temperature. Then the ink was degassed for 15 min.
4. Dec. 5, 2022: 15 min probe sonication at 60 amplitude for 1 min on 1 min off in an ice bath to maintain temperature. Then the ink was degassed for 15 min.
5. Dec. 6, 2022: 15 min probe sonication at 80 amplitude for 1 min on 1 min off in an ice bath to maintain temperature. Then the ink was degassed for 15 min.
6. Dec. 7, 2022: 15 min probe sonication at 100 amplitude for 1 min on 1 min off in an ice bath to maintain temperature. Then the ink was degassed for 15 min.
7. Dec. 14, 2022: Took only 1 mL of solution this time to try to concentrate it. 15 min probe sonication at 80 amplitude for 1 min on 1 min off in an ice bath to maintain temperature. Then the ink was degassed for 15 min.
8. Dec. 14, 2022: This test was done with the ink right from the magnetic stir plate without any sonication or degassing to compare this base case to Test 7.

9. Dec. 14, 2022: Probe sonicated 1 mL of ink from Test 7 again. 80 amplitude 1 min on 1 min off 15 min total. 15 min degas.
10. Dec. 14, 2022: After Test 9 the ink was recombined from Test 7 and 8 into one vial. Used the vortex mixer for 30 seconds and degassed for 1 hour.
11. Dec. 15, 2022: After Test 10 the ink was magnetically stirred for about 17 hours from 5:45pm to 10:55am at 700 rpm and then at 350 rpm until 2:56pm. Took directly off magnetic stir plate for DLS test.
12. Dec. 16, 2022: After Test 11 magnetically stirred for about 19 hours 45 mins from 4:45pm to 12:16am at 1100 rpm and then at 350 rpm until 12:26pm. Took directly off magnetic stir plate for DLS test.
13. Dec. 16, 2022: After Test 12 ink was left in the Litsizer 500 and DLS was run again.
14. Dec. 16, 2022: After Test 13 ink was left in the Litsizer 500 and DLS was run again.
15. Dec. 16, 2022: After Test 14 ink was left in the Litsizer 500 and DLS was run again.
16. Dec. 19, 2022: Attempted printing and it still wasn't working so this sample was taken directly from the printer ink cartridge after failing to print and DLS was run.

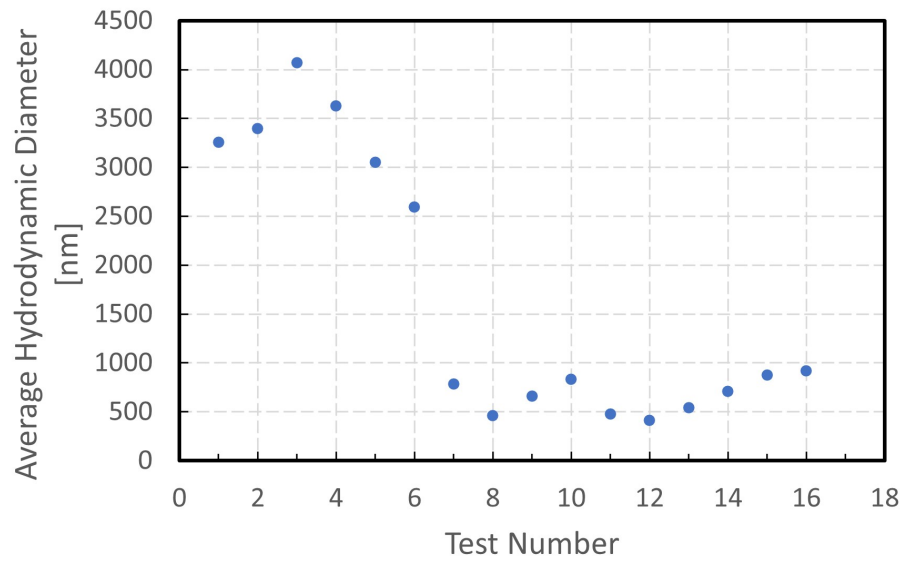


Figure 4.23: The average hydrodynamic diameter after each test given in the list above.

Chapter 5

Conclusions and Future Work

5.1 Conclusions

In this work, two different methods were used to reduce the Ir loading in the anode of PEMWE cells.

The first method of reducing Ir in the anode catalyst layer was to reduce the layer thickness and therefore the loading of a low electrically conductive and highly active catalyst layer. The electronic conductivity of IrO_x TKK is low, which according to numerical modelling by Michael Moore, predicted that it should be possible to reduce catalyst loading while improving performance [29]. The performance theoretically improves due to a reduction in ohmic losses corresponding to easier charge transport through a thinner layer while maintaining kinetic performance as the same amount of the catalyst layer is being utilized. IrO_x inks were developed by first adding PG to the catalyst followed by IPA to help dispersion and then Nafion added as the ionomer. The resulting ink had a Z value of 3.76 and an average particle diameter of 194 nm which are suitable for the Samba cartridges used. Four batches of this ink were successfully printed to form the IrO_x anode. An ink containing platinum supported on carbon was printed on the other side of the membrane to form the cathode. Each batch consisted of four loadings of approximately 0.25, 0.5, 0.75 and 1 mg/cm² of IrO_x. The SEM of each loading found that the thickness of the catalyst layer increases linearly with loading while porosity was maintained.

Once assembled in an MEA the IrO_x cells were electrochemically char-

acterized using polarization curves, cyclic voltammetry, linear sweep voltammetry and electrochemical impedance spectroscopy. Of the three IrO_x loading batches tested, the first two had similar overall performance on the pol. curves between their respective loadings. The fourth batch had similar performance for the 0.5 and 0.75 mg/cm^2 cells, but worse performance for the 0.25 mg/cm^2 cell and better performance for the 1 mg/cm^2 cell. The difference between the 0.25 and 1 mg/cm^2 cells in batch 4 was 44 mV whereas the largest difference between a given loading across the three batches was about 36 mV. Looking at the HFR, batch 1 and 2 see a slight decrease in HFR with a decrease in loading which was expected. Batch 4 deviates slightly from this trend as the HFR remained fairly constant which may be why there is a difference between batch 4 and the others.

When compared to literature using IrO_x TKK, such as Fujita and Taie, the results were similar for alike loadings [12, 57]. Fujita found that the performance began decreasing significantly after going below 0.2-0.3 mg/cm^2 . In Taie's work they also saw a decrease in overall performance below 0.17 mg/cm^2 .

Although the results of the loading study in this work show a similar performance between different loadings, the model by Moore predicted an increased performance at low loadings which was not seen in this work. This was found to be due to the increase in kinetic losses equally counteracting the decrease in ohmic losses as the loading decreased. This suggested that there was more catalyst being utilized in the high loading cells than originally predicted by Moore's model. It was questioned whether the electrical conductivity was as low as originally thought. In addition impressions from the PTL were left in the catalyst layers suggesting that the compression could also be a source of the deviation from the model. A setup was made which allowed the through-plane conductivity of catalyst layer to be measured under varying pressure. IrO_x catalyst layers of each of the four loadings were printed on to gold plates and a gold block was placed on top, which was then pressed down with a piston via compressed gas. Both the compression and the loading were found to have an impact on the resistance as the resistance decreased with an increase in compression and decrease in loading. The increase in applied pressure re-

sulted in a linear increase in conductivity. The compression was expected to make a difference, due to better contact being made between the gold block and the catalyst layer. The effect of catalyst loading was expected as since layer thickness decreased. The resistance-thickness plot did not have linear lines that naturally went through (0,0). The change was explained by potentially not accounting for the thickness of the layer while under compression as the uncompressed thickness was used to calculate the conductivity. The need for repeatability requires further conductivity testing.

To answer the first research question and hypothesis, although the performance was not improved by decreasing the loading, it remained the same. This is significant as it shows that similar performance can be achieved at a 4x reduction in IrO_x loading.

The second method utilized Ni to enhance the d-band structure of Ir, allowing optimized adsorption and desorption of intermediate species during the oxygen evolution reaction, thus leading to an improvement in the catalyst activity. A Ir_8NiO_x catalyst was synthesized using the procedure by Moghadam [67] which used an aqueous alkaline reaction. For this work, this process was scaled up to produce hundreds of milligrams of catalyst per batch. The catalyst particles were found to have a non-uniform distribution of Ni based on TEM done in this work. Although the particle size of a few aggregates was found using TEM, a better representation of the particle size was found through the utilization of DLS of the catalyst dispersed in water which found a 300-400 nm average hydrodynamic diameter. The particle properties in this work differed from that of the original paper [67] suggesting the same catalyst was not made.

Catalyst inks were made using the Ir_8NiO_x catalyst by first adding water to disperse the catalyst followed by PG to increase viscosity and then Nafion added as the ionomer. Initial guesses for PG-water ratio and the ink fluid properties were made based on Khattab's work [111] and were confirmed through density and viscosity tests. The density and viscosity are critical to ensure that the ink is likely to print well as a range for the Z value of 3.1-5.8 is acceptable. It was found that the Ir_8NiO_x catalyst had an approximate

Z value of 4.3. DLS of the ink also provided a particle size of about 386 nm which was suitable for printing. A Dimatix inkjet printer was used to print the Ir_8NiO_x catalyst ink on one side of the Nafion 212 membrane while a platinum supported on carbon ink was printed on the opposite side.

The Ir_8NiO_x catalyst layer was initially characterized using SEM and EDX which showed that the layer thickness and porosity of an Ir_8NiO_x catalyst layer was less than that of IrO_x TKK. The EDX showed that the Ir-Ni atomic ratio was close to 16:1 which is twice the ideal ratio of 8:1. The difference in atomic ratio could have been due to issues in the synthesis and precipitation or the Ni content being so low at the surface that it was difficult to detect using EDX.

Once assembled in an MEA the Ir_8NiO_x cells were electrochemically characterized using polarization curves, cyclic voltammetry, linear sweep voltammetry and electrochemical impedance spectroscopy. The overall performance seen in the polarization curves was worse (i.e, more voltage loss) for the Ir_8NiO_x cells compared to IrO_x TKK. Using Tafel analysis of the simplified Butler-Volmer equation [36] the kinetic parameters were found including the exchange current density and Tafel slope which were higher for Ir_8NiO_x . Higher exchange current density corresponds to a more active catalyst; whereas the higher Tafel slope means there are more losses per decade increase in current. Together these results signify that the Ir_8NiO_x catalyst is similarly or more active than IrO_x but deteriorates faster. The ECSA of the Ir_8NiO_x was also found to be much lower than IrO_x , possibly signifying a lower catalyst surface area for Ir_8NiO_x . Low ECSA could also be due to the low porosity of the Ir_8NiO_x layer or low surface roughness. When the polarization curves are normalized by the ECSA the Ir_8NiO_x cells actually perform better than IrO_x , again showing that the Ir_8NiO_x that was made may possess a higher activity.

The kinetic and ohmic losses were used to decompose the overall pol. curves into the kinetic, ohmic, and mass transport or other losses at 2 A/cm². The kinetic and ohmic losses are slightly higher for Ir_8NiO_x but the mass transport and other losses make up the majority of the difference between the Ir_8NiO_x and IrO_x cells. This aligns with the lower porosity found for Ir_8NiO_x since there isn't as much room to allow both oxygen to escape and water to enter the

catalyst layer. Utilizing SEM and EDX it was found that a significant portion of the Ir_8NiO_x catalyst layers were degraded to the point where catalyst only remained where the PTL physically held it against the membrane. Due to low porosity, bubbles formed inside the catalyst layer may have been forced out of the layer by pushing it apart.

Repeatability was explored using the second batch of Ir_8NiO_x and found it to be impossible due to large particle aggregates. This again showed inconsistency in the precipitation process as the desired catalyst was not produced. Due to having the incorrect catalyst, difficulty making a repeatable ink and the instability of the catalyst layer, further testing was not performed and the project was abandoned.

To answer the second research question and hypothesis, when normalized by active catalyst area, the performance of the Ir_8NiO_x catalyst was higher showing that more current can be produced per area of catalyst. This improved performance shows that it is possible to reduce the amount of Ir used in the catalyst layer. However, Ir_8NiO_x catalyst layers suffered from severe degradation. This showed that the catalyst layer structure is just as important as the catalyst activity as it must stay intact during cell operation. To utilize the increased activity of the Ir_8NiO_x catalyst, the stability and structure of the catalyst layer need to be improved.

5.2 Future Work

Based on the results of this thesis there is further work that can be done to improve the catalyst layers studied and confirm results.

In terms of the IrO_x loading study the two points requiring further research are further decreasing the catalyst loading such that large losses in performance are observed, and the catalyst layer electrical conductivity both through-plane and in-plane. As Fujita showed, around 0.2 mg/cm^2 is the limit of how low the loading can be before substantial losses occur [57]. It would be good to independently confirm this limit for IrO_x TKK. There are three ways that the electrical conductivity can be looked at further. The first is to perform

more through-plane measurements to ensure repeatability. The second is the in-plane electrical conductivity, which due to the cracks in the low loading layers could effect the ECSA and overall performance if there is lost active area; the in-plane conductivity should be measured to determine if this is true or not. Lastly, the in-plane and through-plane electrical conductivity could be improved using an electrically conductive polymer, such as PEDOT, which could lessen the effects of cracks. The use of PEDOT on low loading iridium catalyst layers has recently been reported to increase the performance of an iridium catalyst layer with a loading of about 0.3 mg/cm^2 [119].

The main problems with the Ir_8NiO_x catalyst layer was not producing the correct catalyst and the stability of the layer which resulted in large mass transport losses and low active surface area.

To increase the stability of the layer, as well as the porosity, and to improve mass transport, a support or pore former could be added. Common supports which have the ability to resist oxidation and provide additional electrical conductivity are ATO, ITO and FTO [109]. A sacrificial support, such as carbon, could be used as a pore former since it corrodes at potentials seen at the anode leaving behind pores [30].

To improve the low active surface area, the catalyst particle size could be decreased by adjusting the ink composition to minimize aggregate growth and using other physical grinding techniques [113]. In addition, the surface roughness of the catalyst layer could be increased again by the ink composition or deposition technique [114].

Unfortunately, the second batch of Ir_8NiO_x catalyst was not able to be produced into an ink which led to issues in reproducing the experiments. The primary problem was the catalyst particles aggregating and clogging the printer nozzles. Further investigation into the procedure for precipitating and cleaning the catalyst particles is needed to ensure similar particle-particle interactions.

Transitioning from producing and testing a catalyst on a small scale to a larger scale is a very challenging endeavour. For the scale up to be successful there must be close collaboration between those that develop and produce the catalyst and those that use the catalyst to form an ink and create and test a

larger catalyst layer. As was seen in the differences between RDE and MEA testing, there is a difference in failure mechanisms at each scale. At the small scale the activity of the catalyst is of the most importance. On a larger scale, the catalyst incorporated into an ink, must also form the appropriate catalyst layer structure. These differences need to be taken into account by all parties at all steps of the catalyst development. If the Ir_8NiO_x project is to continue in the future, the scale up and precipitation techniques need to be optimized to more closely match the resultant catalyst from the original paper [67].

There is still lots of work to do to reach the goals of 0.1 or even 0.05 $\text{mg}_{\text{Ir}}/\text{cm}^2$ by 2050. These loadings are being approached as this work went as low as 0.25 mg/cm^2 . Other works, such as Taie et. al., have found good performance on a mass basis all the way to 0.011 mg/cm^2 of IrO_x [12]. Even so, there is a need to run long term stability and accelerated stress tests to ensure that these low loadings are capable of lasting a long time with little degradation. When this is achieved PEMWE will be a reliable large scale storage method for intermittent renewable energy in the form of hydrogen while using only a small portion of the worlds iridium reserves.

References

- [1] Nick Zrinyi. *List of Countries with Net-Zero Commitments and Climate Accountability Legislation*. Accessed on November 9, 2023. URL: <https://rosagalvez.ca/en/initiatives/climate-accountability/list-of-countries-with-net-zero-commitments-and-climate-accountability-legislation/>.
- [2] *2030 emissions reduction plan : Canada's next steps to clean air and a strong economy*. Environment and Climate Change Canada. ISBN: 9780660426860.
- [3] Sushyanth Sridhar and Surender Reddy Salkuti. "Development and Future Scope of Renewable Energy and Energy Storage Systems." In: *Smart Cities* 5, 2, 2022, pp. 668–699. ISSN: 26246511. DOI: 10.3390/smartcities5020035.
- [4] Georg Bopp, Matthias Merkle, Tom Smolinka, Simon Schwunk, and Gunther Ebert. *Study on Storage for a Regenerative Electricity Supply*. Fraunhofer ISE, 2011.
- [5] Shaun Alia, Dong Ding, Anthony McDaniel, Francesca M. Toma, and Huyen N. Dinh. "Chalkboard 2-How to Make Clean Hydrogen." In: 30, 49, 2021.
- [6] Mohsen Fallah Vostakola, Hasan Ozcan, Rami S. El-Emam, and Bahman Amini Horri. "Recent Advances in High-Temperature Steam Electrolysis with Solid Oxide Electrolysers for Green Hydrogen Production." In: *Energies* 16, 8, 2023. ISSN: 19961073. DOI: 10.3390/en16083327.
- [7] Xuesong Wei, Takumi Kakimoto, Yutaro Umehara, Hironori Nakajima, Kohei Ito, Hiromitsu Inagaki, and Shoji Mori. "Improvement of the critical current density of alkaline water electrolysis based on the hydrodynamic similarity between boiling and water electrolysis." In: *International Journal of Heat and Mass Transfer* 214, 2023. ISSN: 00179310. DOI: 10.1016/j.ijheatmasstransfer.2023.124420.
- [8] Qiannan Wu, Yuannan Wang, Kexin Zhang, Zhoubing Xie, Ke Sun, Wei An, Xiao Liang, and Xiaoxin Zou. "Advances and status of anode catalysts for proton exchange membrane water electrolysis technology." In: *Materials Chemistry Frontiers* 7, 6, 2023, pp. 1025–1045. ISSN: 20521537. DOI: 10.1039/d3qm00010a.

- [9] Ganesan Sriram, Karmegam Dhanabalan, Kanalli V. Ajeya, Kanakara, Aruchamy, Yern Chee Ching, Tae Hwan Oh, Ho Young Jung, and Mahaveer Kurkuri. “Recent progress in anion exchange membranes (AEMs) in water electrolysis: synthesis, physio-chemical analysis, properties, and applications.” In: *Journal of Materials Chemistry A* 11, 2023. ISSN: 20507496. DOI: 10.1039/d3ta04298g.
- [10] Furat Dawood, Martin Anda, and G. M. Shafiullah. “Hydrogen production for energy: An overview.” In: *International Journal of Hydrogen Energy* 45, 7, 2020, pp. 3847–3869. ISSN: 03603199. DOI: 10.1016/j.ijhydene.2019.12.059.
- [11] Ahmad Mayyas, Mark Ruth, Bryan Pivovar, Guido Bender, and Keith Wipke. *Manufacturing Cost Analysis for Proton Exchange Membrane Water Electrolyzers*. Tech. rep. NREL, 2019.
- [12] Zachary Taie, Xiong Peng, Devashish Kulkarni, Iryna V. Zenyuk, Adam Z. Weber, Christopher Hagen, and Nemanja Danilovic. “Pathway to Complete Energy Sector Decarbonization with Available Iridium Resources using Ultralow Loaded Water Electrolyzers.” In: *ACS Applied Materials and Interfaces* 12, 47, 2020, pp. 52701–52712. ISSN: 19448252. DOI: 10.1021/acsami.0c15687.
- [13] Maximilian Bernt, Armin Siebel, and Hubert A. Gasteiger. “Analysis of Voltage Losses in PEM Water Electrolyzers with Low Platinum Group Metal Loadings.” In: *Journal of The Electrochemical Society* 165, 5, 2018, F305–F314. ISSN: 0013-4651. DOI: 10.1149/2.0641805jes.
- [14] Maximilian Bernt, Alexandra Hartig-Weiß, Mohammad Fathi Tovini, Hany A. El-Sayed, Carina Schramm, Jonas Schröter, Christian Gebauer, and Hubert A. Gasteiger. “Current Challenges in Catalyst Development for PEM Water Electrolyzers.” In: *Chemie-Ingenieur-Technik* 92, 1-2, 2020, pp. 31–39. ISSN: 15222640. DOI: 10.1002/cite.201900101.
- [15] Mark Clapp, Christopher M. Zalitis, and Margery Ryan. “Perspectives on current and future iridium demand and iridium oxide catalysts for PEM water electrolysis.” In: *Catalysis Today* 420, 2023. ISSN: 09205861. DOI: 10.1016/j.cattod.2023.114140.
- [16] Zhaoping Shi, Xian Wang, Junjie Ge, Changpeng Liu, and Wei Xing. “Fundamental understanding of the acidic oxygen evolution reaction: Mechanism study and state-of-the-art catalysts.” In: *Nanoscale* 12, 25, 2020, pp. 13249–13275. ISSN: 20403372. DOI: 10.1039/d0nr02410d.
- [17] Chao Huang, Ping Qin, Yang Luo, Qingdong Ruan, Liangliang Liu, Yuzheng Wu, Qingwei Li, Yue Xu, Rugeng Liu, and Paul K. Chu. “Recent progress and perspective of cobalt-based catalysts for water splitting: design and nanoarchitectonics.” In: *Materials Today Energy* 23, 2022. ISSN: 24686069. DOI: 10.1016/j.mtener.2021.100911.

- [18] Hideshi Ooka, Jun Huang, and Kai S. Exner. “The Sabatier Principle in Electrocatalysis: Basics, Limitations, and Extensions.” In: *Frontiers in Energy Research* 9, 2021. ISSN: 2296598X. DOI: 10.3389/fenrg.2021.654460.
- [19] Meihong Fan, Xiao Liang, Hui Chen, and Xiaoxin Zou. “Low-iridium electrocatalysts for acidic oxygen evolution.” In: *Dalton Transactions* 49, 44, 2020, pp. 15568–15573. ISSN: 14779234. DOI: 10.1039/d0dt02676j.
- [20] Nian Tzu Suen, Sung Fu Hung, Quan Quan, Nan Zhang, Yi Jun Xu, and Hao Ming Chen. “Electrocatalysis for the oxygen evolution reaction: Recent development and future perspectives.” In: *Chemical Society Reviews* 46, 2, 2017, pp. 337–365. ISSN: 14604744. DOI: 10.1039/c6cs00328a.
- [21] Marcelo Carmo, David L. Fritz, Jürgen Mergel, and Detlef Stolten. “A comprehensive review on PEM water electrolysis.” In: *International Journal of Hydrogen Energy* 38, 12, 2013, pp. 4901–4934. ISSN: 03603199. DOI: 10.1016/j.ijhydene.2013.01.151.
- [22] Ayşenur Öztürk, Ramiz Gültekin Akay, Serdar Erkan, and Ayşe Bayrakçeken Yurtcan. “Introduction to fuel cells.” In: Elsevier, 2020, pp. 1–47. ISBN: 9780128186244. DOI: 10.1016/B978-0-12-818624-4.00001-7.
- [23] Hiroshi Ito, Tetsuhiko Maeda, Akihiro Nakano, and Hiroyasu Takenaka. “Properties of Nafion membranes under PEM water electrolysis conditions.” In: *International Journal of Hydrogen Energy* 36, 17, 2011, pp. 10527–10540. ISSN: 03603199. DOI: 10.1016/j.ijhydene.2011.05.127.
- [24] Reza B. Moghaddam and E. Bradley Easton. “The interplay between impedance parameters, structure, and performance of fuel cell catalyst layers.” In: *Chemical Engineering Science* 224, 2020. ISSN: 00092509. DOI: 10.1016/j.ces.2020.115792.
- [25] Yizhe Li, Zhiyong Fu, Yifan Li, and Guichen Zhang. “A Comparative Study of CCM and CCS Membrane Electrode Assemblies for High-Temperature Proton Exchange Membrane Fuel Cells with a CsH₅(PO₄)₂-Doped Polybenzimidazole Membrane.” In: *Materials* 16, 11, 2023. ISSN: 19961944. DOI: 10.3390/ma16113925.
- [26] Jooyoung Kim, Junhyeong Kim, Hyunki Kim, and Sang Hyun Ahn. “Nanoporous Nickel Phosphide Cathode for a High-Performance Proton Exchange Membrane Water Electrolyzer.” In: *ACS Applied Materials and Interfaces* 11, 34, 2019, pp. 30774–30785. ISSN: 19448252. DOI: 10.1021/acsami.9b08074.

- [27] Sun Young Kang, Ji Eun Park, Ga Young Jang, Changsoon Choi, Yong Hun Cho, and Yung Eun Sung. “Directly Coated Iridium Nickel Oxide on Porous-Transport Layer as Anode for High-Performance Proton-Exchange Membrane Water Electrolyzers.” In: *Advanced Materials Interfaces* 10, 12, 2023. ISSN: 21967350. DOI: 10.1002/admi.202202406.
- [28] Manas Mandal, Antoni Valls, Niklas Gangnus, and Marc Secanell. “Analysis of Inkjet Printed Catalyst Coated Membranes for Polymer Electrolyte Electrolyzers.” In: *Journal of The Electrochemical Society* 165, 7, 2018, F543–F552. ISSN: 0013-4651. DOI: 10.1149/2.1101807jes.
- [29] Manas Mandal, Michael Moore, and Marc Secanell. “Measurement of the Protonic and Electronic Conductivities of PEM Water Electrolyzer Electrodes.” In: *ACS Applied Materials and Interfaces* 12, 44, 2020, pp. 49549–49562. ISSN: 19448252. DOI: 10.1021/acscami.0c12111.
- [30] Manas Mandal and Marc Secanell. “Improved polymer electrolyte membrane water electrolyzer performance by using carbon black as a pore former in the anode catalyst layer.” In: *Journal of Power Sources* 541, 2022. ISSN: 03787753. DOI: 10.1016/j.jpowsour.2022.231629.
- [31] L. Padilla Urbina, J. Liu, N. Semagina, and M. Secanell. “Low loading inkjet printed bifunctional electrodes for proton exchange membrane unitized regenerative fuel cells.” In: *Journal of Power Sources* 580, 2023. ISSN: 03787753. DOI: 10.1016/j.jpowsour.2023.233448.
- [32] Guido Bender, Thomas A. Zawodzinski, and Andrew P. Saab. “Fabrication of high precision PEFC membrane electrode assemblies.” In: *Journal of Power Sources* 124, 1, 2003, pp. 114–117. ISSN: 03787753. DOI: 10.1016/S0378-7753(03)00735-3.
- [33] In Su Park, Wen Li, and Arumugam Manthiram. “Fabrication of catalyst-coated membrane-electrode assemblies by doctor blade method and their performance in fuel cells.” In: *Journal of Power Sources* 195, 20, 2010, pp. 7078–7082. ISSN: 03787753. DOI: 10.1016/j.jpowsour.2010.05.004.
- [34] Megan B. Sassin, Yannick Garsany, Benjamin D. Gould, and Karen E. Swider-Lyons. “Fabrication Method for Laboratory-Scale High-Performance Membrane Electrode Assemblies for Fuel Cells.” In: *Analytical Chemistry* 89, 1, 2017, pp. 511–518. ISSN: 15206882. DOI: 10.1021/acs.analchem.6b03005.
- [35] Tobias Seifert, Enrico Sowade, Frank Roscher, Maik Wiemer, Thomas Gessner, and Reinhard R. Baumann. “Additive manufacturing technologies compared: Morphology of deposits of silver ink using inkjet and aerosol jet printing.” In: *Industrial and Engineering Chemistry Research* 54, 2, 2015, pp. 769–779. ISSN: 15205045. DOI: 10.1021/ie503636c.
- [36] Allen J. Bard and Larry R. Faulkner. *Electrochemical methods : fundamentals and applications*. ISBN: 0471043729.

- [37] Xuehai Tan, Jing Shen, Natalia Semagina, and Marc Secanell. “Decoupling structure-sensitive deactivation mechanisms of Ir/IrOx electrocatalysts toward oxygen evolution reaction.” In: *Journal of Catalysis* 371, 2019, pp. 57–70. ISSN: 10902694. DOI: 10.1016/j.jcat.2019.01.018.
- [38] Sladjana Martens, Ludwig Asen, Giorgio Ercolano, Fabio Dionigi, Chris Zalitis, Alex Hawkins, Alejandro Martinez Bonastre, Lukas Seidl, Alois C. Knoll, Jonathan Sharman, Peter Strasser, Deborah Jones, and Oliver Schneider. “A comparison of rotating disc electrode, floating electrode technique and membrane electrode assembly measurements for catalyst testing.” In: *Journal of Power Sources* 392, 2018, pp. 274–284. ISSN: 03787753. DOI: 10.1016/j.jpowsour.2018.04.084.
- [39] Timon Lazaridis, Björn M. Stühmeier, Hubert A. Gasteiger, and Hany A. El-Sayed. “Capabilities and limitations of rotating disk electrodes versus membrane electrode assemblies in the investigation of electrocatalysts.” In: *Nature Catalysis* 5, 5, 2022, pp. 363–373. ISSN: 25201158. DOI: 10.1038/s41929-022-00776-5.
- [40] F. N. Khatib, Tabbi Wilberforce, Oluwatosin Ijaodola, Emmanuel Ogungbemi, Zaki El-Hassan, A. Durrant, J. Thompson, and A. G. Olabi. “Material degradation of components in polymer electrolyte membrane (PEM) electrolytic cell and mitigation mechanisms: A review.” In: *Renewable and Sustainable Energy Reviews* 111, 2019, pp. 1–14. ISSN: 18790690. DOI: 10.1016/j.rser.2019.05.007.
- [41] Mohammad Fathi Tovini, Alexandra Hartig-Weiß, Hubert A. Gasteiger, and Hany A. El-Sayed. “The Discrepancy in Oxygen Evolution Reaction Catalyst Lifetime Explained: RDE vs MEA - Dynamicity within the Catalyst Layer Matters.” In: *Journal of The Electrochemical Society* 168, 1, 2021, p. 014512. ISSN: 0013-4651. DOI: 10.1149/1945-7111/abdcc9.
- [42] Dennis Bastian. *Preismonitor*. Tech. rep. Federal Institute for Geosciences and Natural Resources - BGR, 2019.
- [43] showtheplanet inc. *Daily Metal Prices*. Accessed on 25/10/2023. 2019. URL: <https://www.dailymetalprice.com/>.
- [44] Mohammad Ahadi, Mickey Tam, Jürgen Stumper, and Majid Bahrami. “Electronic conductivity of catalyst layers of polymer electrolyte membrane fuel cells: Through-plane vs. in-plane.” In: *International Journal of Hydrogen Energy* 44, 7, 2019, pp. 3603–3614. ISSN: 03603199. DOI: 10.1016/j.ijhydene.2018.12.016.
- [45] Marc Secanell Michael Moore Manas Mandal. “A Numerical Study on the Impact of Low Electronic Conductivity on PEMWE Electrolyser Performance.” In: vol. MA2021-01 1192. 2021. DOI: 10.1149/MA2021-01381192mtgabs.

- [46] Krzysztof A. Lewinski, Dennis van der Vliet, and Sean M. Luopa. “NSTF Advances for PEM Electrolysis - the Effect of Alloying on Activity of NSTF Electrolyzer Catalysts and Performance of NSTF Based PEM Electrolyzers.” In: *ECS Transactions* 69, 17, 2015, pp. 893–917. ISSN: 1938-5862. DOI: 10.1149/06917.0893ecst.
- [47] Caroline Rozain, Eric Mayousse, Nicolas Guillet, and Pierre Millet. “Influence of iridium oxide loadings on the performance of PEM water electrolysis cells: Part I-Pure IrO₂-based anodes.” In: *Applied Catalysis B: Environmental* 182, 2016, pp. 153–160. ISSN: 09263373. DOI: 10.1016/j.apcatb.2015.09.013.
- [48] Shaun M. Alia, Sarah Stariha, and Rod L. Borup. “Electrolyzer Durability at Low Catalyst Loading and with Dynamic Operation.” In: *Journal of The Electrochemical Society* 166, 15, 2019, F1164–F1172. ISSN: 0013-4651. DOI: 10.1149/2.0231915jes.
- [49] Friedemann Hegge, Florian Lombeck, Edgar Cruz Ortiz, Luca Bohn, Miriam Von Holst, Matthias Kroschel, Jessica Hübner, Matthias Breitwieser, Peter Strasser, and Severin Vierrath. “Efficient and Stable Low Iridium Loaded Anodes for PEM Water Electrolysis Made Possible by Nanofiber Interlayers.” In: *ACS Applied Energy Materials* 3, 9, 2020, pp. 8276–8284. ISSN: 25740962. DOI: 10.1021/acsaem.0c00735.
- [50] Ugljesa Babic, Elisabeth Nilsson, Alexandra Pătru, Thomas J. Schmidt, and Lorenz Gubler. “Proton Transport in Catalyst Layers of a Polymer Electrolyte Water Electrolyzer: Effect of the Anode Catalyst Loading.” In: *Journal of The Electrochemical Society* 166, 4, 2019, F214–F220. ISSN: 0013-4651. DOI: 10.1149/2.0341904jes.
- [51] Yeonghwan Jang, Changwook Seol, Sang Moon Kim, and Segeun Jang. “Investigation of the correlation effects of catalyst loading and ionomer content in an anode electrode on the performance of polymer electrode membrane water electrolysis.” In: *International Journal of Hydrogen Energy* 47, 42, 2022, pp. 18229–18239. ISSN: 03603199. DOI: 10.1016/j.ijhydene.2022.04.019.
- [52] Melanie Bühler, Friedemann Hegge, Peter Holzapfel, Markus Bierling, Michel Suermann, Severin Vierrath, and Simon Thiele. “Optimization of anodic porous transport electrodes for proton exchange membrane water electrolyzers.” In: *Journal of Materials Chemistry A* 7, 47, 2019, pp. 26984–26995. ISSN: 20507496. DOI: 10.1039/c9ta08396k.
- [53] Lirong Ma, Sheng Sui, and Yuchun Zhai. “Investigations on high performance proton exchange membrane water electrolyzer.” In: *International Journal of Hydrogen Energy* 34, 2, 2009, pp. 678–684. ISSN: 03603199. DOI: 10.1016/j.ijhydene.2008.11.022.

- [54] Jingke Mo, Zhenye Kang, Scott T Retterer, David A Cullen, Todd J Toops, Johny B Green, Matthew M Mench, and Feng-Yuan Zhang. “Discovery of true electrochemical reactions for ultrahigh catalyst mass activity in water splitting.” In: *Science Advances* 2, 2016. DOI: 10.1126/sciadv.1600690. URL: <https://www.science.org>.
- [55] Gaoqiang Yang, Shule Yu, Yifan Li, Kui Li, Lei Ding, Zhiqiang Xie, Weitian Wang, and Feng Yuan Zhang. “Role of electron pathway in dimensionally increasing water splitting reaction sites in liquid electrolytes.” In: *Electrochimica Acta* 362, 2020. ISSN: 00134686. DOI: 10.1016/j.electacta.2020.137113.
- [56] Matthias Kroschel, Arman Bonakdarpour, Jason Tai Hong Kwan, Peter Strasser, and David P. Wilkinson. “Analysis of oxygen evolving catalyst coated membranes with different current collectors using a new modified rotating disk electrode technique.” In: *Electrochimica Acta* 317, 2019, pp. 722–736. ISSN: 00134686. DOI: 10.1016/j.electacta.2019.05.011.
- [57] Mitsuharu Fujita, Ikkei Arima, Hiroki Goto, Saki Konaka, and Tomoyuki Tada. “The Relationship between Activity and Durability of Surface Area and Catalyst Loading of IrOx Anode Catalyst in Proton Exchange Membrane Water Electrolysis (PEMWE).” In: *ECS Meeting Abstracts* MA2020-02, 2020, p. 2466. DOI: 10.1149/MA2020-02382466mtgabs.
- [58] Christopher P. Thornton, C. C. Lamberg-Karlovsky, Martin Liezers, and Suzanne M.M. Young. “On pins and needles: Tracing the evolution of copper-base alloying at Tepe Yahya, Iran, via ICP-MS analysis of common-place items.” In: *Journal of Archaeological Science* 29, 12, 2002, pp. 1451–1460. ISSN: 03054403. DOI: 10.1006/jasc.2002.0809.
- [59] Elin Figueiredo, Rui J.C. Silva, João C. Senna-Martinez, M. Fátima Araújo, Francisco M. Braz Fernandes, and João L. Inês Vaz. “Smelting and recycling evidences from the Late Bronze Age habitat site of Baiões (Viseu, Portugal).” In: *Journal of Archaeological Science* 37, 7, 2010, pp. 1623–1634. ISSN: 10959238. DOI: 10.1016/j.jas.2010.01.023.
- [60] The Editors of Encyclopedia Britannica. *bronze*. Accessed 11 December 2023. URL: <https://www.britannica.com/technology/bronze-alloy>.
- [61] Satadeep Bhattacharjee, Umesh V. Waghmare, and Seung Cheol Lee. “An improved d-band model of the catalytic activity of magnetic transition metal surfaces.” In: *Scientific Reports* 6, 2016. ISSN: 20452322. DOI: 10.1038/srep35916.
- [62] Ying Wang, Lei Zhang, Kuibo Yin, Jie Zhang, Hui Gao, Na Liu, Zhangquan Peng, and Zhonghua Zhang. “Nanoporous Iridium-Based Alloy Nanowires as Highly Efficient Electrocatalysts Toward Acidic Oxygen Evolution

- Reaction.” In: *ACS Applied Materials and Interfaces* 11, 43, 2019, pp. 39728–39736. ISSN: 19448252. DOI: 10.1021/acsami.9b09412.
- [63] Zhandong Ren, Yanyan Wang, Hucheng Jiang, Hongwei Jiang, Miaojie Tian, Ye Liu, Juanjuan Han, Hua Fang, and Yuchan Zhu. “A novel bifunctional catalyst for overall water electrolysis: Nano Ir: XMn(1-x)Oyhybrids with L12-IrMn3phase.” In: *Chemical Communications* 58, 5, 2022, pp. 685–688. ISSN: 1364548X. DOI: 10.1039/d1cc06062g.
- [64] Jia Du, Jonathan Quinson, Damin Zhang, Francesco Bizzotto, Alessandro Zana, and Matthias Arenz. “Bifunctional Pt-IrO₂Catalysts for the Oxygen Evolution and Oxygen Reduction Reactions: Alloy Nanoparticles versus Nanocomposite Catalysts.” In: *ACS Catalysis* 11, 2, 2021, pp. 820–828. ISSN: 21555435. DOI: 10.1021/acscatal.0c03867.
- [65] Hao Hu, Farhad M.D. Kazim, Zihao Ye, Yuhua Xie, Quan Zhang, Konggang Qu, Jingxiang Xu, Weiwei Cai, Shenglin Xiao, and Zehui Yang. “Electronically delocalized Ir enables efficient and stable acidic water splitting.” In: *Journal of Materials Chemistry A* 8, 38, 2020, pp. 20168–20174. ISSN: 20507496. DOI: 10.1039/d0ta07416k.
- [66] Hong Nhan Nong, Hoang Phi Tran, Camillo Spöri, Malte Klingenhof, Lorenz Frevel, Travis E. Jones, Thorsten Cottre, Bernhard Kaiser, Wolfram Jaegermann, Robert Schlögl, Detre Teschner, and Peter Strasser. “The Role of Surface Hydroxylation, Lattice Vacancies and Bond Covalency in the Electrochemical Oxidation of Water (OER) on Ni-Depleted Iridium Oxide Catalysts.” In: *Zeitschrift für Physikalische Chemie* 234, 5, 2020, pp. 787–812. ISSN: 09429352. DOI: 10.1515/zpch-2019-1460.
- [67] Reza B. Moghaddam, Chao Wang, Jason B. Sorge, Michael J. Brett, and Steven H. Bergens. “Easily prepared, high activity Ir-Ni oxide catalysts for water oxidation.” In: *Electrochemistry Communications* 60, 2015, pp. 109–112. ISSN: 13882481. DOI: 10.1016/j.elecom.2015.08.015.
- [68] Jinhui Zhu, Min Wei, Qinghao Meng, Zhenyu Chen, Yepeng Fan, Syed Waqar Hasan, Xiaoran Zhang, Dandan Lyu, Zhi Qun Tian, and Pei Kang Shen. “Ultrathin-shell IrCo hollow nanospheres as highly efficient electrocatalysts towards the oxygen evolution reaction in acidic media.” In: *Nanoscale* 12, 47, 2020, pp. 24070–24078. ISSN: 20403372. DOI: 10.1039/d0nr06601j.
- [69] Dickson D. Babu, Yiyin Huang, Ganesan Anandhababu, Xu Wang, Rui Si, Maoxiang Wu, Qiaohong Li, Yaobing Wang, and Jiannian Yao. “Atomic iridium@cobalt nanosheets for dinuclear tandem water oxidation.” In: *Journal of Materials Chemistry A* 7, 14, 2019, pp. 8376–8383. ISSN: 20507496. DOI: 10.1039/c9ta01088b.

- [70] Xuechu Sun, Fei Liu, Xiu Chen, Cuicui Li, Jun Yu, and Mu Pan. “Iridium-doped ZIFs-derived porous carbon-coated IrCo alloy as competent bifunctional catalyst for overall water splitting in acid medium.” In: 307, 2019, pp. 206–213. ISSN: 00134686. DOI: 10.1016/j.electacta.2019.03.179.
- [71] Hongyu Guo, Zhiwei Fang, Hao Li, Desiree Fernandez, Graeme Henkelman, Simon M. Humphrey, and Guihua Yu. “Rational Design of Rhodium-Iridium Alloy Nanoparticles as Highly Active Catalysts for Acidic Oxygen Evolution.” In: *ACS Nano* 13, 11, 2019, pp. 13225–13234. ISSN: 1936086X. DOI: 10.1021/acsnano.9b06244.
- [72] Fan Lv, Jianrui Feng, Kai Wang, Zhipeng Dou, Weiyu Zhang, Jinhui Zhou, Chao Yang, Mingchuan Luo, Yong Yang, Yingjie Li, Peng Gao, and Shaojun Guo. “Iridium-Tungsten Alloy Nanodendrites as pH-Universal Water-Splitting Electrocatalysts.” In: *ACS Central Science* 4, 9, 2018, pp. 1244–1252. ISSN: 23747951. DOI: 10.1021/acscentsci.8b00426.
- [73] Chao Wang, Reza B. Moghaddam, and Steven H. Bergens. “Active, Simple Iridium-Copper Hydrous Oxide Electrocatalysts for Water Oxidation.” In: *Journal of Physical Chemistry C* 121, 10, 2017, pp. 5480–5486. ISSN: 19327455. DOI: 10.1021/acs.jpcc.6b12164.
- [74] In Gyeom Kim, Ahyoun Lim, Jong Hyun Jang, Kwan Young Lee, In Wook Nah, and Sehkyu Park. “Leveraging metal alloy-hybrid support interaction to enhance oxygen evolution kinetics and stability in proton exchange membrane water electrolyzers.” In: *Journal of Power Sources* 501, 2021. ISSN: 03787753. DOI: 10.1016/j.jpowsour.2021.230002.
- [75] Alison Cowley. *PGM Market Report*. Tech. rep. Johnson Matthey, 2023.
- [76] National Minerals Information Center. *MINERAL COMMODITY SUMMARIES*. Tech. rep. U.S. Department of the Interior, U.S. Geological Survey, 2023.
- [77] Yecan Pi, Qi Shao, Pengtang Wang, Jun Guo, and Xiaoqing Huang. “General Formation of Monodisperse IrM (M = Ni, Co, Fe) Bimetallic Nanoclusters as Bifunctional Electrocatalysts for Acidic Overall Water Splitting.” In: *Advanced Functional Materials* 27, 27, 2017. ISSN: 16163028. DOI: 10.1002/adfm.201700886.
- [78] Fan Lv, Weiyu Zhang, Wenxiu Yang, Jianrui Feng, Kai Wang, Jinhui Zhou, Peng Zhou, and Shaojun Guo. “Ir-Based Alloy Nanoflowers with Optimized Hydrogen Binding Energy as Bifunctional Electrocatalysts for Overall Water Splitting.” In: *Small Methods* 4, 6, 2020. ISSN: 23669608. DOI: 10.1002/smt.201900129.

- [79] Kyeong Rim Yeo, Kug Seung Lee, Hoyoung Kim, Jinwoo Lee, and Soo Kil Kim. “A highly active and stable 3D dandelion spore-structured self-supporting Ir-based electrocatalyst for proton exchange membrane water electrolysis fabricated using structural reconstruction.” In: *Energy and Environmental Science*, 2022. ISSN: 17545706. DOI: 10.1039/d2ee01042a.
- [80] Chun Hu, Kaihang Yue, Jiajia Han, Xiaozhi Liu, Lijia Liu, Qiunan Liu, Qingyu Kong, Chih-Wen Pao, Zhiwei Hu, Kazu Suenaga, Dong Su, Qiaobao Zhang, Xianying Wang, Yuanzhi Tan, and Xiaoqing Huang. “Misoriented high-entropy iridium ruthenium oxide for acidic water splitting.” In: *Science Advances*, 9, 2023. DOI: 10.1126/sciadv.adf9144.
- [81] Hong Nhan Nong, Lin Gan, Elena Willinger, Detre Teschner, and Peter Strasser. “IrOx core-shell nanocatalysts for cost- and energy-efficient electrochemical water splitting.” In: *Chemical Science* 5, 8, 2014, pp. 2955–2963. ISSN: 20416539. DOI: 10.1039/c4sc01065e.
- [82] Jianrui Feng, Fan Lv, Weiyu Zhang, Peihao Li, Kai Wang, Chao Yang, Bin Wang, Yong Yang, Jinhui Zhou, Fei Lin, Gui Chang Wang, and Shaojun Guo. “Iridium-Based Multimetallic Porous Hollow Nanocrystals for Efficient Overall-Water-Splitting Catalysis.” In: *Advanced Materials* 29, 47, 2017. ISSN: 15214095. DOI: 10.1002/adma.201703798.
- [83] Yecan Pi, Qi Shao, Xing Zhu, and Xiaoqing Huang. “Dynamic Structure Evolution of Composition Segregated Iridium-Nickel Rhombic Dodecahedra toward Efficient Oxygen Evolution Electrocatalysis.” In: *ACS Nano* 12, 7, 2018, pp. 7371–7379. ISSN: 1936086X. DOI: 10.1021/acsnano.8b04023.
- [84] Di Liu, Siqi Lu, Yanrong Xue, Zhi Guan, Jinjie Fang, Wei Zhu, and Zhongbin Zhuang. “One-pot synthesis of IrNi@Ir core-shell nanoparticles as highly active hydrogen oxidation reaction electrocatalyst in alkaline electrolyte.” In: *Nano Energy* 59, 2019, pp. 26–32. ISSN: 22112855. DOI: 10.1016/j.nanoen.2019.01.070.
- [85] Woong Hee Lee, Jaekyung Yi, Hong Nhan Nong, Peter Strasser, Keun Hwa Chae, Byoung Koun Min, Yun Jeong Hwang, and Hyung Suk Oh. “Electroactivation-induced IrNi nanoparticles under different pH conditions for neutral water oxidation.” In: *Nanoscale* 12, 27, 2020, pp. 14903–14910. ISSN: 20403372. DOI: 10.1039/d0nr02951c.
- [86] Tobias Reier, Zarina Pawolek, Serhiy Cherevko, Michael Bruns, Travis Jones, Detre Teschner, Sören Selve, Arno Bergmann, Hong Nhan Nong, Robert Schlögl, Karl J.J. Mayrhofer, and Peter Strasser. “Molecular insight in structure and activity of highly efficient, low-Ir Ir-Ni oxide catalysts for electrochemical water splitting (OER).” In: *Journal of the American Chemical Society* 137, 40, 2015, pp. 13031–13040. ISSN: 15205126. DOI: 10.1021/jacs.5b07788.

- [87] Xiu Chen, Mingyue Xu, Shang Li, Cuicui Li, Xuechu Sun, Shichun Mu, and Jun Yu. “Ultrafine IrNi Bimetals Encapsulated in Zeolitic Imidazolate Frameworks-Derived Porous N-Doped Carbon for Boosting Oxygen Evolution in Both Alkaline and Acidic Electrolytes.” In: *Advanced Materials Interfaces* 7, 24, 2020. ISSN: 21967350. DOI: 10.1002/admi.202001145.
- [88] Jianhua Liao, Wei Ding, Sicheng Tao, Yao Nie, Wei Li, Guangping Wu, Siguo Chen, Li Li, and Zidong Wei. “Carbon supported IrM (M = Fe, Ni, Co) alloy nanoparticles for the catalysis of hydrogen oxidation in acidic and alkaline medium.” In: *Cuihua Xuebao/Chinese Journal of Catalysis* 37, 7, 2016, pp. 1142–1148. ISSN: 02539837. DOI: 10.1016/S1872-2067(15)61064-6.
- [89] Jonathan Ruiz Esquius, Gerardo Algara-Siller, Ioannis Spanos, Simon J. Freakley, Robert Schlögl, and Graham J. Hutchings. “Preparation of solid solution and layered IroNi(OH)₂ oxygen evolution catalysts: Toward optimizing iridium efficiency for OER.” In: *ACS Catalysis* 10, 24, 2020, pp. 14640–14648. ISSN: 21555435. DOI: 10.1021/acscatal.0c03866.
- [90] Alaina L. Strickler, Raul A. Flores, Laurie A. King, Jens K. Nørskov, Michal Bajdich, and Thomas F. Jaramillo. “Systematic Investigation of Iridium-Based Bimetallic Thin Film Catalysts for the Oxygen Evolution Reaction in Acidic Media.” In: *ACS Applied Materials and Interfaces* 11, 37, 2019, pp. 34059–34066. ISSN: 19448252. DOI: 10.1021/acscami.9b13697.
- [91] Berkermann and Frederic. “Preparation and Application of Aqueous Iridium Oxide Colloids.” PhD thesis. Ruhr University Bochum, 2010.
- [92] Brian Derby. “Inkjet printing of functional and structural materials: Fluid property requirements, feature stability, and resolution.” In: *Annual Review of Materials Research* 40, 2010, pp. 395–414. ISSN: 15317331. DOI: 10.1146/annurev-matsci-070909-104502.
- [93] Brian Adams. *Wolfram Local Acceleration Of Gravity Widget*. Available at <https://www.wolframalpha.com/widgets/view.jsp?id=e856809e0d522d3153e2e7e8ec263bf2> (22/06/2023).
- [94] *Litesizer Series Instruments: Reference Guide*. Tech. rep. Anton Paar, 2018.
- [95] *White Paper: Understanding the Concept of Dynamic Light Scattering*. Tech. rep. Anton Paar, 2018.
- [96] *White Paper: Data Acquisition, Processing and Interpretation in the Litesizer Series*. Tech. rep. Anton Paar, 2018.
- [97] Gordon Macbeth and A Ralph Thompson. “Densities and Refractive Indexes for Propylene Glycol-Water Solutions.” In: *Analytical Chemistry* 23, 4, 1951, pp. 618–619.

- [98] Scott Storbakken. *Fabrication and Testing of Inkjet Printed Electrodes for Anion Exchange Membrane Water Electrolysis*. MSc. University of Alberta. 2022.
- [99] Jonas Backholm and Gunnar A. Niklasson. “Optical properties of electrochromic iridium oxide and iridium-tantalum oxide thin films in different colouration states.” In: *Solar Energy Materials and Solar Cells* 92, 11, 2008, pp. 1388–1392. ISSN: 09270248. DOI: 10.1016/j.solmat.2008.05.015.
- [100] Wentao Wang, Shunquan Chen, Jianjun Li, and Wei Wang. “Fabrication of catalyst coated membrane with screen printing method in a proton exchange membrane fuel cell.” In: *International Journal of Hydrogen Energy* 40, 13, 2015, pp. 4649–4658. ISSN: 03603199. DOI: 10.1016/j.ijhydene.2015.02.027.
- [101] S. Kundu, M. W. Fowler, L. C. Simon, and S. Grot. “Morphological features (defects) in fuel cell membrane electrode assemblies.” In: *Journal of Power Sources* 157, 2, 2006, pp. 650–656. ISSN: 03787753. DOI: 10.1016/j.jpowsour.2005.12.027.
- [102] Sang Moon Kim, Chi-Yeong Ahn, Yong-Hun Cho, Sungjun Kim, Wonchan Hwang, Segeun Jang, Sungsoo Shin, Gunhee Lee, Yung-Eun Sung, and Mansoo Choi. “High-performance fuel cell with stretched catalyst-coated membrane: One-step formation of cracked electrode.” In: *Scientific Reports* 6, 2016. ISSN: 20452322. DOI: 10.1038/srep26503.
- [103] Chi Yeong Ahn, Segeun Jang, Yong Hun Cho, Jiwoo Choi, Sungjun Kim, Sang Moon Kim, Yung Eun Sung, and Mansoo Choi. “Guided cracking of electrodes by stretching prism-patterned membrane electrode assemblies for high-performance fuel cells.” In: *Scientific Reports* 8, 1, 2018. ISSN: 20452322. DOI: 10.1038/s41598-018-19861-6.
- [104] Naoki Hasegawa, Atsushi Kamiya, Takuro Matsunaga, Naoki Kitano, and Masashi Harada. “Analysis of crack formation during fuel cell catalyst ink drying process. Reduction of catalyst layer cracking by addition of high boiling point solvent.” In: *Colloids and Surfaces A: Physicochemical and Engineering Aspects* 628, 2021. ISSN: 18734359. DOI: 10.1016/j.colsurfa.2021.127153.
- [105] Naomi Kumano, Kenji Kudo, Akihiko Suda, Yusuke Akimoto, Masahiko Ishii, and Hiroshi Nakamura. “Controlling cracking formation in fuel cell catalyst layers.” In: *Journal of Power Sources* 419, 2019, pp. 219–228. ISSN: 03787753. DOI: 10.1016/j.jpowsour.2019.02.058.
- [106] Manas Kumar Mandal. “Understanding the physical phenomena limiting the inkjet printed PEM water electrolyzer performance.” PhD thesis. University of Alberta, 2022.

- [107] Simon Hettler, Manuel Dries, Peter Hermann, Martin Obermair, Dagmar Gerthsen, and Marek Malac. “Carbon contamination in scanning transmission electron microscopy and its impact on phase-plate applications.” In: *Micron* 96, 2017, pp. 38–47. ISSN: 09684328. DOI: 10.1016/j.micron.2017.02.002.
- [108] D. R.G. Mitchell. “Contamination mitigation strategies for scanning transmission electron microscopy.” In: *Micron* 73, 2015, pp. 36–46. ISSN: 09684328. DOI: 10.1016/j.micron.2015.03.013.
- [109] Himanshi Dhawan, Marc Secanell, and Natalia Semagina. “State-of-the-Art Iridium-Based Catalysts for Acidic Water Electrolysis: A Minireview of Wet-Chemistry Synthesis Methods.” In: *Johnson Matthey Technology Review* 65, 2, 2021, pp. 247–262. ISSN: 20565135. DOI: 10.1595/205651321x16013966874707.
- [110] Verena Pfeifer, Travis E. Jones, Juan J. Velasco Vélez, Cyriac Massué, Rosa Arrigo, Detre Teschner, Frank Girgsdies, Michael Scherzer, Mark T. Greiner, Jasmin Allan, Maike Hashagen, Gisela Weinberg, Simone Piccinin, Michael Hävecker, Axel Knop-Gericke, and Robert Schlögl. “The electronic structure of iridium and its oxides.” In: *Surface and Interface Analysis* 48, 5, 2016, pp. 261–273. ISSN: 10969918. DOI: 10.1002/sia.5895.
- [111] Ibrahim S. Khattab, Farzana Bandarkar, Maryam Khoubnasabjafari, and Abolghasem Jouyban. “Density, viscosity, surface tension, and molar volume of propylene glycol + water mixtures from 293 to 323 K and correlations by the Jouyban–Acree model.” In: *Arabian Journal of Chemistry* 10, 2017, S71–S75. ISSN: 18785352. DOI: 10.1016/j.arabjc.2012.07.012.
- [112] Deena Titus, E. James Jebaseelan Samuel, and Selvaraj Mohana Roopan. “Nanoparticle characterization techniques.” In: 2018, pp. 303–319. ISBN: 9780081025796. DOI: 10.1016/B978-0-08-102579-6.00012-5.
- [113] Julie Christine Fornaciari. “Optimizing Transport Phenomena in Electrolytic Cells.” PhD thesis. University of California, Berkeley, 2022.
- [114] Maniya Aghasibeig, Christian Moreau, Ali Dolatabadi, and Rolf Wuthrich. “Engineered Three-Dimensional Electrodes by HVOF Process for Hydrogen Production.” In: *Journal of Thermal Spray Technology* 25, 8, 2016, pp. 1561–1569. ISSN: 10599630. DOI: 10.1007/s11666-016-0458-9.
- [115] Philipp Jan Rheinländer and Julien Durst. “Transformation of the OER-Active IrO_x Species under Transient Operation Conditions in PEM Water Electrolysis.” In: *Journal of The Electrochemical Society* 168, 2, 2021, p. 024511. ISSN: 0013-4651. DOI: 10.1149/1945-7111/abe0d4.

- [116] Daniel F. Abbott, Dmitry Lebedev, Kay Waltar, Mauro Povia, Maarten Nachtegaal, Emiliana Fabbri, Christophe Copéret, and Thomas J. Schmidt. “Iridium oxide for the oxygen evolution reaction: Correlation between particle size, morphology, and the surface hydroxo layer from operando XAS.” In: *Chemistry of Materials* 28, 18, 2016, pp. 6591–6604. ISSN: 15205002. DOI: 10.1021/acs.chemmater.6b02625.
- [117] Krisztina J. Szekeres, Soma Vesztergom, Maria Ujvári, and Gyözö G. Láng. “Methods for the Determination of Valid Impedance Spectra in Non-stationary Electrochemical Systems: Concepts and Techniques of Practical Importance.” In: *ChemElectroChem* 8, 7, 2021, pp. 1233–1250. ISSN: 21960216. DOI: 10.1002/ce1c.202100093.
- [118] Alexandros Ch Lazanas and Mamas I. Prodromidis. “Electrochemical Impedance SpectroscopyA Tutorial.” In: *ACS Measurement Science Au* 3, 2023, pp. 162–193. ISSN: 2694250X. DOI: 10.1021/acsmeasuresciau.2c00070.
- [119] Yujiao Sun, Xiuping Zhang, Cong Wang, Xiaofang Bai, Li Fan, Jiantao Fan, Shaoyi Xu, and Hui Li. “Effect of poly(3,4-ethylenedioxythiophene): poly(styrenesulfonate) on low-iridium catalyst layer for proton exchange membrane water electrolysis.” In: *Journal of Power Sources* 586, 2023. ISSN: 03787753. DOI: 10.1016/j.jpowsour.2023.233678.

Appendix A

Additional Methodology

A.1 Triply Distilled Water

The water used to disperse the chlorinated salts for both $\text{IrCl}_3 \cdot x\text{H}_2\text{O}$ and $\text{NiCl}_2 \cdot 6\text{H}_2\text{O}$ was triply distilled. This means it went from first distillation which was using deionized water from a tap and then went through two further distillation steps where the water was evaporated and re-condensed. The apparatus is shown in Figure A.1.

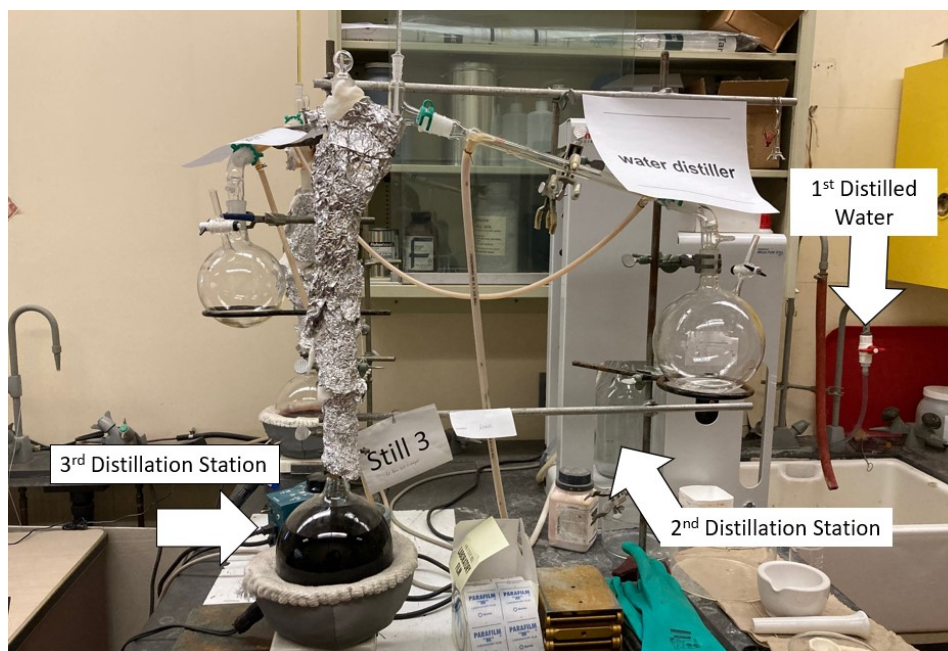


Figure A.1: Triple distillation of water apparatus.

A.2 Viscometer Calibration

2139 High Tech Road
 State College, PA 16803
 814-353-8000 • 800-676-6232 • Fax 814-353-8007
cannon@cannoninstrument.com
www.cannoninstrument.com

Certificate of Calibration

ZEITFUCHS CROSS-ARM VISCOMETER			
Size	2	Serial Number	B562
Constant	Expanded Uncertainty* (k=2)	Kinematic Viscosity Range	
mm ² /s ² , (cSt/s)	%	mm ² /s, (cSt)	
0.009463	0.16	2 - 10	

* In alignment with the Calibration and Measurement Capabilities of National Metrology Institutes, the expressed uncertainty is relative to the viscosity of water, and therefore the uncertainty of the viscosity of water (ISO/TR 3666 (1998), 0.17%) is not taken into account.

CALIBRATION DATA AT 40°C - The viscometer constant is the same at all temperatures.

Viscosity Standard	Kinematic Viscosity mm ² /s, (cSt)	Efflux Time Seconds	Constant mm ² /s ² , (cSt/s)
12	2.418	255.54	0.009460
13	3.829	404.56	0.009465

Average = 0.009463

Kinematic viscosities of the standards used in calibrating were established in Master Viscometers as described in Ind. Eng. Chem. Anal. Ed. 16,708(1944), ASTM D 2162, and the Journal of Research of the National Bureau of Standards, Vol. 52, No. 3, March 1954, Research Paper 2479.

Kinematic viscosities are traceable to the viscosity of, water ISO 3666, at 20°C (ITS-90). Temperature measurements are traceable to NIST fixed-point calibration of SPRTs.

The gravitational constant, g, is 980.1 cm/sec² at the Cannon Instrument Company. The gravitational constant varies up to 0.1% in the United States. To make this small correction in the viscometer constant, multiply the above viscometer constant by the factor [g (at your laboratory) / 980.1].

Calibrated by DLH on 3/15/2021

Issue Date 3/15/2021

under supervision of

D. T. Trowbridge Ph.D

J. T. Mastropiero

M. T. Zubler

Laboratory Technical Director

Deputy Laboratory Technical Director

Director of Quality Assurance



Figure A.2: Zeitfuchs Cross-arm Viscometer Certificate of Calibration.

A.3 Setting Images

A.3.1 Inkjet printing ink jetting settings

Below are the cartridge and waveform settings used to inkjet print the CCMs in this work. The waveform used was a multi-pulse configuration where small pulses were used to create an initial droplet which would then be expelled during the more powerful push at the end. Using multi-pulse allows the droplet size to be increased so more ink can be deposited than usual with a small nozzle diameter.

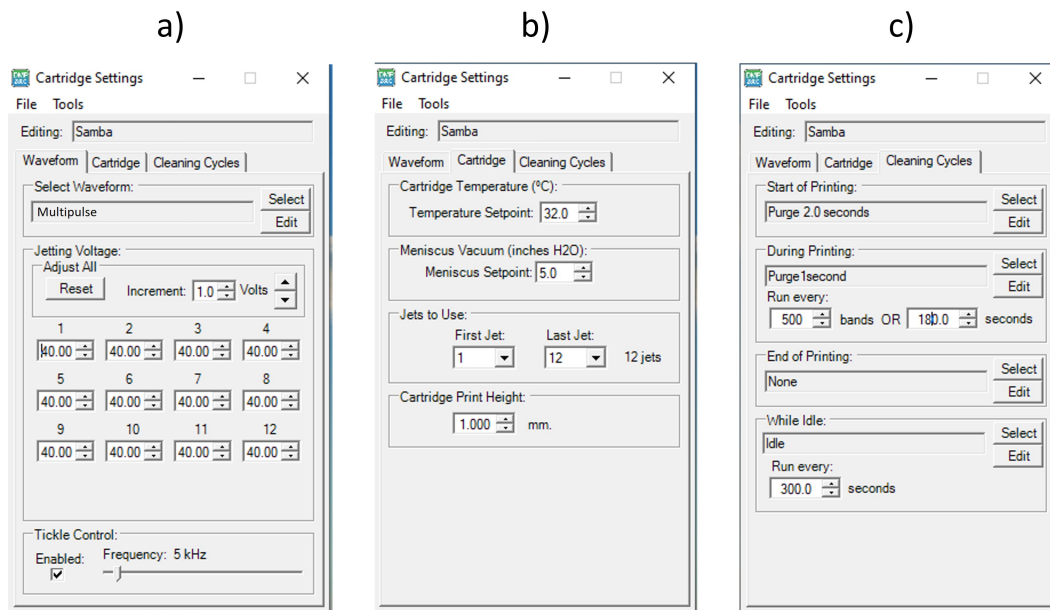


Figure A.3: Cartridge settings for inkjet printing. a) waveform choice and piezoelectric voltage , b) cartridge temperature and nozzle settings, c) cleaning settings.

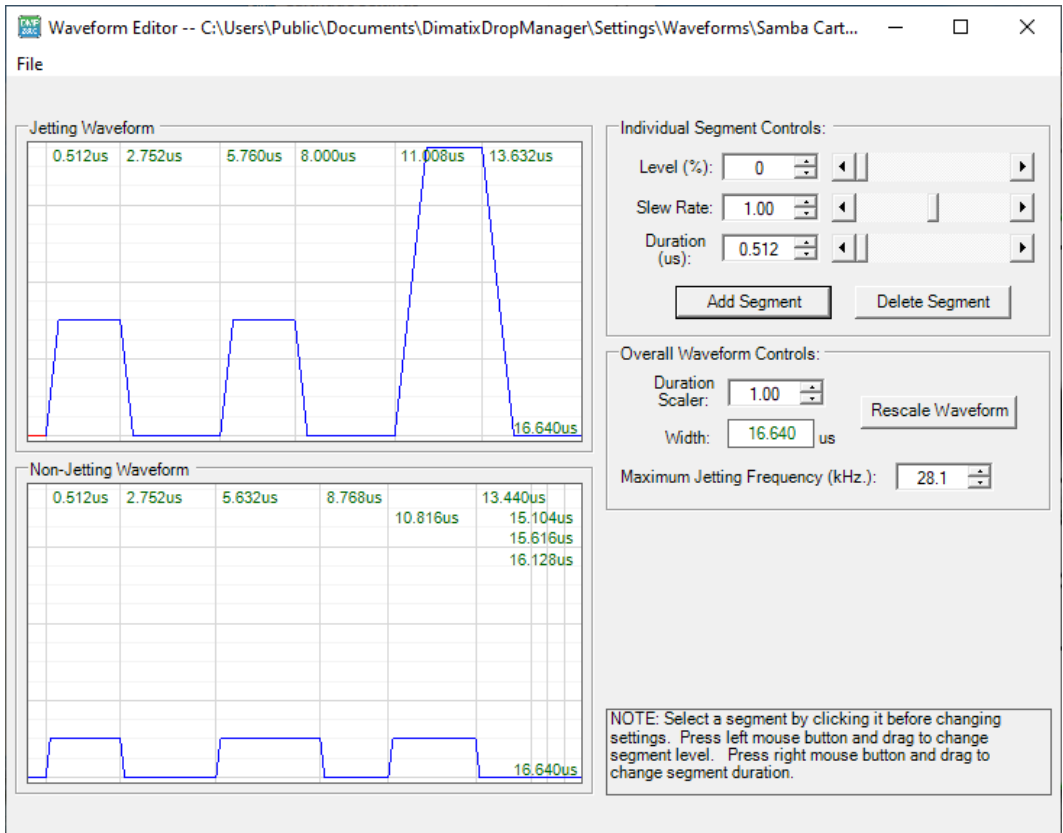


Figure A.4: Multi-pulse waveform.

A.3.2 CV

The screenshot shows a software interface for setting Cyclic Voltammetry (CV) parameters. The interface is divided into several sections:

- Devices:** Shows a list of devices, including "SP-300 - virtual".
- Experiment:** Contains buttons for "Advanced Settings", "Cell Characteristics", "External Devices", and "Parameters Settings" (which is highlighted in yellow).
- Parameters Settings:** This section contains the following parameters:
 - Turn to OCV between techniques
 - Set E_{we} to E_j = 0.250 V vs. Ref
 - Scan E_{we} with dE/dt = 40.000 mV/s
 - to vertex potential E_1 = 0.005 V vs. Ref
 - Reverse scan to vertex E_2 = 1.500 V vs. Ref
 - Repeat n_c = 10 time(s)
 - Measure <I> over the last 30 % of the step duration
 - Record <I> averaged over N = 10 voltage steps
 - E Range = 0 V; 5 V (Resolution = 100 μ V)
 - I Range = 1 A
 - Bandwidth = 8
 - End scan to E_f = 0.250 V vs. Ref
 - Force E_1 / E_2 (dE/dt \sim 100 μ V / 2 ms, dEN \sim 1.0 mV, 2990 points per cycle)
- Bottom Panel:** Contains control buttons for play, pause, and stop.

Figure A.5: The setting parameters filled out to obtain a CV.

A.3.3 LSV

Devices

Turn to OCV between techniques

Rest for t_R = 0 h 0 mn 0.000 0 s

Limit $|dE_{we} / dt| < dE_R / dt$ = 0.0 mV/h

Record every dE_R = 10 mV
or dt_R = 1.000 0 s

Scan E_{we} with dE/dt = 2.000 mV/s

from E_i = 1.300 V vs. Ref

to E_L = 1.750 V vs. Ref

Record <I>

over the last 50 % of the step duration

average N = 1 voltage steps

E Range = 0 V; 2.5 V
Resolution = 50 μ V

I Range = 10 A

Bandwidth = 8

($dE/dt \sim 50 \mu\text{V} / 25 \text{ms}$)
($dEN \sim 50 \mu\text{V}$)

Experiment

Advanced Settings

Cell Characteristics

External Devices

Parameters Settings

1 - LSV

Figure A.6: The setting parameters filled out to obtain a LSV.


A.3.4 EIS

Excitation signal mode		Single sine	▼
Set I to $I_s =$		0.100	A ▼ vs. <None> ▼
for $t_{I_s} =$		0	h 2 mn 0.000 s
<input type="checkbox"/>	Record every $dE =$	0.000	mV
	and $dt =$	0.000	s
Scan from $f_i =$		100.000	kHz ▼
to $f_f =$		20.000	mHz ▼
with $N_d =$		50	points per decade ▼
in		Logarithmic	spacing ▼
amplitude $I_a =$		30.000	mA ▼
wait for $p_w =$		0.10	period before each frequency
average $N_a =$		1	measure(s) per frequency
drift correction		<input type="checkbox"/>	
Repeat $n_c =$		0	time(s)
E Range =		0V; 5V	▼ ...
		<i>Resolution = 100 μV'</i>	
I Range =		1 A	▼
Bandwidth =		6	▼
		(~ 22mn08s / scan)	
Go back to seq. $N_s' =$		0	(9999 ends technique)
for $n_r =$		0	time(s) (0 for next sequence)
		<input type="checkbox"/>	increment cycle number

Figure A.7: The setting parameters filled out to obtain the first EIS curve at 0.1 A.

Excitation signal mode **Single sine** ▾

Set **I** to **I_s** = **A** ▾ vs. **<None>** ▾
 for **t_{I_s}** = h mn s
 Record every **dE** = mV
 and **dt** = s

Scan from **f_i** = kHz ▾ 
 to **f_f** = mHz ▾
 with **N_d** = points **per decade** ▾
 in **Logarithmic** ▾ spacing
 amplitude **I_a** = mA ▾
 wait for **p_w** = period before each frequency
 average **N_a** = measure(s) per frequency
 drift correction
Repeat n_c = time(s)


E Range = ▾ ...
Resolution = 100 μV
I Range = ▾
Bandwidth = ▾
 (~ 22mn37s / scan)

Go back to seq. N_{s'} = (*9999 ends technique*)
 for **n_f** = time(s) (*0 for next sequence*)
 increment cycle number

Figure A.8: The setting parameters filled out to obtain the second EIS curve at 1 A.

Excitation signal mode **Single sine** ▾

Set **I** to **I_s** = A ▾ vs. ▾
 for **t_{I_s}** = h mn s
 Record every **dE** = mV
 and **dt** = s

Scan from **f_i** = kHz ▾ 
 to **f_f** = mHz ▾
 with **N_d** = points **per decade** ▾
 in **Logarithmic** ▾ spacing
 amplitude **I_a** = mA ▾
 wait for **p_w** = period before each frequency
 average **N_a** = measure(s) per frequency
 drift correction
 Repeat **n_c** = time(s)

E Range = ▾ ...
Resolution = 100 μV
 I Range = ▾
 Bandwidth = ▾
 (~ 22mn37s / scan)

Go back to seq. **N_{s'}** = (*9999 ends technique*)
 for **n_f** = time(s) (*0 for next sequence*)
 increment cycle number

Figure A.9: The setting parameters filled out to obtain the third EIS curve at 10 A.

A.4 Pinch Value

The pinch of the cell is the difference between the values of X and Y in Figure A.10 and determines how much compression is applied from the PTL and GDL/MPL to the catalyst layers. The pinch is found using the equation

$$\text{Pinch} = (t_{GDL/MPL} + t_c + t_a + t_{PTL} + t_{PM}) - (2 \times t_l + t_{CG} + t_{AG} + t_{PM}) \quad (\text{A.1})$$

where $t_{GDL/MPL}$ is the thickness of the GDL/MPL, t_c is the thickness of the cathode catalyst layer, t_a is the thickness of the anode catalyst layer, t_{PTL} is the thickness of the PTL, t_{PM} is the thickness of the polymer membrane, t_{CG} is the thickness of the cathode gasket, t_{AG} is the thickness of the anode gasket, and t_l is the thickness of the lamination sheets. Using the values in Table 2.3 the pinch is 67.2 μm which is close to the 72 μm that was desired.

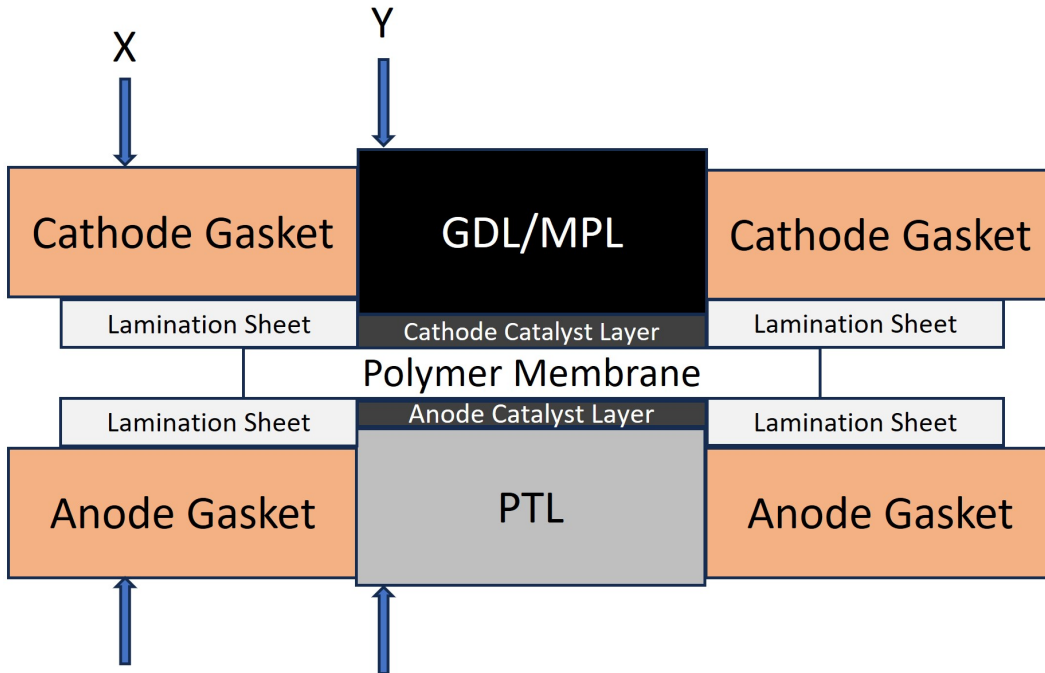


Figure A.10: Schematic of MEA components pressing on the polymer membrane and catalyst layers at different distances to create the pinch.

Appendix B

IrNi EDX Spectra

Figure B.1 shows the EDX spectra for the Ir₈NiO_x catalyst layer before cell assembly.

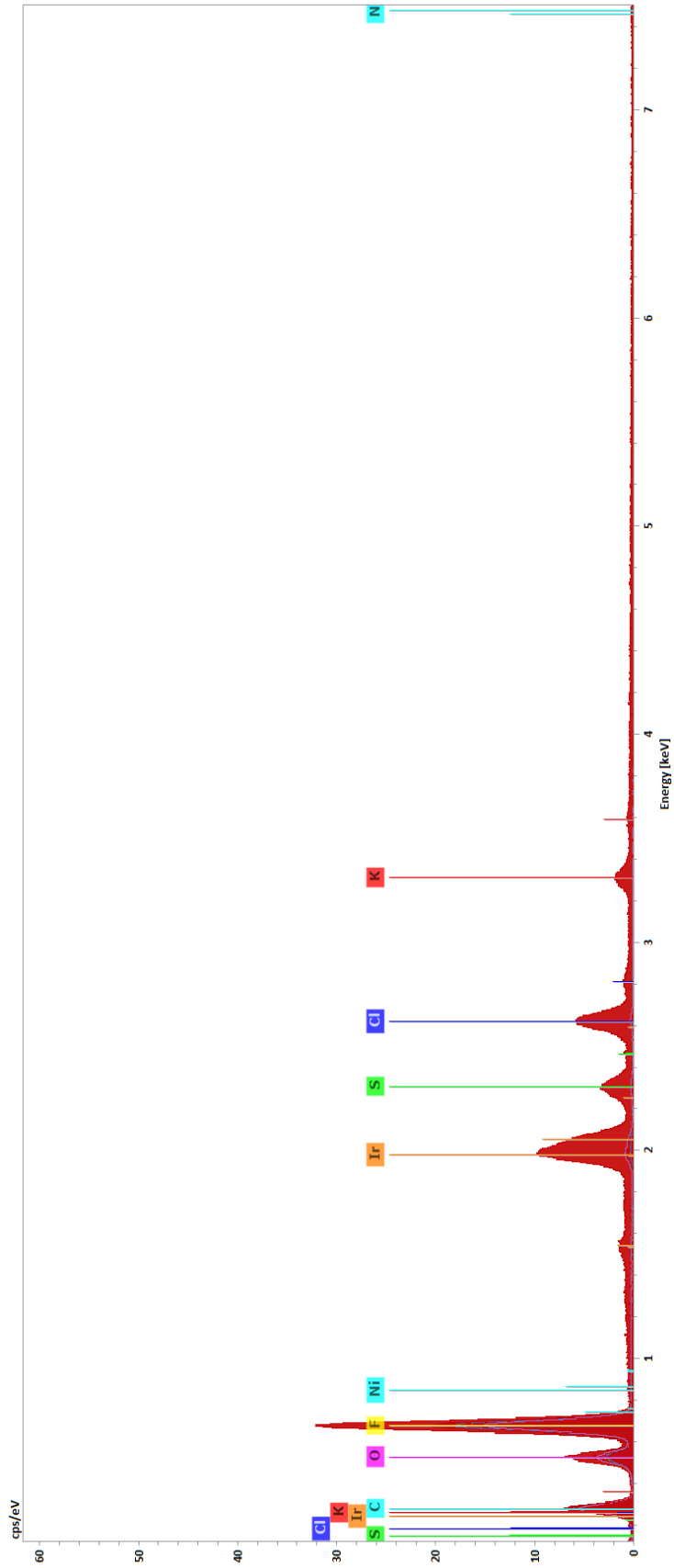


Figure B.1: EDX spectra for the surface of E2, Ir₈NiO_x 0.99 mg/cm².

Appendix C

Additional IrO_x TTK Loading Results

C.0.1 SEM Images

Figures C.1-C.3 show the SEM images at 1000x, 500x, 200x and 100x magnification for ML20-ML22.

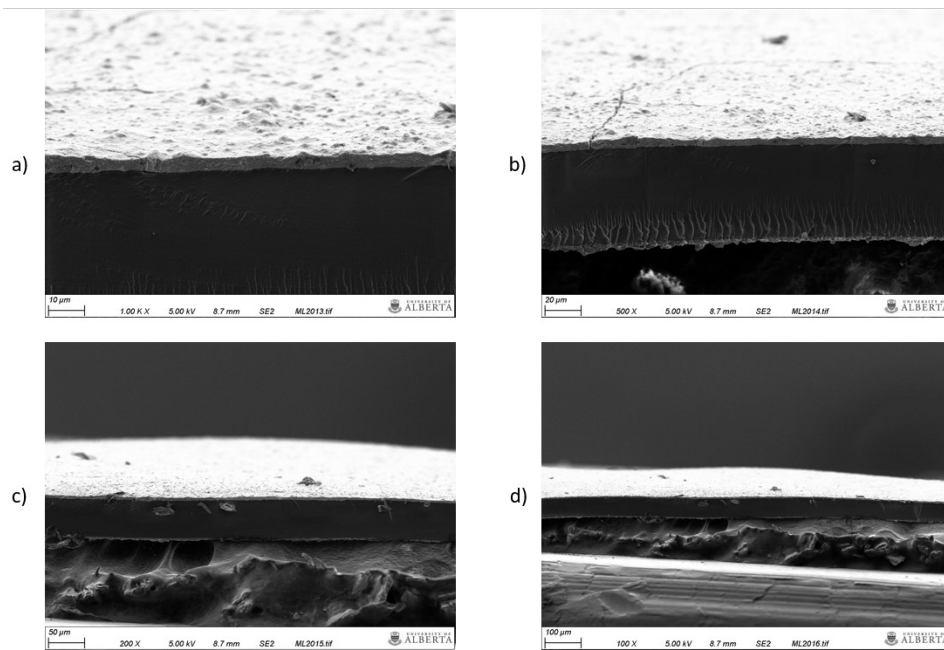


Figure C.1: SEM images of ML20, 0.808 mg/cm² IrO_x TTK at a) 1000x, b) 500x, c) 200x, d) 100x.

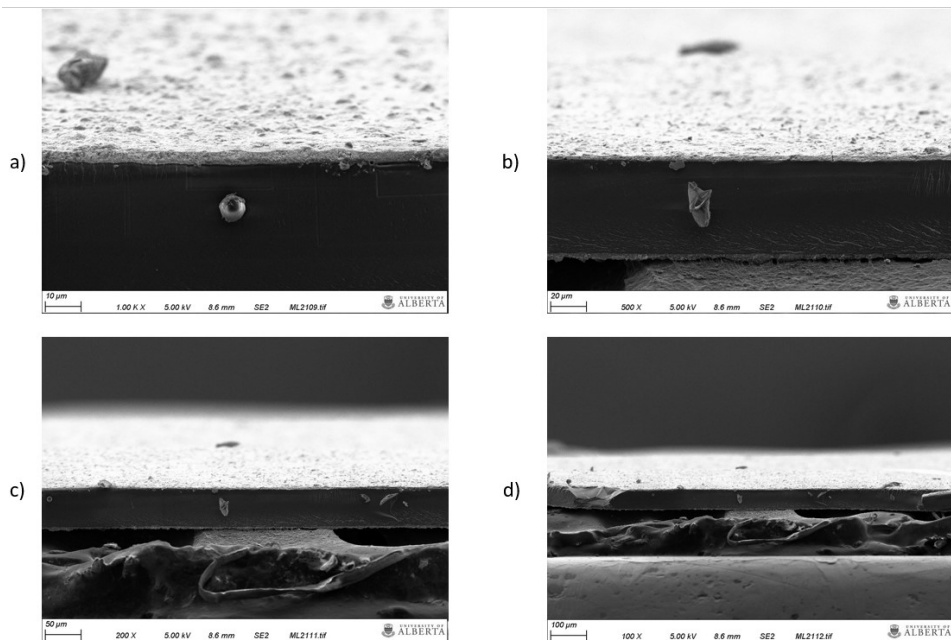


Figure C.2: SEM images of ML21, $0.567 \text{ mg/cm}^2 \text{ IrO}_x$ TKK at a) 1000x, b) 500x, c) 200x, d) 100x.

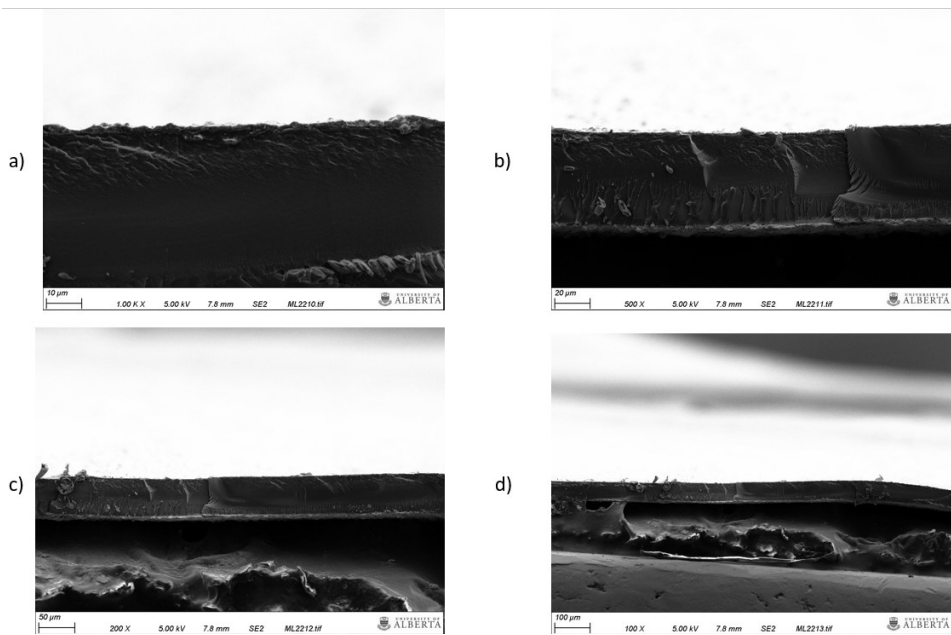


Figure C.3: SEM images of ML22, $0.241 \text{ mg/cm}^2 \text{ IrO}_x$ TKK at a) 1000x, b) 500x, c) 200x, d) 100x.

C.0.2 Different Loading Pol. Curves

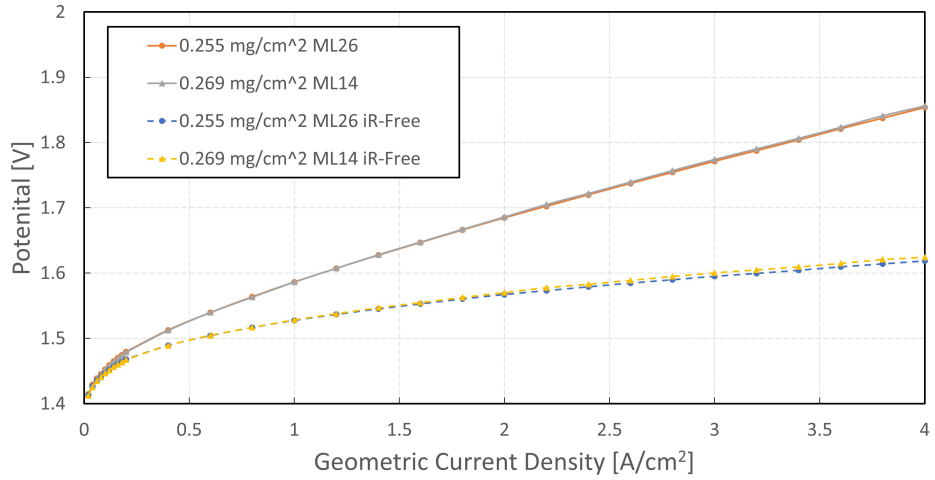


Figure C.4: Pol. curves and iR-free pol. curves for 0.25 mg/cm² cells.

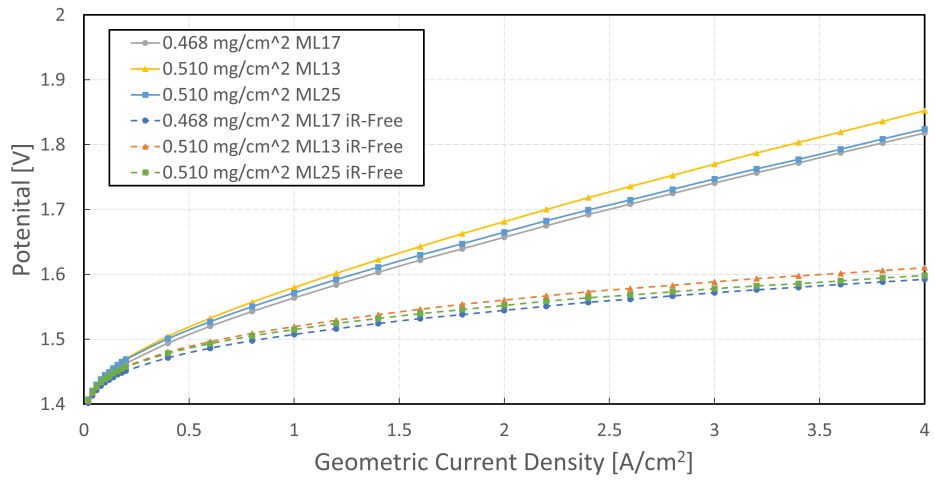


Figure C.5: Pol. curves and iR-free pol. curves for 0.5 mg/cm² cells.

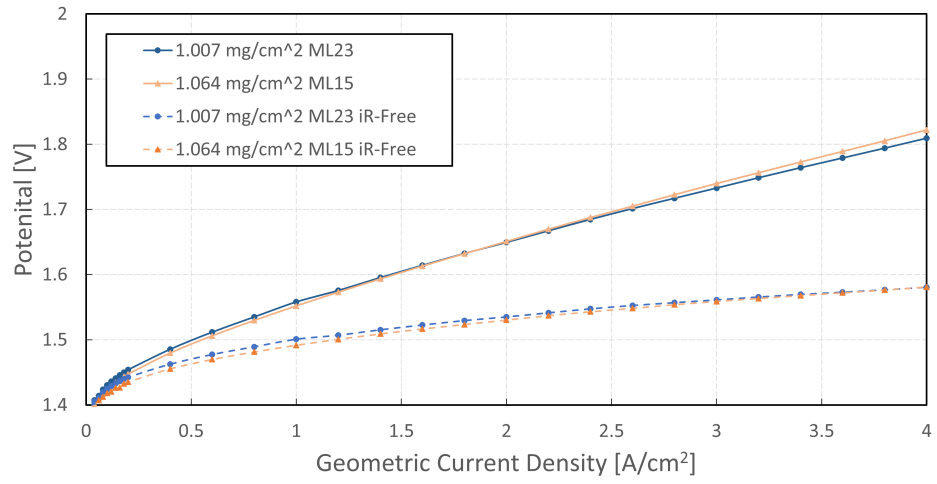


Figure C.6: Pol. curves and iR-free pol. curves for 1 mg/cm² cells.